

Performance Analysis and Characterisation of a new
Magneto-Electrical Measurement System for
Electrical Conductivity Imaging

Arre Job Verweerd

**Performance Analysis and Characterisation of an new
Magneto-Eletrical Measurement System for
Electrical Conductivity Imaging**

Dissertation

zur
Erlangung des Doktorgrades (Dr. rer. nat.)
der
Mathematisch-Naturwissenschaftlichen Fakultät
der
Rheinischen Friedrich-Wilhelms-Universität Bonn

vorgelegt von

Arre Job Verweerd

aus Lekkerkerk, die Niederlande

Bonn, 2007

Angefertigt mit der Genehmigung der Mathematisch-Naturwissenschaftlichen Fakultät
der Rheinischen Friedrich-Wilhelms-Universität Bonn.

Diese Dissertation ist auf dem Hochschulschriftenserver der ULB Bonn
http://hss.ulb.uni-bonn.de/diss_online elektronisch publiziert.

1. Referent: Univ.-Prof. Dr. Hoerdt, A.
2. Referent: Univ.-Prof. Dr. Vereecken, H.

Tag der Promotion: 04.05.2007

Erscheinungsjahr: 2007

Di manakah engkau, ketika Aku melerakkan dasar bumi?

Ceritakanlah, kalau engkau mempunyai pengertian!

Siapakah yang telah menetapkan ukurannya?

Bukankah engkau mengetahuinya?

- Atau siapakah yang telah merentangkan tali pengukur padanya?

Atas apakah seni-sendinya dilantak, dan siapakah yang memasang batu
penjurunya?

Ayup 38: 4-6

Abstract

An often used proxy in hydrogeology is the electrical conductivity distribution to study flow and transport of groundwater in soil. In order to map the electrical conductivity distribution of soil columns (length 0.5 m and 0.1 m radius), traditionally ERT (Electrical Resistivity Tomography) is used. In this thesis the ERT measurements will be complimented by magnetometric resistivity (MMR) measurements. Due to a low frequency current injection (25 Hz) a current distribution is generated in the soil column of which the electrical potential is measured at several electrodes. This current has an associated magnetic field, also depending on the internal electrical conductivity distribution, this resulting magnetic field is measured in the MMR method.

The magneto-electrical resistivity imaging technique (MERIT) combines the measurement of both electric and magnetic parameters. In this thesis the development of a small laboratory scale system will be described. The electrical potentials are measured by small stainless steel screws inserted into the plexi-glass mantle of the soil column, the magnetic fields are measured with especially designed sensor modules. The three component magnetic field modules are composed of AMR sensors, and are located on a vertical moving scanning torus. The magnetic field measurement system is designed to operate under 'typical' laboratory noise conditions.

The development of this new measurement system also includes optimization of the sensor positions and current injection geometries. The technique of singular value decomposition is applied to the Jacobian (or sensitivity matrix) of a combined ERT and MMR dataset in order to obtain information on the behaviour of the system in the so-called model space as well as its data space. This information can be used to obtain a quantitative measure of the optimum measurement configuration and the optimum resolution of the MERIT system, depending on the target of the survey.

Finally a 2D quasi-Newton inversion algorithm with Broyden type Jacobian updating is used in order to image the electrical conductivity distribution of the soil column.

Contents

1	Introduction	3
1.1	Objectives	4
1.2	Outline	5
2	Historical Development and Theory of ERT and MMR	7
2.1	Historical Development of the Electrical Methods	7
2.2	Theory of the Resistivity Method	8
2.3	Historical Development of Magnetometric Resistivity	10
2.4	Theory of Magnetometric Resistivity	13
2.4.1	MMR Data and a 1D Layered Earth	14
2.4.2	MMR Data and Scaled Conductivity Contrasts	15
2.5	Combining ERT and MMR: The MERIT System	16
2.6	Forward Solutions for the Electric Problem	17
2.6.1	Analytical Solution of the Forward Problem	17
2.6.2	Numerical Solution of the Forward Problem	18
2.7	Comparison Between Analytical and Numerical Solution	19
3	Development of the MERIT Measurement System	21
3.1	Magnetic Sensors	22
3.2	Magnetoresistive Sensors	23
3.2.1	The Magnetoresistive Effect	23
3.2.2	AMR Sensor Layout	26
3.2.3	Magnetic Sensor Noise Spectra	26
3.3	Magnetic Sensor Modules	28
3.3.1	Sensor Stability	29
3.3.2	Lock-in Amplification	32
3.3.3	Displacement Currents	33
3.4	Electrical Potential Measurements	34
3.5	The Lab-scale MERIT Measurement Setup	35
4	Testing the Measurement System	37
4.1	Sensor Output Definitions	37
4.2	Magnetic Noise Sources	38
4.2.1	Environmental Disturbances	39
4.2.2	Anthropogenic Disturbances	39
4.2.3	Magnetic Noise Measurements	39

4.2.4	The Laboratory Background Noise	41
4.3	The Magnetic Field Due to a Reference Coil	43
4.4	Repeatability of a Measured Dataset	44
4.5	The MERIT Measurement Scheme	45
4.6	Numerical Magnetic Fields Compared to Real Data	47
4.6.1	The Conductive Rod Modelled	47
4.6.2	The Conductive Rod Measured	48
5	Optimisation and Resolution of the MERIT System	50
5.1	Background Mathematics	50
5.1.1	Singular Value Decomposition	51
5.1.2	Jacobian Calculation	53
5.1.3	The Effective Independence Distribution Matrix	54
5.1.4	Adaptations and Assumptions in EID Calculation	56
5.1.5	Resolution Calculation	57
5.1.6	The Singular Value Threshold	58
5.2	The Optimal Measurement Configuration	58
5.2.1	Horizontal Current Injection Scenarios	59
5.2.2	Vertical Current Injection Scenarios	66
5.2.3	Concluding Remarks on the Optimum Configuration	69
5.3	Resolution of the MERIT System	71
5.3.1	Resolution of Homogeneous Scenarios	71
5.3.2	Resolution of the Resistive Shield Scenario	73
5.3.3	Resolution of the Conductive Shield Scenario	76
5.4	Under-determined Systems and Resolution Matrix Rank	77
5.4.1	MMR Datasets	77
5.4.2	ERT Datasets	79
5.4.3	MERIT Datasets	79
5.4.4	The singular value threshold revisited	80
5.4.5	Concluding Remarks on the Resolution	81
6	Synthetic Data Inversion	82
6.1	The Quasi-Newton Inversion Algorithm	82
6.2	Weighting Electric and Magnetic Data	84
6.3	Synthetic Data Inversion Test Scenarios	85
6.3.1	Inversion Scenarios	85
6.3.2	Shielded Body Scenario	89
6.4	Inversion of Noisy Data	91
6.5	Horizontal and Vertical Current Injections Revisited	92
6.6	Concluding Remarks on Inversion	94
7	Discussion and Recommendations	95
8	Summary and Conclusions	98
9	Acknowledgements	99
10	References	101

Chapter 1

Introduction

The near subsurface is the part of the subsurface that bears most of the burden relating to anthropogenic activity, in the form of contaminations due to waste or chemical spills. Also the ever increasing demand for clean water in industry, agriculture or as drinking water has a great effect on the near subsurface. Due to the increasing effect this part of the subsurface has on society in general, the need for accurate investigation methods is also increasing. Since many striking features are often closely linked with the water saturation of the soil or the presence of for instance clay or sand layers, the electrical conductivity can be a useful proxy in studying the subsurface.

The need for detailed knowledge of the subsurface combines several scientific disciplines in a joint effort to understand the structure and behaviour of the soil. The soil is thus seen as a delicate interaction of physical, chemical and biological activity all set in a (hydro-) geological scenario, and is studied by the relative new field of hydrogeophysics (see for instance Vereecken et al., 2004 and 2004b). Geophysics is implemented in this field in several ways, first of all the characterisation of the subsurface in a non-invasive way (see for instance Telford et al., 1990 or Reynolds, 1997). More focussed on groundwater studies (see Berthold et al., 2004, Furman et al., 2004 or Liu and Yeh., 2004) are the monitoring or remediation of contaminants (Daily et al., 2004 and Bentley and Gharibi, 2004), salt water intrusions or tracer plumes in groundwater (see Daily et al., 1992 or Kemna et al., 2002).

The study of soil and groundwater related problems is not new in geophysics. In the early 1940's Archie (see Archie, 1942) already introduced an empirical relation describing the dependency of the (bulk) electrical conductivity on the pore fluid conductivity, matrix material and porosity, later known as Archie's law. This relation, developed for application in oil and gas reservoirs, could easily be implemented for problems concerning the near surface. In addition to theoretical considerations several geophysical techniques have been adapted from other branches of the mineral exploration industry, including techniques used to measure the electrical conductivity.

1.1 Objectives

The electrical conductivity (or its reciprocal the electrical resistivity) can be measured by so-called non-invasive methods, in which the electrical conductivity is measured directly on site. In general electrical (or its tomographical implementation: Electrical Resistivity Tomography, ERT) or electromagnetic (EM) surveys (see Telford et al., 1990) are carried out in order to map the subsurface electrical conductivity.

In electrical measurements a number of electrodes are inserted into the ground, and an electrical current is injected into the soil over two electrodes. The other electrodes are used to measure the electrical potential resulting from the injection. By using several electrode configurations the electrical conductivity of the subsurface at different depths can be obtained.

Electromagnetics uses a transmitter coil to generate an alternating electromagnetic field, which in its turn generates electrical eddy currents into the subsurface. These eddy currents have their own associated magnetic field, which interferes with the transmitted field. This combined field is measured by a receiver coil, and its phase and amplitude are then used to calculate the subsurface electrical conductivity.

In this thesis a third non-invasive technique is discussed which was developed parallel to the electrical resistivity methods in the early days of exploration geophysics (see Jakosky, 1933), but slowly disappeared from the geophysical landscape. Difficulties in the application and processing of measurement technique were cause of the lagging behind of this method in comparison to other exploration techniques.

The Maxwell equations establish a clear connection between electrical and magnetic fields, every current flowing through a medium also is accompanied by a magnetic field. This magnetic field also contains information on the electrical current density and thus on the electrical conductivity distribution in the medium. In the magnetometric resistivity method (or MMR, see Nabighian, 1991) the measurement of this magnetic field due to a current injection into the subsurface is used to obtain this information. Only due to the recent increase in computing power and the availability of reliable and accurate magnetic field sensors, MMR has returned in the focus of exploration geophysicists (Boggs, 1999, Chen et al., 2002 and Rubin and Hubbart, 2005). In addition to the increasing interest in MMR in geophysics there is also an interest in the field of non-destructive testing (Nazarov et al, 2004) and the medical field, where the need for non-invasive methods is even greater than in geophysics (see Levy et al., 2002).

Since the current used in electrical methods can also be used as source for an MMR signal, both measurements can be combined to obtain a better understanding of the electrical conductivity distribution. This thesis therefore describes the development of the laboratory scale setup of the so-called magneto electrical resistivity imaging technique (MERIT for short, see Kulesa et al., 2002), in which the two methods of ERT and MMR are combined. The aim is to increase the resolution capabilities of the system by the implementation of an additionally measured parameter. The magnetic field measurements have several advantages compared to the measurement of the electrical field. In electrical measurements the data consists of electrical potential differences, which greatly reduces the amount of data, since every data point consist of two measurements. The magnetic field can be measured in three orthogonal components, generating at every measured location three data points. Also differences in sensitivity in both techniques can lead to an increase in resolution. The true non-invasive nature of magnetic field measurements is a large advantage when compared to ERT. Since the magnetic fields also are present outside the studied volume no actual contact with the object is necessary. Therefore the amount of possible measurement locations is increased greatly.

The study presented in this thesis describes three years of cooperative work between the Central Institute for Electronics (Zentral Institut für Elektrotechnik) and the Agrosphere Institute, Institute for Chemistry and Dynamics of the Geosphere (Institut Agrosphäre, Institut für Chemie und Dynamik der Geosphäre). The institutes are part of the Research Centre Jülich in Jülich, (Forschungszentrum Jülich GmbH.), one of the Helmholtz Research Centres in Germany. Both institutes were involved in design and development of the measurement system, the sensor modules used in the MERIT system and the routines used in processing of the data. This work can be seen as the first steps in an ongoing project to increase the imaging capabilities of hydrological processes by implementation of geophysics, in which MERIT is used to characterizes the electrical conductivity. Further work includes for instance the linking of spectral induced polarization parameters to hydrological parameters (see Münch et al., 2005).

1.2 Outline

This thesis will start by introducing the two different components of MERIT, by describing the physical laws of the electrical and magnetometric methods, in addition a short overview of the historical developments of both systems will be given. The numerical forward model used in this study is also presented in this chapter. The third chapter will deal with the designed measurement system. Since the MERIT system is a completely new system, several technical developments had to be made in order to obtain a good data quality. The tests of the system itself (with main focus on the measurement of the magnetic fields) will be shown in the fourth chapter, the measurement scheme will be described as well as the effect of magnetic noise and possible sources of noise. In addition the developed measurement system will be tested against the numerical

algorithms used in the modelling, and vice versa. In the fifth chapter a study for the optimum measurement configuration (in terms of current injection dipole and measurement locations) will be shown, and synthetic data will be used to demonstrate the increase in resolution of a MERIT dataset in comparison with traditional ERT or MMR data. Chapter five also will deal with importance of the singular values of a given dataset on its resolving power and the amount of information present. The sixth chapter describes a fundamental inversion routine, which can be used to obtain an image of the electrical conductivity distribution of a 2D plane through a synthetic soil column. Conclusions and recommendations for further research can be found in chapters seven and eight.

Chapter 2

Historical Development and Theory of ERT and MMR

In this chapter the two geophysical methods incorporated into the MERIT system will be described and compared: electrical resistivity tomography and magnetometric resistivity. Traditionally resistivity measurements (or the tomographic implementation: electrical resistivity tomography (ERT)) is used to map subsurface conductivity distributions. Historically the method of magnetometric resistivity (MMR) was developed for the same purpose. Since this method is rather unknown the main focus will lie on the MMR part of the MERIT system.

At first a short history of the development of each technique will be given, secondly the focus will turn to the physical relations on which both methods are based. The differences between MMR and electrical resistivity will be highlighted from a physical point of view and finally the numerical algorithm developed for modelling purposes (see Tillmann et al., 2003) will be described.

2.1 Historical Development of the Electrical Methods

Electrical resistivity, or geoelectrics is an often used method in near surface geophysics with a relative long history in exploration geophysics. Already around 1912 Conrad and Marcel Schlumberger started experimenting with the measurement of subsurface electrical resistivity. A measurement basically incorporates four electrodes, where two are used for current injection, the other two are used to measure the electrical potential difference, related to the current injection. Over the years several different current injection patterns emerged, each with its distinct advantages and disadvantages in sensitivity or practical use (Telford et al., 1990 and Reynolds, 1997). Data processing involved the matching of datasets to pre-calculated type curves of known electrical conductivity distributions

The increase in computing power and availability of reliable multichannel measurement system allowed measurement and processing of more dimensions as compared to the 1D methods of the 80's (images of resistivity versus depth for instance). Secondly the numerical implementation of physical laws for two or three dimensional structures (see Dey and Morrison., 1979) allowed the development of numerical inversion routines, for characterisation of the subsurface electrical conductivity distribution. The combination of borehole and surface electrodes introduced the true tomographic implementation of electrical measurements (known as ERT). In contrast to tomographic methods, as implemented in X-ray or seismic tomography (see Dines and Lytle, 1979), ERT cannot use back-projection along the paths of electrical current. The electrical current trajectories are not straight (as X-rays or seismic waves are), therefore at first the problem has to be approximated by linearization before an inversion routine can be implemented (see for instance Daily and Owen, 1991). This information allows the inversion routine to image the subsurface electrical conductivity distribution by means of an iterative process where a model is matched to the measured data.

Electrical resistivity methods have also found their way in the field of medicine (often known there as electrical impedance tomography, see for instance Malmivuo and Plonsey, 1995), technical applications (i.e. non-destructive testing) or industrial processes (in observation of fluid mixing in vessels or pipes for instance).

2.2 Theory of the Resistivity Method

The electrical resistivity method has been described in several geophysical textbooks (for instance Telford et al., 1990 or Reynolds, 1997) and will only be touched upon in this section.

In any given body, either the subsurface or a defined volume in a laboratory, a DC current is injected through electrodes at the surface. At several other electrode pairs the electric potential is measured. With the use of Ohm's law the current density $\vec{J}(r)$ and electric field $\vec{E}(r)$ can be linked by the electrical conductivity distribution $\sigma(\vec{r})$:

$$\vec{J}(r) = \sigma(\vec{r})\vec{E}(r) \quad (2.1)$$

Writing the electric field as the electrical potential $U(\vec{r})$ the following equations can be obtained,

$$\begin{aligned} \vec{E}(r) &= -\nabla U(\vec{r}) \\ \vec{J}(r) &= -\sigma(\vec{r})\nabla U(\vec{r}) \end{aligned} \quad (2.2)$$

Assuming no accumulation of electrical charge (Q) due to the current density $\vec{J}(r)$, the divergence of $\vec{J}(r)$ can be written as:

$$\begin{aligned} \nabla \cdot \vec{J} &= \frac{\partial Q}{\partial t} = I_{inj} \quad \text{at a single current injection point} \\ \nabla \cdot \vec{J} &= 0 \quad \text{everywhere else} \end{aligned} \quad (2.3)$$

Where I_{inj} is the current injected at a single electrode and $\frac{\partial}{\partial t}$ denotes the time derivative. Inserting equation 2.3 into equation 2.2 and rewriting the equation with basic vector algebra the following equation can be obtained:

$$\nabla\sigma \cdot \nabla U + (\sigma\nabla^2 U) = -I_{inj}\delta(\vec{r} - \vec{r}_s). \quad (2.4)$$

The Dirac delta function is denoted by δ here, and the injection electrode is located at \vec{r}_s . If σ is taken constant over the whole space, the Laplace equation is obtained for every where except at the injection electrode ($\nabla^2 U = -I_{inj}\delta(\vec{r} - \vec{r}_s)$).

After limiting the volume to a half-space (by the introduction of free air where $\sigma = 0$) and application of suitable boundary conditions ($\frac{\partial U}{\partial z} = 0$ at $z = 0$) the electric potential can be written as:

$$U(\vec{r}) = \left(\frac{I_{inj}}{2\pi\sigma}\right) \frac{1}{r} \quad (2.5)$$

Normally in the field case two electrodes (a source and sink, depicted C_1 and C_2 , see figure 2.2) are used for current injection (I_{inj}). By application of super positioning the electrical potential can be calculated for the two electrode case from equation 2.5. Since the injected current flows into the ground at C_1 and leaves the subsurface at C_2 , the injected current has the opposite sign in the electric potential at C_2 .

Now the electrical potential between the two measurement electrodes (ΔU) due to injection current I_{inj} can be written as:

$$\Delta U = \frac{I_{inj}}{2\pi\sigma_a} \left[\left(\frac{1}{r_1} - \frac{1}{r_2} \right) - \left(\frac{1}{r_3} - \frac{1}{r_4} \right) \right] \quad (2.6)$$

Where r_i denote the distances from one electrode to the other (see also figure 2.2). From this equation the apparent conductivity (σ_a) can be obtained. In case of a homogeneous electrical conductivity distribution, this apparent conductivity is equal to the true electrical conductivity of the subsurface. If the subsurface has a heterogeneous electrical conductivity distribution, the apparent electrical conductivity is a bulk conductivity which incorporates the geometry of the measurement. It is an equivalent homogeneous conductivity, giving rise to the same electric potential as the real inhomogeneous subsurface. By implementation of inversion techniques the apparent conductivity can be used to obtain the actual electrical conductivity of the subsurface or volume.

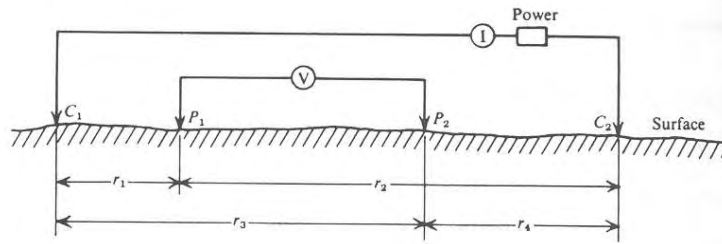


Figure 2.1: Electrode layout for a typical resistivity survey, (after Telford et al., 1990). $C_{1,2}$ denote the current injection electrodes, $P_{1,2}$ the potential electrodes, $r_{1,2,3,4}$ are arbitrary lengths (m).

2.3 Historical Development of Magnetometric Resistivity

The magnetometric resistivity method is primarily based on the patent of Jakosky from 1933 (see Jakosky, 1933), in which he describes a system to measure the deviations from the earth's magnetic field under influence of a DC or low frequency AC (up to 100 Hz) current injection through two electrodes in the subsurface. For the field implementation of the MMR method his horseshoe layout (see figure 2.2) of the cables and the measurement of the magnetic field along parallel lines has basically remained the same over the years. The main advance lies in the development of magnetic sensors and electromagnetic theory (and thus modeling and processing of MMR datasets). Where Jakosky had to measure the magnetic field with free-hanging bar magnets or vibrating string magnetometers, nowadays a large range of highly sensitive magnetic sensors are available (see Ripka, 2001).

Also in the 1930's the Romanian scientist Stefanescu worked on the theoretical background of the geophysical application of magnetic fields due to subsurface current flow. For almost forty years a continuous science program concerning magnetometric resistivity was pursued by the group around Stefanescu (see Nabighian, 1991). This led to a whole range of type curves for simple geological scenarios, similar to the type curves used in resistivity at the time. In 1974 the company Scintrex developed a highly sensitive fluxgate magnetometer, allowing detailed MMR studies to be undertaken (see Edwards, 1974). Parallel to this development in MMR a closely related method emerged, magnetic induced polarization (MIP, see Seigel, 1974). This method is the magnetic field equivalent of the induced polarization method (IP) and is as closely linked to MMR as IP is to standard resistivity (see Fink et al., 1990).

May 2, 1933.

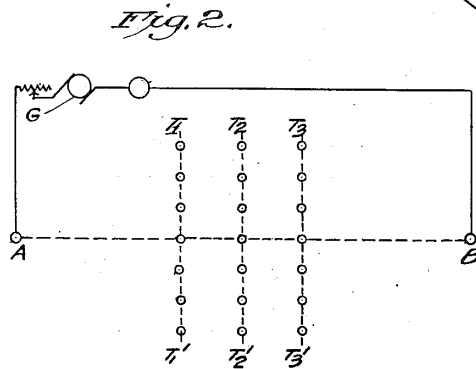
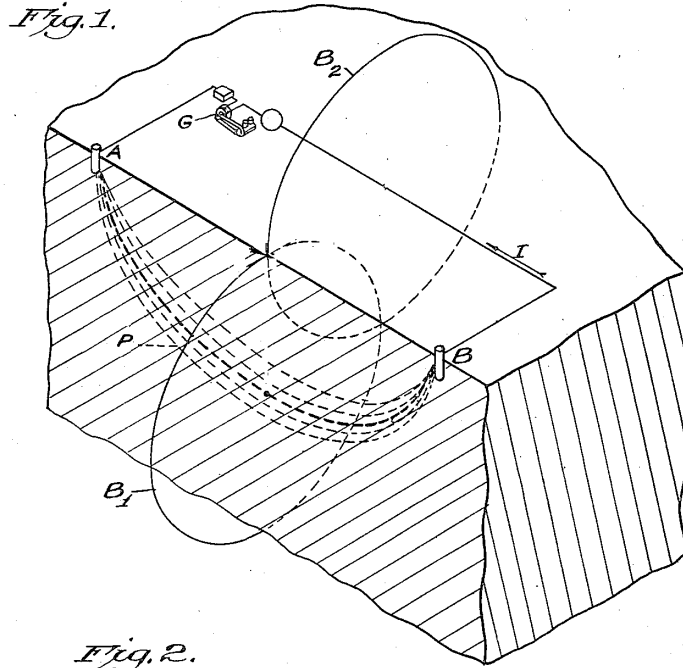
J. J. JAKOSKY

1,906,271

METHOD AND APPARATUS FOR DETERMINING UNDERGROUND STRUCTURE

Filed June 1, 1931

4 Sheets-Sheet 1



INVENTOR,
John J. Jakosky,
 BY *Nathan P. Shinsky and*
Alfred W. Knapp
 ATTORNEYS.

Figure 2.2: Original MMR measurement setup by Jakosky, Figure 1 shows the 'horseshoe' type of measurement configuration and explain the current flow paths through the subsurface (P), its resulting magnetic field B_1 and the magnetic field due to the wire B_2 . A current generator is depicted by G , which is connected to the injection points A and B . Figure 2 shows a typical MMR survey setup, with measured lines $T_{1,2,3}$ - $T_{1,2,3}$ between current injection electrodes A and B (adapted from U.S. Patent 1.906.271).

Around mid 1970's both Edwards (see Edwards, 1974) and Seigel (see Seigel, 1974) pointed out that MMR could be superior to traditional resistivity soundings in mapping shielded conductivity distributions. When an inhomogeneity is buried beneath a conductive overburden, traditional resistivity has difficulty in penetrating below the overburden, whereas MMR has less problem due to loss of signal. Ever increasing amount of data sets and availability of more sensitive magnetometers led to a whole range of applications in the late 1970's (Edwards and Howell., 1976, Edwards et al., 1978 and Gómez-Trevino and Edwards, 1979). In the early 1980's MMR was also taken into the field of offshore geophysics (see Edwards et al., 1984 and Edwards et al., 1985). The lack of needing physical contact with the subsurface (as is needed in resistivity surveys) except for a limited amount of injection electrodes, makes MMR ideal as a borehole tool, as described by Acosta and Worthington, 1983. They also pointed out the sensitivity of magnetic fields to concentrated current within a resistive media, allowing MMR to perform better in high resistive media than resistivity methods.

In the time ranging from mid 1980's to mid 1990's the MMR method gradually disappeared from the applied geophysical landscape, only to be picked up again in the late 1990's by the University of New England and Flinders University in Australia (see Cattach et al, 1993, Cattach, 1996, Boggs, 1999 and Fathianpour, 1997), the University of British Columbia, Canada (see Chen et al., 2002 and Chen et al., 2004) and the company Multi-Phase Technologies, LLC in the USA (see Svoboda et al., 2002, Labrecque et al., 2002 and Labreque et al., 2003). In addition to the surface based MMR techniques, the field of borehole geophysics also benefits from the new interest in MMR (Elders and Asten, 2004) as an additional tool for electrical conductivity measurements next to borehole EM. The development of new numerical techniques, increases in computational power and ever increasingly more sensitive magnetometers made the application of MMR again an interesting option. Kulesa et al., 2002 introduced the Magneto-Electrical Resistivity Imaging Technique in which the combination of both MMR and ERT was placed in a hydrogeophysical context. The truly non-invasive character of the MMR technique can provide a large amount of information concerning flow and transport processes in soil columns, as well as on the field scale. The combined measurement of the electrical potential and the magnetic field yields complementary information which will increase the resolving capabilities in comparison to ERT datasets.

Similar as in the case of the electrical methods, MMR has also found its way in other branches of science, for instance in non destructive testing (see Nazarov et al, 2004) or medicine (Levy et al., 2002).

2.4 Theory of Magnetometric Resistivity

The following section will describe the physical background on which MMR is based. In addition several disadvantages inherent in the method it self, due to the physical relations, will be highlighted. The described theory will closely follow Nabighian, 1991.

The magnetic field (\vec{B}^1) due to a steady volume current² for a general case is given by the Biot-Savart law:

$$\vec{B}(\vec{r}) = \frac{\mu}{4\pi} \int_V \frac{\vec{J}(\vec{r}') \times (\vec{r} - \vec{r}')}{|\vec{r} - \vec{r}'|^3} dV', \quad (2.7)$$

where μ is known as the magnetic permeability, $\vec{J}(\vec{r})$ the current density, \vec{r}' a vector pointing to the volume element, \vec{r} a vector pointing to the magnetic sensor position and finally dV' a volume element (in the space spanned by the unit vectors of \vec{r}'). For most non-magnetic soils, the magnetic permeability of free space, $\mu_0 = 4\pi \times 10^{-7} [\frac{N}{A^2}]$ can be chosen, and disappears from the equation as free parameter. With basic vector algebra equation 2.7 can be rewritten into:

$$\vec{B}(\vec{r}) = \frac{\mu}{4\pi} \int_V \vec{J}(\vec{r}') \times \nabla' \frac{1}{|\vec{r} - \vec{r}'|} dV' \quad (2.8)$$

For a steady current, this volume integral can be transformed into a volume and a surface integral, first by applying the basic vector identity (for an arbitrary vector $\vec{\eta}$ and an arbitrary scalar ϕ):

$$\nabla' \times (\phi \vec{\eta}) = \phi \nabla' \times \vec{\eta} - \vec{\eta} \times \nabla' \phi \quad (2.9)$$

and secondly applying Stokes theorem. Thus equation 2.8 can be rewritten as:

$$\vec{B}(\vec{r}) = \frac{\mu}{4\pi} \int_V \frac{\nabla' \times \vec{J}(\vec{r}')}{|\vec{r} - \vec{r}'|} dV' - \frac{\mu}{4\pi} \int_S \frac{\vec{n} \times \vec{J}(\vec{r}')}{|\vec{r} - \vec{r}'|} dS' \quad (2.10)$$

Here the surface S denotes the bounding surface of the volume V and $\vec{n}(\vec{r}')$ is a unit vector along the outward normal to S . Inside any volume we may define an electrical potential $U(\vec{r}')$ for a steady current which relates the current density distribution to the electrical conductivity distribution $\sigma(\vec{r})$.

Further more, the volume V can thus be chosen that it is slightly larger as the volume in which the conductivity distribution is located. This causes $\vec{J} = 0$ everywhere along the boundary, and allows to negate the surface integral in equation 2.8. Rewriting equation 2.8 and introducing the results from Ohm's

¹Although officially the parameter \vec{H} is used to quantify the magnetic field, and $\vec{B} = \mu \vec{H}$ is known as the magnetic flux density, \vec{B} is the fundamental quantity concerning magnetic fields, and will therefore in this thesis continually be used to describe the magnetic field.

²With the term steady current, a current stationary in both time and space is meant (see Griffiths, 1989).

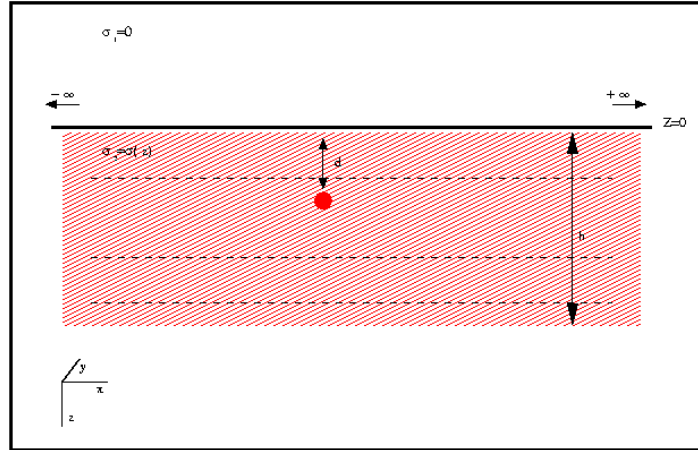


Figure 2.3: Geometry used in calculation, the red dot indicates a current source

law (equation 2.2), the magnetic field can be related to the electrical conductivity distribution in a known volume.

$$\overline{B}(\vec{r}) = \frac{\mu_0}{4\pi} \int_V \frac{\nabla' U(r') \times \nabla' \sigma(r')}{|\vec{r} - \vec{r}'|} dv' \quad (2.11)$$

Comparing the MMR with the ERT method several differences become apparent, the underlying physics is cause of differences in sensitive behaviour. In the final equations, in case of ERT equation (2.2) and in case of MMR equation (2.11), the first difference is apparent, MMR data does not contain information on the electrical conductivity distribution itself but on the gradient of the electrical conductivity.

The MMR method has several insensitivities not occurring in ERT when electrical conductivity is concerned. Two main differences occur, MMR is insensitive to horizontally layered media and it is physically impossible for the magnetic field to change when the electrical conductivity is changed by a scaling factor. The consequences of both insensitivities will be described in the following subsections.

2.4.1 MMR Data and a 1D Layered Earth

Already in the work of Stefanescu considerations on the insensitivity of the magnetic field to a horizontally stratified subsurface are included. Stefanescu (and later Nabighian, 1991) based his proof on symmetry and Ampère's law. Here, the mathematical proof will be given, based on the work of Inayat-Hussain, 1989.

If equation (2.10) is taken, and Ohm's law (equation (2.2)) is inserted, the complete equation can be transformed into cylindrical coordinates ($\vec{B} = B(R, \theta, Z)$).

Since we are dealing with a 1D earth (see figure 2.3), we can write for a sub-surface layer (consisting of several sublayers), with depth h , the electrical conductivity distribution as $\sigma(z)$. The layer itself is located in a halfspace.

After implementing the symmetry conditions to exclude the θ component of \vec{B} , introduction of Bessel functions and insertion of boundary conditions the following equation can be obtained (see Inayat-Hussain, 1989):

$$\begin{aligned} \vec{B} \equiv B(R, Z)\hat{\theta} = & \\ -\mu_0 [H(Z) - H(Z - h)] \sigma(Z) \cdot \int_0^\infty d\lambda J_1(\lambda R) \left(\frac{\partial}{\partial Z} \right) v(\lambda, Z) & \quad (2.12) \\ + \frac{\mu_0 \text{sign}(d-Z)}{4\pi R} \left(1 - \frac{|d-Z|}{(R^2 + (d-Z)^2)^{\frac{1}{2}}} \right). & \end{aligned}$$

where $\hat{\theta}$ is the unit vector in θ direction, $H(z)$ a Heaviside function ($H(z > 0) = 1$ and $H(z < 0) = 0$) and $\text{sign}(z)$ a sign function. The depth of current injection is denoted by d , $J_1(\lambda R)$ a first order Bessel function and $v(\lambda, Z)$ is the Hankel transform of the electric potential.

Studying the first term of equation (2.12) in detail it now becomes obvious that in the region $Z < 0$, or $Z > h$ the first term vanishes and so does the dependency on the electrical conductivity $\sigma(Z)$.

Thus is shown that the magnetic field due to a horizontally stratified medium does not produce any response, rendering the MMR method insensitive to horizontally stratified media if the magnetic field is measured above ($Z < 0$) or below ($Z > h$) the stratified layer. The magnetic field is only sensitive to horizontal stratification if it is measured within the stratified layer ($0 < Z < h$).

2.4.2 MMR Data and Scaled Conductivity Contrasts

The magnetometric resistivity method is also insensitive between two models where the electrical conductivity contrast only differs by a constant scaling factor a (see Chen et al., 2002). The cause of this phenomenon can be observed from the Maxwell equations themselves.

Amperè's law (see Griffiths, 1989) states:

$$\nabla \times \vec{H} - \sigma(r)\vec{E} = \vec{J}_s \quad (2.13)$$

Where \vec{J}_s depicts the current due to the current injection through the two electrodes. By writing $\vec{E} = -\nabla U$ and, application of the boundary condition, we can obtain the electrical potential U . Inserting the value for U into equation 2.13 the magnetic field can be obtained by solving:

$$\nabla \times \vec{B} = \vec{J}_s - \sigma \nabla U = f \quad (2.14)$$

Where a source term f can be introduced, satisfying $\nabla \cdot f = 0$. If a new conductivity model differing only a constant factor a , such that $\sigma_2(r) = a\sigma_1(r)$, is chosen and insert it into equation (2.13). It can easily be shown by taking

the divergence of equation 2.14 that $\sigma_1(r)\nabla U_1 = \sigma_2(r)\nabla U_2$ since the injected current \vec{J}_s will remain constant:

$$\nabla \cdot (\sigma_1(r)\nabla U_1) = \nabla \cdot \vec{J}_s = \nabla \cdot (\sigma_2(r)\nabla U_2). \quad (2.15)$$

With both terms of the source term f unchanged, the magnetic field remains unchanged too (see equation 2.14 and equation 2.7). Thus indicating the insensitivity of MMR data to the absolute conductivity of the subsurface.

2.5 Combining ERT and MMR: The MERIT System

The magneto-electrical resistivity imaging technique (MERIT) combines the measurement of the electrical potential and the magnetic field due to a current injection. With the increased focus of geophysics on MMR (see Chen et al., 2002, Labrecque et al., 2002 and Labrecque et al., 2003) the goal of increasing the resolution of ERT surveys by the addition of MMR data is apparent. In this thesis the MERIT system will be limited to cylindrical samples (with 0.1 m radius and 0.5 m height). Similar as in the case of both ERT and MMR, the technique itself is not limited to the laboratory scale, and can also be implemented on the mineral exploration scale for instance (see Cattach et al, 1993).

In combining both methods the additional information inherent in the magnetic field data can be used to increase the resolution of the system. Each magnetic measurement point will lead to the addition of three measured values (the three magnetic field components) to the system of equations. By introduction of the magnetic field data the size of the dataset is increased considerable, which also can lead to an increase in resolution.

Another advantage of the magnetic field measurements is the true non-invasive nature of the measurements. No need for a physical connection between sample and sensor is necessary (except for the current injection electrodes). This allows the magnetic field to be measured at every available position. A free moving vertical scanning system is therefore designed, to allow a great flexibility concerning the measurement location of the magnetic field.

The sample volume for which this MERIT system is designed is a typical size for laboratory scale hydrological experiments. The non-invasive character of the magnetic field part of MERIT gives an additional advantage on this scale. The presence of a large number of electrodes, as used in ERT to obtain an image of the electrical conductivity, will influence the water flow through the column considerable. The scanning system itself allows relative fast measurements, which is also necessary in flow experiments.

2.6 Forward Solutions for the Electric Problem

The goal of the measurements of both electrical potential and magnetic field is to obtain an image of the subsurface electrical conductivity distribution. In order to obtain such an image a forward modelling algorithm needs to be developed which can be implemented into an inversion scheme (which will be described in chapter 6). In this section the algorithms used in both numerical modelling and the actual inversion will be described, and a comparison between the numerical and the analytical solution will be made.

2.6.1 Analytical Solution of the Forward Problem

The analytical solution for the electrical field in a 3D cylindrical object due to a dipole current injection has been well studied. In the study of the physical properties of for instance core samples (see Lytle et al., 1979), but also in the fields of medicine and industrial process tomography the use of cylindrical volumes is well known. In this section only the calculations of the electric field will be shown. The step from electric field to magnetic field (i.e. equation 2.11) is similar for both analytical and numerical solutions. A solution for the volume integral in equation 2.11 cannot be easily implemented in a true analytical sense. Therefore this step will be omitted in this comparison, and only the electrical potential will be compared.

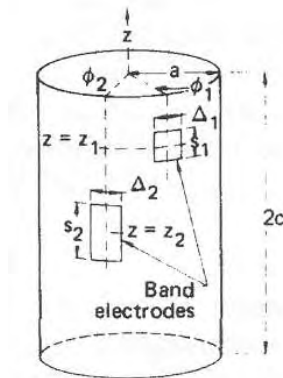


Figure 2.4: Electrode configuration for analytical calculations, after Lytle et al., 1979.

Lytle et al., 1979, provided the analytical solution for a DC current injection in a similar setup as the numerical solution of the MERIT system (see figure 2.6.1). The two injection electrodes with dimensions $(s_{1,2} \times \Delta_{1,2})$ are located at the surface of the cylinder at a height $z_{1,2}$ below the cylinder top. The cylinder itself has a radius of a and a height of $2c$. This leads to a forward problem where the Laplace equation has to be solved for inhomogeneous Neumann boundary conditions. Since the choice of cylindrical coordinates is obvious, the Laplacian

will be directly expressed in cylinder coordinates:

$$\nabla^2 U = 0 = \frac{1}{r} \frac{\partial}{\partial r} \left(r \frac{\partial U}{\partial r} \right) + \frac{1}{r^2} \frac{\partial^2 U}{\partial \phi^2} + \frac{\partial^2 U}{\partial z^2} \quad (2.16)$$

With the following boundary conditions:

$$\begin{aligned} \frac{\partial U}{\partial n} &= 0 && \text{for boundary elements not containing electrodes} \\ \sigma \frac{\partial U}{\partial n} &= J && \text{for boundary elements where the electrodes are located} \end{aligned} \quad (2.17)$$

The partial derivative $\frac{\partial}{\partial n}$ depicts the normal derivative to the surface, σ the electrical conductivity and J the injected current density distribution.

If the two electrodes (see figure 2.6.1) have the same size ($s_1 = s_2 = s$, $\Delta_1 = \Delta_2 = \Delta$ and $z_1 = z_2 = Z$), the electrical potential distribution in the column can be written in cylinder coordinates as:

$$\begin{aligned} U(\rho, \phi, z) = & \\ & - \sum_{r=1}^{\infty} \sum_{n=0}^{\infty} \left[\left(\frac{4Ic \cos\left(\frac{r\pi z_1}{c}\right) \sin\left(\frac{r\pi s}{2c}\right) \sin\left(\frac{n\Delta}{2a}\right) B_n(r\rho c)}{\sigma \pi^3 r^2 n s \Delta (1 + \delta_{0n})} \frac{B_n(r\rho c)}{B'_n(r\rho c)} \cos\left(\frac{r\pi z}{c}\right) \right) \right. \\ & \quad \left. (\cos(n(\phi - \phi_1)) - \cos(n(\phi - \phi_2))) + \right. \\ & \left(\frac{4Ic \sin\left(\frac{(2r-1)\pi z_1}{2c}\right) \sin\left(\frac{(2r-1)\pi s}{4c}\right) \sin\left(\frac{n\Delta}{2a}\right) B_n((2r-1)\pi \rho 2c)}{\sigma \pi^3 [(2r-1)/2]^2 n (1 + \delta_{0n}) s \Delta} \frac{B_n((2r-1)\pi \rho 2c)}{B'_n((2r-1)\pi \rho 2c)} \sin\left(\frac{(2r-1)\pi z}{2c}\right) \right) \\ & \quad \left. (\cos(n(\phi - \phi_1)) - \cos(n(\phi - \phi_2))) \right] - \\ & \sum_{n=1}^{\infty} \frac{aI}{\sigma \pi n^2 c} (\rho a)^n \left(\frac{\sin\left(\frac{n\Delta}{2a}\right)}{\Delta} (\cos(n(\phi - \phi_1)) - \cos(n(\phi - \phi_2))) \right) \end{aligned} \quad (2.18)$$

where, I is the total current strength injected, σ the (homogeneous) electrical conductivity, δ_{n0} the Dirac delta function ($\delta_{0n} = 1$ when $n=0$, otherwise $\delta_{0n} = 0$), B_0 the modified Bessel function and B'_0 its first derivative. When the internal electrical potential distribution is known, equation 2.11 can be used to calculate the magnetic field resulting from the current injection in the column.

2.6.2 Numerical Solution of the Forward Problem

Solving the forward problem with a numerical approach requires a discretization of the measurement volume, similar to the volume used in the analytical solution, (see Tillmann et al., 2003, and Tillmann et al., 2004). In the case of a cylindrical body this volume will consist of a combination of prisms and cubes (see figure 2.5, and Tillmann et al., 2003). In each element the electrical conductivity is held constant, the electrical potential inside the element is approximated linearly. The current electrodes are located on the outside of the cylinder as area electrodes, with dimensions equal to a single grid cell.

A finite element scheme (see Jin, 1993) is chosen to solve the forward problem, with similar boundary conditions as in the analytical case. Therefore a similar set of differential equations has to be solved as in equation 2.16, again with the Neumann boundary conditions (see equation 2.17).

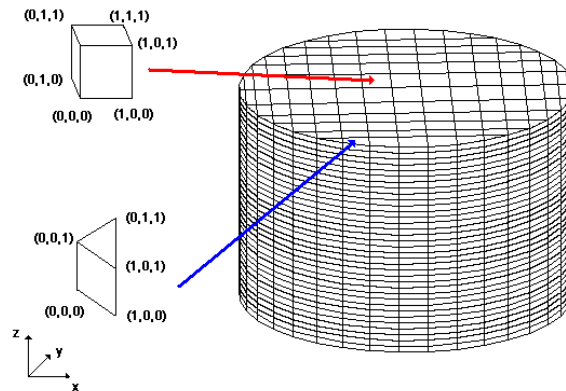


Figure 2.5: Finite element grid used in the numerical modeling of the MERIT system, after Tillmann et al., 2004

The Ritz method (see Jin, 1993) is used to formulate the system of equations and a conjugate gradient algorithm is used to solve the linear system of equations (see Barret et al, 1994). Similar as in the analytical solution the resulting electrical potential distribution can then be used to calculate the magnetic field at the outside magnetic sensors with the rewritten form of the law of Biot-Savart (see 2.11).

2.7 Comparison Between Analytical and Numerical Solution

In order to test the numerical algorithm a simple model was taken and a forward calculation was made (see Tillmann et al., 2003). The model consists of a homogeneous column with dimensions equal to the column used in the measurement setup itself (radius of 0.1 m and a height of 0.5 m). The surface electrodes used in both analytical and numerical solution had the size of an outer grid cell of the discretization grid used in the numerical solution. In order to test the analytical and numerical solutions both a horizontal and a vertical dipole were modelled. The horizontal dipole was placed in the middle of the column height and had a dipole length of 180 degrees (i.e. located at the opposite sides of the cylinder), the vertical dipole had a dipole length of 20 cm. The areas of the surface electrodes used in both modelling examples was set fixed at 1 grid cell, as was the injected current (100 mA). Data is presented as folded out cylinder mantles with 64 gridcells in the vertical and 48 in the horizontal direction.

Both the horizontal (figure 2.6) and the vertical injection dipole (figure 2.7) show similar features, the areas in close vicinity of the electrodes has the largest error percentage (up to 0.4 %), at all other locations the difference between numerical and analytical solution is negligible.

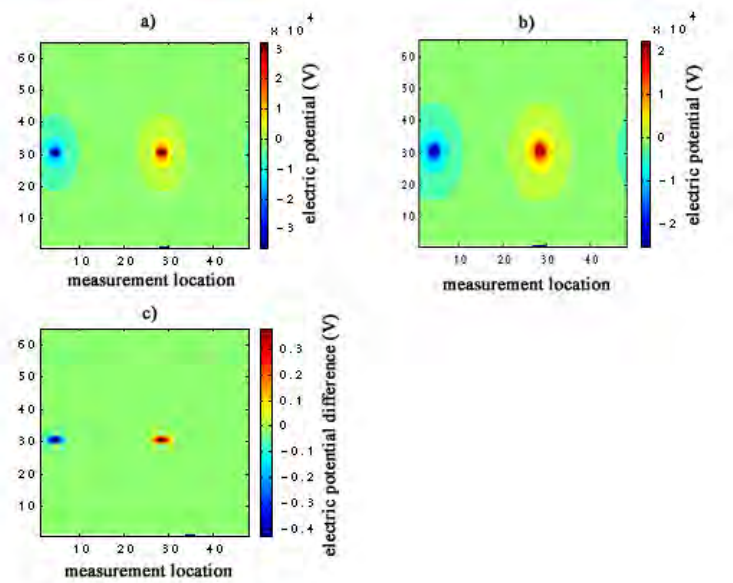


Figure 2.6: Electrical potential at the column mantle, a) the analytical solution, b) the numerical solution, c) the difference in % of the analytical solution

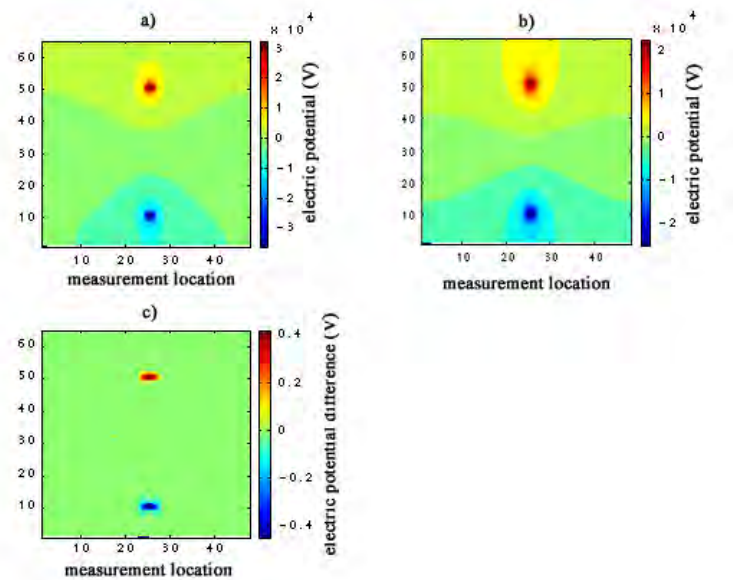


Figure 2.7: Electrical potential at the column mantle, a) the analytical solution, b) the numerical solution, c) the difference in % of the analytical solution

Chapter 3

Development of the MERIT Measurement System

In this chapter the hardware for the laboratory scale version of the magneto-electrical resistivity imaging technique (MERIT) will be described (see also Zimmermann et al., 2003 and Zimmermann et al., 2005). The development and design of the sensor modules, as well as the scanning system, is done in cooperation with the Central Institute for Electronics of the Research Centre Jülich.

As explained before the MERIT system combines the measurement of the electric and the magnetic field due to a current injection into a medium. The MERIT system developed in the course of this thesis, is designed to measure the electrical conductivity distribution of cylindrical volumes. The main requirement of the system will therefore be to accommodate cylindrical samples (with a radius of 0.1 m and 0.5 m height) with only a limited amount of electrodes available. Secondly the minimal resolution of the magnetic sensors was set at 50 pT, in order to be able to measure even the rather small magnetic fields with sufficient accuracy (see Tillmann et al., 2004). An additional requirement for the system is the ability to measure under typical magnetic noise conditions. This requirement was chosen for several reasons, firstly the development of a good magnetic shielding system is very complex and expensive (for instance magnetic shielding used in MEG (magnetoencephalography) systems or astrophysical observatories). Secondly since the technique MERIT is not limited to cylindrical samples, the system designed here will function as a prototype for larger systems, up to the field scale, where the chance of implementing a shielding system is negligible.

The main focus of this chapter will lie on the development of the magnetic sensor modules, since the other components (i.e. the ERT part and the measurement system itself) are more or less standard techniques. Therefore at first an overview will be given on typical magnetic sensors, followed by a more in depth discussion of the sensor type used (an anisotropic magnetoresistive sensor, AMR) in the MERIT system, since this is a relative unknown magnetic sensor in geophysics. Different type of AMR sensors will be described and

compared in terms of their noise spectra, and one AMR sensor will be chosen for implementation in the current MERIT system. The focus then changes to the development of the magnetic sensor modules, including the electrical components used to stabilize the sensor sensitivity or increase the signal to noise ratio. Finally the electrical potential measurements will be discussed and the complete MERIT system for small cylindrical samples will be introduced.

3.1 Magnetic Sensors

A wide range of magnetic sensors is available on the market, ranging from high-tech low temperature SQUIDs (Superconducting Quantum Interference Devices) to relative simple induction coils. In this section several magnetic sensor types will be compared on basis of a possible implementation in the MERIT system (for more in depth descriptions see Ripka, 2001 and Boll and Overschott, 1989 for instance).

Keeping in mind that the system is to be designed to operate under laboratory noise conditions, the high sensitivity of for instance SQUIDs (see Ripka, 2001) is not applicable for this type of measurements due to the absence of a shielding system, secondly the complexity of the operation of a SQUID based sensor system is huge (i.e. cooling the sensors down to 77 K for high temperature SQUIDs and 4.2 K for low temperature SQUIDs) which also implies the ineffectiveness of an array system based on SQUIDs. From an operation complexity point of view induction coils on the other hand are a good option, but the size of a three component coil system is rather large. This also makes this sensor type not applicable in a three component array based system on the scale of the MERIT system (e.g. soil columns with 0.1 m radius and 0.5 m height).

The size of the sensors plays a rather important role, since the scale of the MERIT system is in the order of tens of cm, the dimensions of the magnetic sensor have to be known accurately. With large sensors, the measured magnetic field will be averaged over a large volume (the dimensions of the actual sensor head), causing errors due to uncertainty in the location of the sensitive magnetic axis. The smaller the sensor itself, the better the position of the sensitive axis is known.

Traditionally the use of fluxgate, proton or cesium vapor sensors is wide spread in geophysics. At low frequencies all sensors mentioned are slightly more sensitive than coils, but have less sensitivity in comparison to coils at high frequency. Again, the size of the sensors is a disadvantage in implementations on the scale of the current lab-scale MERIT system.

Microchip based sensors do not have the size problems related to other sensors, also they can easily be implemented on a circuit board, and the costs are relatively low, making them ideal targets for an array based system. Although Hall sensors are chip based, the sensitivity of a Hall sensor is much too low for

implementation in this system. Two options of chip-based sensors then remain, anisotropic magnetoresistive sensors (AMR) and giant magnetoresistive sensors (GMR).

3.2 Magnetoresistive Sensors

The magnetoresistive effect has first been described in 1857 by Lord Kelvin (see Thomson, 1857) and describes the changes in electrical resistivity of a medium due to an outside magnetic field. The technical advances in the field of microelectronics and demand for miniaturization revived his ideas in the last three decades. Nowadays magnetoresistive sensors are implemented in a variety of electronic systems. Common implementations are: reading-heads for data storage systems, magnetic positioning, navigation and electrical current measurements (see Ripka, 2001, Boll and Overschott, 1989 and Tumanski, 2001). Since magnetoresistive sensors are relatively unknown in geophysical implementations, this section will deal with the physical background of the magnetoresistive effect, and the structure of the sensors itself.

3.2.1 The Magnetoresistive Effect

In general three different physical processes give rise to the magnetoresistive effect. The Lorentz force, associated with magnetic fields and moving electric charges, generates a torque and extends the current paths in any conductor, causing the electrical resistance to increase (see figure 3.1). This change is proportional to $(\mu \cdot |B|)^2$ where μ is the electron mobility, and $|B|$ the amplitude of the magnetic flux density (see Boll and Overschott, 1989). Since the electron mobility in metals is low, this effect, known as the Hall effect, can be neglected in AMR sensors (which are metal based).

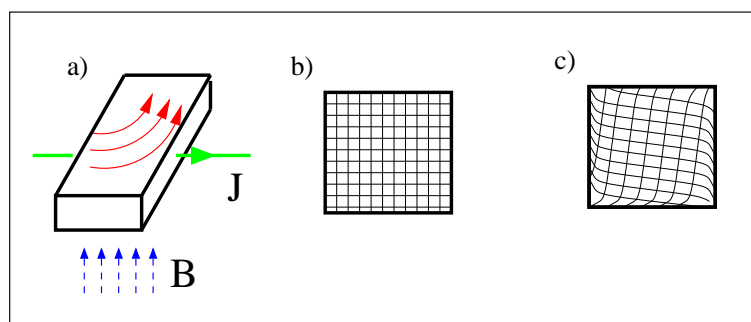


Figure 3.1: The magnetoresistive effect in semiconductors; a) electron movement (in red) due to the Lorentz force associated to the magnetic field (B , in blue) on current J (green). b) current paths and equipotential line in a rectangular plate semiconductor. c) current paths and equipotential lines in the semiconductor with an external magnetic field (after Tumanski, 2001).

The second effect is caused by the bending of electron energy bands at the Fermi surface in paramagnetic and diamagnetic materials. The bending influences the electrical resistance also and is proportional to $|B|^2$.

The last contribution is associated with ferro- and ferrimagnetic thin films. Since this effect is the leading contribution in anisotropic magnetoresistive sensors it will be discussed more in-depth.

In ferro- and ferrimagnetic material the conducting electrons from the band with uncompensated spins are anisotropically scattered. This fact is what makes materials ferro- or ferrimagnetic in the first place. The anisotropic scattering causes effects in the electrical resistance of the material which depend on the three dimensional shape of the Fermi surface. This shape is still being studied and only well known for a limited amount of magnetic materials. The magnetoresistive effect of a material therefore is based on empirical data. Theory only succeeds in approximations of the effect up to one order of magnitude (see Boll and Overschott, 1989).

The AMR effect can be described as a two dimensional problem if a thin film, single magnetic domain AMR element with length l , width w and thickness t is assumed. An outside field (\vec{B}) pushes the magnetization of the element \vec{M} out of the 'easy' axis (see figure 3.2). The easy axis lies parallel to the direction of the spontaneous magnetization (\vec{M}_s) of the element. This change in direction can thus be used to obtain information on the outside field.

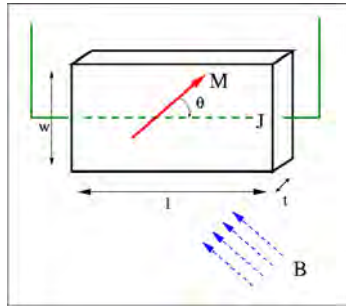


Figure 3.2: Geometry of an AMR sensor's principle axis and orientation. B is an outside magnetic field, pushing the magnetization M in an angle θ with respect to the flowing current J . Dimensions of the sensor itself are width (w), length (l) and thickness (t).

The angle θ is defined as the angle between the direction of the current \vec{J} running through the AMR element and the magnetization \vec{M} of the element. The resistivity ρ of the element depends on this angle. When $\rho \equiv \rho_{\parallel}$ for $\theta = 0^\circ$ and $\rho \equiv \rho_{\perp}$ for $\theta = 90^\circ$ the resistivity is given by:

$$\rho(\theta) = \rho_{\perp} + (\rho_{\parallel} - \rho_{\perp}) \cos^2 \theta = \rho_{\perp} + \Delta\rho \cdot \cos^2 \theta. \quad (3.1)$$

The magnetoresistive effect is then defined as the ratio $\frac{\Delta\rho}{\rho_{\perp}}$. Rewriting equation

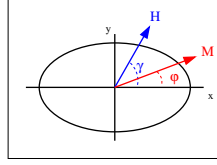


Figure 3.3: Stoner Wohlfahrt model of an ellipsoid single domain AMR element. The easy axis is aligned with the x-axis of the ellipsoid, the hard axis with the y-axis.

3.1 in terms of the resistance (R) of the sensor instead of the resistivity of each element, the dimensions of the sensor have to be inserted:

$$R(\theta) = \rho_{\perp} \frac{l}{w \cdot t} + \Delta\rho \frac{l}{w \cdot l} \cdot \cos^2 \theta \quad (3.2)$$

With equation 3.2 the relation between the magnetization M and the resistance of the AMR element is given. For the relation between M and the outside field H another model needs to be introduced. The Stoner Wohlfahrt model (see Stoner and Wohlfahrt, 1991) describes an ellipsoid single domain element (see figure 3.3). The energy (E_T) associated with such a domain boundary, subject to an external magnetic field (H), is given by:

$$E_T = E_k + E_H + E_d \quad (3.3)$$

where E_k describes the magnetic anisotropy energy due to the crystal orientation ($E = K \sin^2 \theta$, with K the anisotropy constant, a material constant). The energy from the external field H is depicted as $E_H = -HM_s \cos(\phi - \theta)$, ϕ being the angle of the external field relative to the easy axis. Finally the factor $E_d = NH_d \sin \theta$ is known as the demagnetization energy, the demagnetization field (H_d) is generated by the magnetization M in the element itself. The demagnetization field is a fraction of the actual magnetization and is described as: $H_d = NM$, with N a demagnetization factor depending on the shape of the domain. The demagnetization factor can only be calculated for ellipsoid elements.

The angle θ is the angle with the minimum energy, which can be found by taking the derivative of equation 3.3 and setting it to zero:

$$\begin{aligned} \frac{\partial E_T}{\partial \theta} &= KM_s \cos \theta \sin \theta - H_a M_s \sin(\phi - \theta) - H_s M_s \cos \theta \\ &= H_k \cos \theta \sin \theta - H_a \sin(\phi - \theta) - H_s \cos \theta = 0 \end{aligned} \quad (3.4)$$

If the outside magnetic field (H_a) is acting in direction perpendicular to the easy axis (i.e. the hard axis), the angle $\phi = 90^\circ$ and the angle θ can be written as (assuming $\cos \theta \neq 0$):

$$\sin \theta = \frac{H_a + H_d}{H_k} \quad (3.5)$$

If equation 3.5 is inserted in equation 3.2 a first order dependency of the resistance of an AMR element on the external magnetic field is found. The combination of both models used to obtain this relation agrees well with measurements and is therefore often used to describe the AMR effect. The ratio $\frac{\Delta\rho}{\rho_{\perp}}$ for the materials used in AMR sensors is usually in the 2 to 4 % range.

3.2.2 AMR Sensor Layout

Typically AMR sensors consist of thin films of material with high electrical conductivity (aluminum, gold, silver or copper) interbedded in films of AMR material (usually Nickel Cobalt alloys, also known as Permalloy). In the sensor models described here this material is slanted by an angle of about 45 degrees creating a so-called barberpole¹ layout. The sensor itself consists of four components in a resistive bridge configuration (see figure 3.4). The compensation and set/reset straps shown in figure 3.4 are used to reset the magnetization of the sensor into the easy axis, after being pushed into the direction of uniaxial anisotropy by the outside magnetic field. Thus preparing the sensor for another measurement.

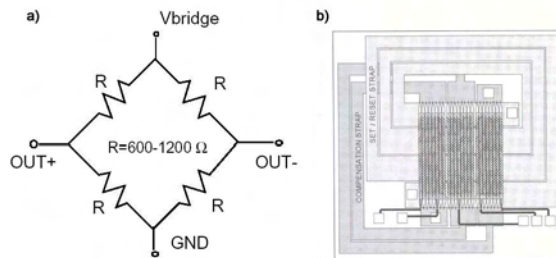


Figure 3.4: AMR sensor layout, a) shows the resistive bridge used in the AMR sensors (after Pant and Caruso, -), and b) the actual layout of the sensor itself (after Tumanski, 2001)

3.2.3 Magnetic Sensor Noise Spectra

As mentioned before, one of the main requirements of the system is to be able to obtain accurate measurements in the magnetic noise of a typical laboratory environment without the use of extensive magnetic shielding. Since the thermal noise of AMR sensors is small enough to be used in this kind of noise environment, several types of AMR sensors and one GMR were tested. Each sensor was supplied with a bridge voltage of 5 V and had a thermal noise level better than $100 \frac{pT}{\sqrt{Hz}}$ (see table 3.1).

In a shielded environment the noise spectra of these sensors were measured (see figure 3.5), in order to study their behaviour more in depth. The noise spectrum of a typical sensor incorporates two effects, at first the so-called $\frac{1}{f}$ behaviour

¹After the rotating signs used by barbershops

sensor type	thermal noise $\frac{pT}{\sqrt{Hz}}$	type	manufacturer
AA002	46	GMR	NVE
KMZ51	89	AMR	Philips
HMC1023	85	AMR	Honeywell
HMC1001	23	AMR	Honeywell

Table 3.1: Thermal noise level of investigated magnetoresistive sensors (manufacturer data)

(where f is frequency) which at higher frequencies will be substituted for a second behaviour, the sensor's thermal noise level.

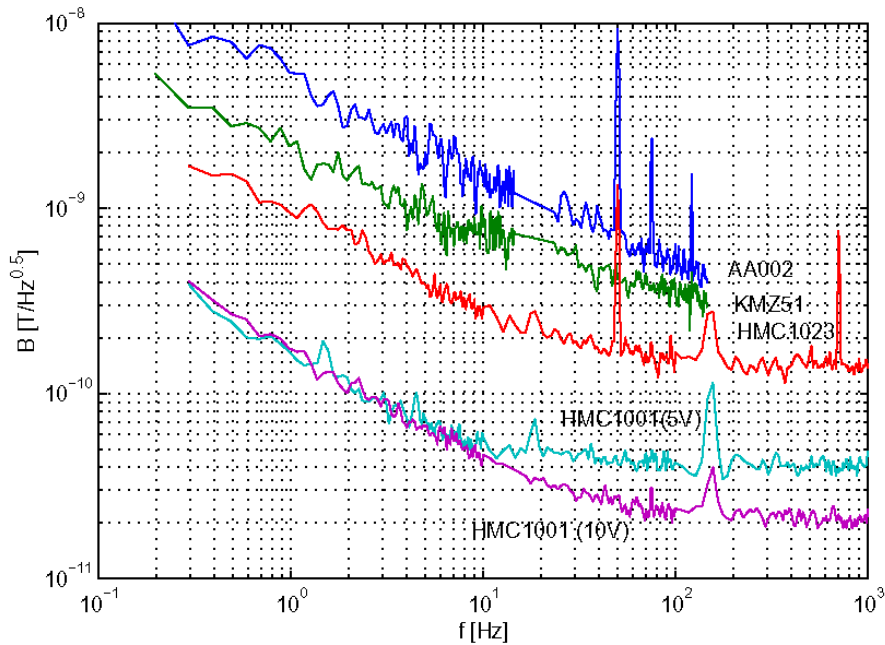


Figure 3.5: Noise spectra of different magnetoresistive sensors, after Zimmermann et al., 2001

From these noise spectra the superior noise behaviour of the Honeywell HMC1001 AMR sensor can be observed, leading to a noise level of lower than $50 \frac{pT}{\sqrt{Hz}}$ in the 10-100 Hz frequency range.

In addition, the noise spectrum of the HMC1001 sensor for the measured frequency range, shows not only the typical low frequency $\frac{1}{f}$ behavior, but also thermal noise behavior (the flattening out of the noise spectrum). This implies that when the sensor is operated with a higher bridge voltage of 10 V the thermal noise level can be reduced even more. Since the noise spectra of the other sensors did not show this behaviour in the studied frequency range, operation of the sensor with a higher bridge voltage could not reduce the thermal noise level.

The HMC1001 sensor is also available as a two directional sensor (HMC1002), which means that in order to measure the three components of the magnetic field, at least 2 sensor chips are needed (HMC1001 and HMC1002). The HMC1002 has the same specifications as the HMC1001, and is constructed in such a way that the two magnetic axis are perpendicular to each other.

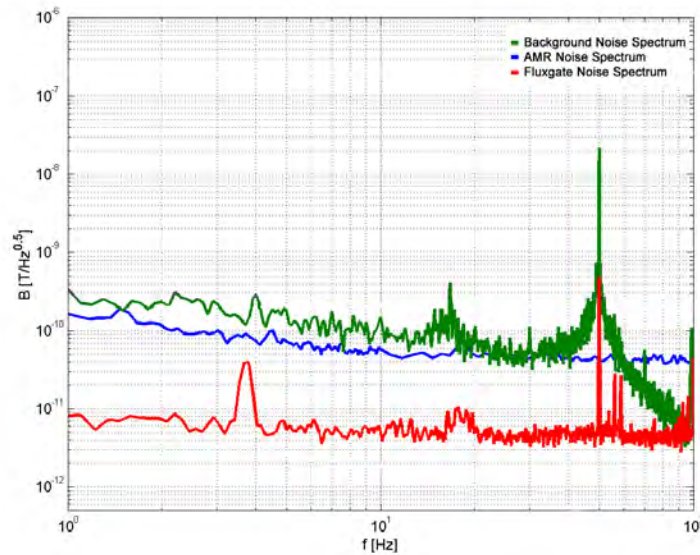


Figure 3.6: Noise spectra of typical laboratory (green) noise compared to the sensor noise of an AMR sensor (blue) and a fluxgate sensor (red) as reference.

Comparing the noise spectrum of the chosen sensor with the noise spectrum of our laboratory (see figure 3.6) the application of this sensor can be justified. In the complete measured frequency range the sensor noise lies below the environmental noise. As a reference the noise spectrum of a Bartington Fluxgate magnetometer (*Mag-03MSES*) is also presented, measured under equal conditions as the AMR sensor. Clearly present in the magnetic noise is the 50 Hz peak due to electrical appliances. The superior noise behaviour of the fluxgate sensor does not bring any improvement when compared to the typical laboratory noise.

3.3 Magnetic Sensor Modules

With the choice of sensors fixed, the other electronic components of the sensor module will be discussed. In order to increase the signal to noise ratio several techniques were implemented, i.e. a lock-in system was introduced, and an integration time was chosen. Also a field-feedback system was used to decrease the effect of the sensor sensitivity to the Earth's magnetic field. The whole module design is optimised such as to minimize magnetic field produced by the measurement modules themselves during a measurement.

3.3.1 Sensor Stability

The magnetic field of the Earth (with an intensity of about 50.000 nT) has a large negative effect on any magnetic field measurement system. The presence and direction of this field influences the sensitivity of the sensors and also the direction of the magnetic axis of each sensor.

The sensitivity of a complete single sensor AMR bridge consisting of four bar-berpole elements (see Ripka, 2001) can be defined as the variation of its bridge voltage with respect to the applied magnetic field. The full bridge voltage (U_s) of this circuit as a function of the sensors sensitive magnetic axis (H_{sen}) and of its orthogonal (H_{ort}) axis can be written as (Boll and Overschott, 1989):

$$U_s = U_0 \frac{cH_{sen}}{H_0 + H_{ort}} \sqrt{1 - \left(\frac{H_{sen}}{H_0 + H_{ort}}\right)^2} \quad (3.6)$$

The constant H_0 describes the characteristic field strength of the sensor (see Pant and Caruso, -), c the AMR sensor's magnetoresistive effect ($\frac{\Delta\rho}{\rho}$) and U_0 the supply voltage of the bridge.

Due to the orientation of the sensor, the second orthogonal axis of the sensor (normal to the sensor surface) can be negated and is therefore not taken into account. If small changes in the external fields are assumed, the sensitivity can be described by (Zimmermann et al., 2005):

$$S_{ort} \equiv \frac{dU_s}{dH_{ort}} = -\frac{U_0 c H_{sen}}{(H_0 + H_{ort})^2} \sqrt{1 - \left(\frac{H_{sen}}{H_0 + H_{ort}}\right)^2} + \frac{U_0 c H_{sen}^3}{(H_0 + H_{ort})^4} / \sqrt{1 - \left(\frac{H_{sen}}{H_0 + H_{ort}}\right)^2} \quad (3.7)$$

$$S_{sen} \equiv \frac{dU_s}{dH_{sen}} = \frac{U_0 c}{H_0 + H_{ort}} \sqrt{1 - \left(\frac{H_{sen}}{H_0 + H_{ort}}\right)^2} - \frac{U_0 c H_{sen}^2}{(H_0 + H_{ort})^3} / \sqrt{1 - \left(\frac{H_{sen}}{H_0 + H_{ort}}\right)^2} \quad (3.8)$$

Where $S_{ort, sen}$ is the sensor sensitivity in orthogonal and sensitive direction respectively. The relative sensitivities ($\frac{S_{ort, sen}}{S_0}$) can then be calculated for static fields in the order of magnitude similar to the Earth's magnetic field ($50 \mu T$). Where $S_0 = \frac{U_0 c}{H_0}$ describes the sensitivity in the direction of the sensitive axis without any external magnetic field ($H_{ort} = H_{sen} = 0$).

The sensitivity of the sensors can also be measured by using a triaxial Helmholtz coil. Inside this large coil (where small magnetic fields can be generated with an accuracy of about 0.1%) a second triaxial coil is located to generate the static field. This whole system (see figure 3.7) was located in a magnetically shielded area in order to negate the effect of the Earth's magnetic field. In order to test the compensation of the sensitivity dependence with the so-called flipping technique (see Ripka, 2001) both positive and negative layer magnetization of the sensor were measured (i.e. $\pm H_0$).

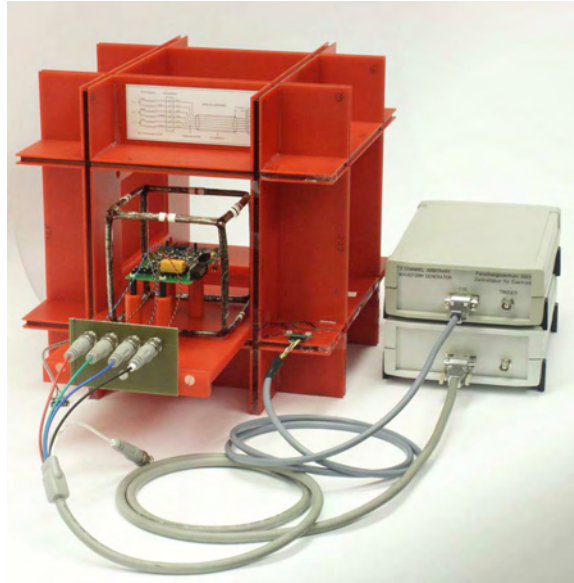


Figure 3.7: Measurement setup for sensor sensitivity determination, after Zimmermann et al., 2005

Table 3.2 shows the measured sensor sensitivities in orthogonal and sensitive directions ($S_{(ort,sen)m}$) and the calculated relative sensitivity values $S_{(ort,sen)c}$ for the sensitive and orthogonal axes. Both datasets show errors due to changes in sensitivity of up to 7%, influencing the measurements considerably. Compensation of this error by means of introducing the flipping-technique does not hold for the MERIT system, in several cases the sum of both magnetizations do not give rise to a zero mean value. Therefore in order to compensate for this static field dependency a field-feedback system is used.

In a field feedback system (see figure 3.8) a compensating coil is used to negate the static field in the sensitive direction, this causes S_{ort} to be zero at any time (see equation 3.7). The output signal in a field feedback system is only depending on the feedback coil sensitivity and no longer on the sensor sensitivity. Therefore the static fields have no effect anymore on the sensor sensitivity. The feedback system is incorporated in the sensor chip itself.

H_0 [$\frac{A}{m}$]	H_{ort} [$\frac{A}{m}$]	H_{sen} [$\frac{A}{m}$]	H_{ort} [$\frac{A}{m}$]	$\frac{S_{ortc}}{S_0}$ -	$\frac{S_{ortm}}{S_0}$ -	$\frac{S_{senc}}{S_0}$ -	$\frac{S_{senm}}{S_0}$ -
636.6	0.0	0.0	0.0	0.0000	0.0000	1.0000	1.000
-636.6	0.0	0.0	0.0	0.0000	-0.0000	1.0000	0.9999
636.6	39.8	0.0	0.0	0.0000	-0.0041	0.9412	0.9337
-636.6	39.8	0.0	0.0	0.0000	0.0049	1.0667	1.0749
636.6	0.0	39.8	0.0	-0.0621	-0.0711	0.9941	0.9982
-636.6	0.0	39.8	0.0	0.0621	0.0711	0.9941	0.9938
636.6	0.0	0.0	39.8	0.0000	0.0017	1.0000	0.9991
-636.6	0.0	0.0	39.8	0.0000	-0.0017	1.0000	0.9998

Table 3.2: Static field sensor sensitivity, $S_{(ort,sen)c}$ denote calculated values, $S_{(ort,sen)m}$ measured values, after Zimmermann et al., 2005

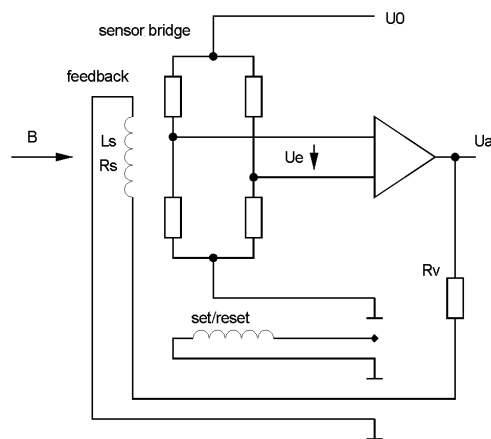


Figure 3.8: Field feedback circuit with compensating coil, after Zimmermann et al., 2005

Since the sensitivity no longer depends on the sensor sensitivity itself, the temperature drift of the coil (R_s) and resistor (R_v) can give rise to errors. This effect is limited to about 0.1% for temperature changes of 5 K, and can therefore, in a laboratory situation, be neglected. A second temperature related effect is the heating of the circuits themselves. The HMC1001 requires compensation currents as high as 25 mA, which leads to errors due to self-heating of 0.14%. A good thermal coupling with the circuit board to dissipate the produced heat and the use of two parallel SMD resistors limits the self-heating and allows to neglect this error also.

3.3.2 Lock-in Amplification

Introduction of a lock-in system increases the signal to noise ratio considerably, and allows the measurement of small amplitude periodical signals in a environment with a high noise level. The lock-in technique is based on the mathematical principle that two sine or cosine functions multiplied with each other only give rise to a non-zero value if both frequencies are the same. A reference signal $r(t)$ is therefore generated and multiplied with the measurement signal $u_m(t)$, see figure 3.9. A first-order moving average filter (with an integration time T) acts as a lowpass filter and gives rise to the output signal u_{out} :

$$u_{out} = \frac{1}{T} \int_0^T u_m(t)r(t)dt \quad (3.9)$$

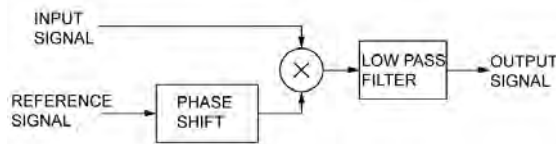


Figure 3.9: Schematic signal processing of a lock-in amplifier, after Zimmermann et al., 2005.

The effect of introducing the lock-in technique to the system, and the influence of the integration time can be seen in figure 3.10. Simulations of three different integration times were compared, first with an integration time of 0.5 s, secondly 3 s and finally a 10 s measurement cycle. Since one requirement of the system is to operate with an accuracy of 50 pT, the 10 s integration time is chosen. Using this integration time only a few noise peaks are above the 50 pT. The 50 pT was set as upper noise limit in order to be able to measure the relative small magnetic signal.

Studying the final noise spectrum (see figure 3.10 c) two distinct frequency ranges appear as good candidates to provide the lock-in frequency: 20-40 Hz and 60-80 Hz. Traditional MMR, the patent by Jakosky for instance, is limited to frequencies below 100 Hz (see Jakosky, 1933), which imply that both frequency ranges are acceptable. But since the MMR system, as used in this

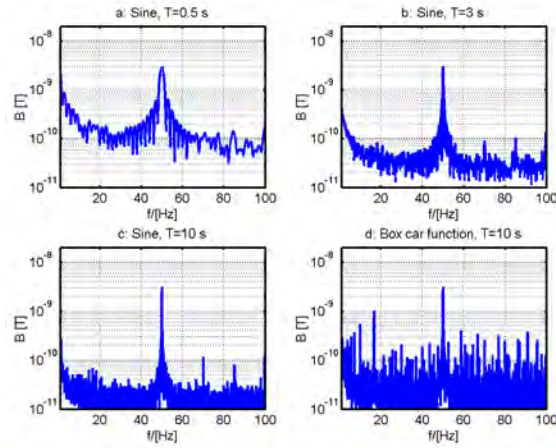


Figure 3.10: Lock-in signal frequency spectra, a) denotes a sine function with an integration time of 0.5 s, b) an integration time of 3 s, c) of 10 s. In figure d) a boxcar function as reference signal is used with an integration time of 10 s, after Zimmermann et al., 2005.

application, is developed as an addition to traditional DC-resistivity, the lower frequency range was chosen. This also limits any possible unwanted induction effects associated with alternating currents. The chosen range is on the low side limited by the typical $\frac{1}{f}$ noise, and on the high side by the 50 Hz peak due to electrical appliances. Therefore a 25 Hz signal as lock-in reference signal was chosen.

An alternative option to a sine function as reference signal is a boxcar function. The effect of this type of signal was also tested with an integration time of 10 s. The overall noise level of the box car function (see 3.10 d) is much higher than that of the sine function with the same integration time, leading to the choice of a sine function reference signal.

3.3.3 Displacement Currents

A short note needs to be made here concerning the fact that no real direct current signal is used in the MERIT system, although the data is treated as traditional DC resistivity data. The use of an alternating current as injection current could give rise to unwanted effects due to displacement currents. This subsection will show the behaviour of the injected AC current as DC phenomenon instead of AC (wave) phenomenon.

For a periodical signal the magnetic field strength (\vec{H}) due to a current (\vec{J}_f) in matter can be written as:

$$\begin{aligned}\nabla \times \vec{H} &= \vec{J}_f + \vec{J}_d \\ &= \sigma \vec{E} + \frac{\partial \vec{D}}{\partial t}\end{aligned}\quad (3.10)$$

Where the displacement current is denoted by \vec{J}_d and \vec{D} the electric displace-

ment. The ratio between \vec{J}_f and \vec{J}_d leads to information on the nature of the electrical phenomenon, for DC resistivity surveys \vec{J}_f is dominant, for the wave behaviour of electromagnetic phenomenon \vec{J}_d also plays an important part (see e.g. Miltzer and Weber, 1985). The displacement current can be written for a periodical signal ($e^{i\omega t}$) as:

$$\vec{J}_d = \frac{\partial \vec{D}}{\partial t} = i\varepsilon\omega \vec{E} \quad (3.11)$$

where ε describes the permittivity of the medium ($\varepsilon = \varepsilon_0\varepsilon_r$ with ε_0 the permittivity of free space and ε_r the relative permittivity), and ω the frequency. Since the current in the sample (\vec{J}_f) is given by:

$$\vec{J}_f = \sigma \vec{E} \quad (3.12)$$

Both current densities can be compared by building their ratio:

$$f = \frac{|\vec{J}_f|}{|\vec{J}_d|} = \frac{\sigma}{\varepsilon\omega} \quad (3.13)$$

For a small frequency ω , the value of f is very large, and allows to neglect the influence of \vec{J}_d with respect to \vec{J}_f . With the chosen frequency of 25 Hz, and assuming a typical value for the electrical conductivity and the permittivity of soils (ranging from 0.01 to 1 $\frac{S}{m}$ for σ and around 9×10^{-12} for ε in non magnetic soils, see e.g. Telford et al., 1990), this criterion is met and allows us to neglect any effects associated with displacement currents.

3.4 Electrical Potential Measurements

A desktop computer is used to control the electrical potential measurements in addition to the current injections. In the measurement setup 16 relays are incorporated, allowing a maximum of 16 electrodes to be switched. The electrical potential differences are also measured with lock-in technique, as is the injection current. The current setup uses two reference signals, a sine and a cosine wave (both with 25 Hz frequency) as part of a future development in which not only the amplitude of the signal, but also the phase can be taken into account. This way a future MERIT system could be able to combine other geophysical methods (i.e. spectral induced polarization (SIP) and magnetic induced polarization (MIP)).

In conjunction with the measurement of the electrical potential due to the current injection, the injected current itself is also measured during the whole measurement and returned to the computer for further processing. Measurement of the input current is necessary to monitor the development of the contact resistance, which can vary during a single measurement due to corrosion effects at the electrodes for instance. Also typical hydrological scenarios (e.g. drying of a sample during irrigation experiments) have a profound effect on the contact resistance of an electrode, and thus the injected current.

3.5 The Lab-scale MERIT Measurement Setup

The current MERIT system is designed to be implemented in laboratory scale hydro-geological experiments (see for instance Tillmann et al., 2004 and Verweerd et al., 2004). A typical size of laboratory samples in flow and transport experiments are columns of several cm radius and a height of several tens of cm. The measurement setup is therefore constructed to accommodate cylindrical objects with a radius of 10 cm and up to 50 cm height. In order to monitor flow and transport on this scale a relatively fast scanning system is required. For this system a plexiglas torus containing 24 measurement modules was constructed. The torus can freely move in vertical direction by means of a vertically moving belt (with a positioning accuracy of $50 \mu m$) limiting the spatial sampling only in the horizontal plane.

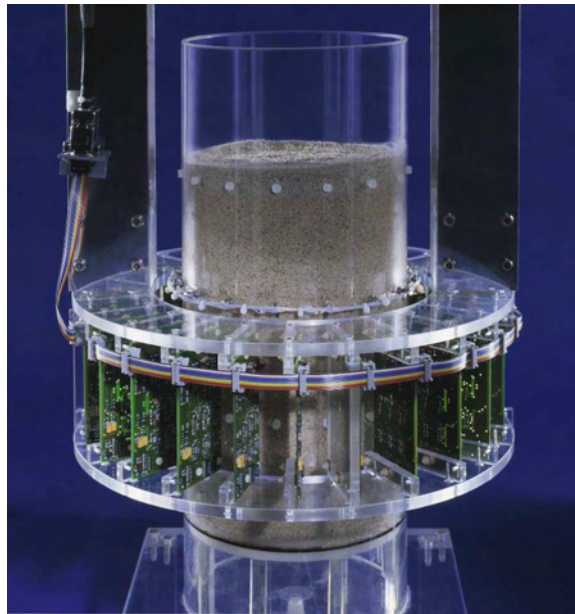


Figure 3.11: The MERIT scanning system, close up of scanning torus with magnetic field measurement modules, after Zimmermann et al., 2005

The electrodes used for the ERT part of the system are located in the plexiglas casing of the (soil-) sample itself and at three different heights. This way three rings each with 5 evenly spaced electrodes are constructed. The 15 electrodes themselves are stainless steel screws (size M4), with a length of 4 mm on the inside of the column.

The magnetic field dataset is sent to the PC via a BUS after each measurement cycle. During the measurements all data processing and storage is done on the microchip located on the module, this limits additional magnetic noise due to currents used in communication between each module and the PC.

Movement of the scanning torus, as well as the ERT data acquisition and cur-

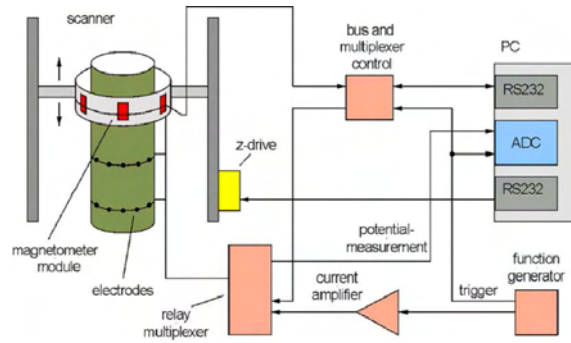


Figure 3.12: Block diagram of the MERIT scanning system, after Zimmermann et al., 2005.

rent injection is controlled by a measurement PC. Close to the PC the current generator, current amplifier and relays for switching electrodes on or off are located. A twisted cable, of about 1.5 m length, runs between the relay board and the soil column in order to limit the magnetic field due to the injection current flowing in this cable. At the base of the column the cable is divided into 15 smaller cables and connected to the electrodes (where shielding through twisting is no longer possible).

Chapter 4

Testing the Measurement System

Before the system, as described in the previous chapter, is used for actual measurements of the conductivity distribution in cylindrical probes several tests were undertaken to study the behaviour of the whole measurement system in terms of measurement accuracy and repeatability.

To test the measurement system a reference magnetic field was used. In order to have a good reference a small coil was constructed with well known properties, the magnetic field generated by this coil was then measured and modelled (see Zimmermann et al., 2005). In addition to the tests noise measurements were carried out, to study possible disturbances in the vicinity of the measurement system or construction errors in the modules.

4.1 Sensor Output Definitions

Since the sensors used in the MERIT system are placed in radial direction on the scanning torus (see figure 3.11), each sensor in the horizontal plane has a different orientation (for module i , \vec{x}_i and \vec{y}_i). Both sensors horizontally mounted on the module measure components of both x and y components of the magnetic field (see figure 4.1), the so-called module coordinate system. A transformation is therefore needed, in which the measurements of each module is transformed into the global coordinate system $\vec{X}, \vec{Y}, \vec{Z}$. The z-component of both coordinate systems is similar and does not change during transformation. The sensitive axis of each sensor therefore measures a magnetic field composed of all three components of the global field. If the contribution due to orthogonal sensitivity is assumed zero, S_{sen} can be written as a function of the contributions due to the three components ($S_{sen} = f(S_X, S_Y, S_Z)$) and the total output of the i^{th} sensor u_m can be written as:

$$u_m(i) = \left(S_X, S_Y, S_Z \right)_i \begin{pmatrix} B_x \\ B_y \\ B_z \end{pmatrix}. \quad (4.1)$$

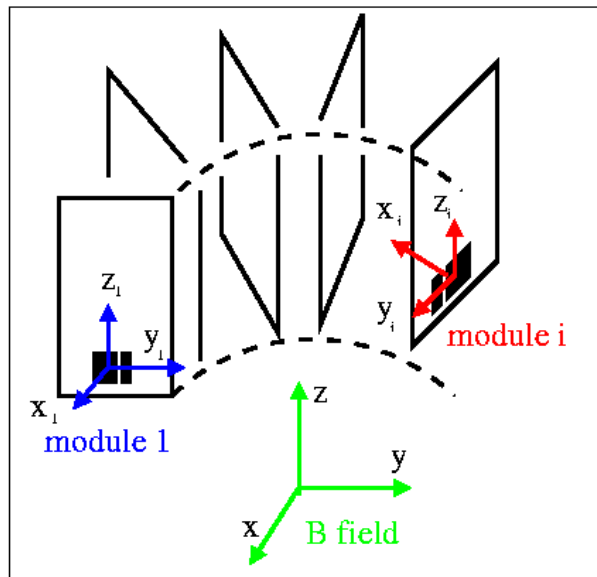


Figure 4.1: Sensor coordinate systems, each module i has its local coordinate system (x_i, y_i, z_i) with respect to a global coordinate system \vec{X} , \vec{Y} and \vec{Z} .

Another aspect is the locations of the sensitive axes of the sensors themselves. As a first order approximation one can assume the axes to be orthogonal and oriented along the module coordinate system. Using the data obtained in the measurement of the sensitivity a more accurate approximation can be made on the location of the sensor sensitive axis, although only in the case of homogeneous fields.

This fact makes it practically impossible for inhomogeneous fields to represent the measured data as magnetic fields. All measured magnetic data will therefore be presented in sensor output value, instead of magnetic field strength. By using equation 4.1 one can obtain relevant output sensor value for every calculated magnetic field under the assumption of homogeneous outside magnetic fields (the sensitivities for homogeneous fields can be obtained as described in the previous chapter).

4.2 Magnetic Noise Sources

Even with the addition of the lock-in technique, the measurement of the magnetic field is still prone to disturbances by noise. First of all there are noise sources which produce magnetic noise at the lock-in frequency of 25 Hz, which will not be filtered out by the lock-in technique. Secondly the sensitivity of the sensors changes considerably in the presence of outside magnetic fields, thus making the measurements less accurate. In this section possible sources of magnetic noise will be described, both environmental and anthropogenic disturbances, which can influence the data quality of the MERIT system.

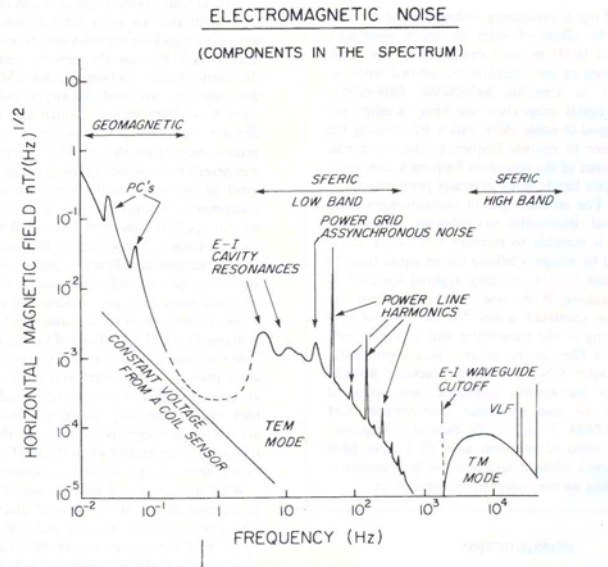


Figure 4.2: Schematic overview of the electromagnetic noise spectrum, noise is both of environmental and anthropological origin (after Macnae et al., 1984).

4.2.1 Environmental Disturbances

Natural magnetic fields in the extremely low frequency (ELF) range are well documented (see, Barr et al., 2000). Most of these fields are either related to volcanic eruptions, dust storms and tornadoes or lighting activity (i.e. Sprites or Schumann resonance, also known as E-I cavity resonance) but also solar or other astrophysical phenomena can occur in this frequency range. Since these effects cannot be predicted and the possibility of occurrence is not very large, these effect are not taken into account in the MERIT setup. A schematic noise spectrum with both environmental and anthropological noise sources can be seen in figure 4.2.

4.2.2 Anthropogenic Disturbances

The frequency used in the MERIT system is normally not disturbed by any effects due to human activity. The only known transmitter capable of transmitting at 25 Hz frequency is a Russian ELF communication system on the Kola Peninsula (see Barr et al., 2000). Other military systems are assumed to operate in the 70-80 Hz range as minimum. Radio amateurs are not known to operate in this frequency range due to the huge size of antennas necessary for transmission. The frequency of the current in the overhead contact line of trains used in much of north and middle Europe (Germany, Austria, Switzerland, Norway and Sweden) is 16.66 Hz and therefore also does not interfere.

4.2.3 Magnetic Noise Measurements

The offset and noise of the complete MERIT system (see chapter 3) can be determined by measurement of the magnetic field without any current injection

(see figure 4.3). This way all disturbances due to sensor modules and environment (i.e additional noise sources or changes in the direction of the sensitive axis due to for instance the Earth's field) can be determined. Since the three component sensors on the module are split up in a single directional sensor (HMC1001) and a two-directional sensor (HMC1002), this measurement also can give information on any errors in the orthogonality of the sensor located on the module. The measured magnetic fields were translated from the module coordinate system to the global Cartesian coordinates. The sensitive magnetic axes were supposed to be in the same coordinate system as the modules.

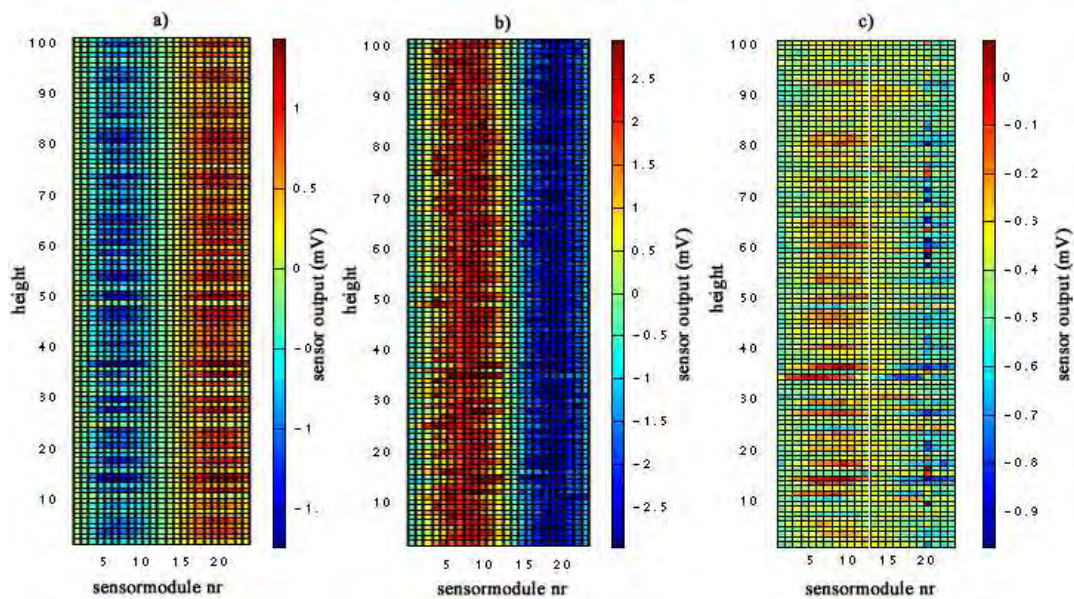


Figure 4.3: Sensor output values measured without a current injection, a),b) and c) show the global x,y and z component of the magnetic field ' '

The magnetic noise is presented in figure 4.3 as the output of the three magnetic field sensors transformed to the global coordinate system. Thus three planes are constructed, which can be seen as the x,y and z component of the magnetic field of a folded out cylinder mantle.

The mean values of the measured sensor output for the x,y and z-component are 0.05 mV, -0.1211 mV (without the two measurements with sensor output values over 20 mV) and -0.413 mV respectively (see also figure 4.4). A clear coherent noise signal is present in the x and y component (hence the non-Gaussian distribution of both histograms, in comparison to the typical Gaussian distribution of the noise in the z component). These signals can be related to the power supply for generation of the injection current. Due to the dimensions of the laboratory the distance between scanning system and current generation is about 1.5 m, tests have shown a distance of about 5 m to be sufficient to reduce this error below 0.1 % . Since this error is supposed to be stationary in time, it can easily be removed by subtracting this signal for the measurements.

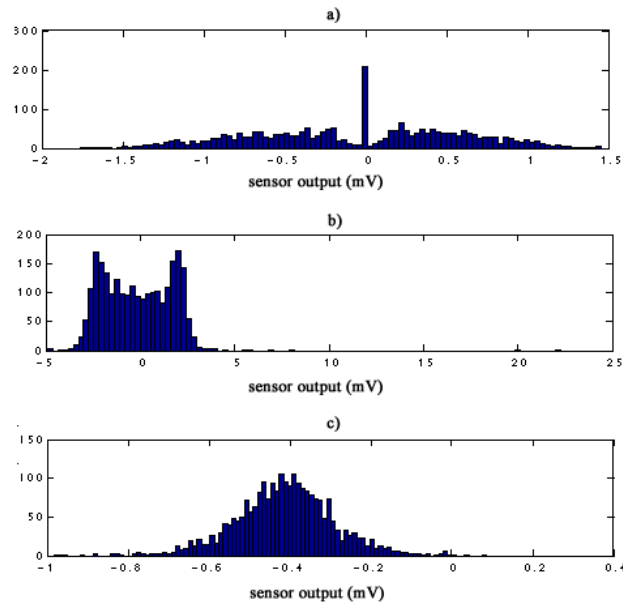


Figure 4.4: Histograms of the sensor output values without a current injection, a), b) and c) depict the global x,y and z components'

Also the effect of one improperly constructed module (visible as the vertical line with higher amplitude in the z-axis plot at module number 20) could be determined.

4.2.4 The Laboratory Background Noise

An overview of the ambient noise sources in the laboratory used was obtained by the measurement of a magnetic noise map of the room. Every 50 cm the magnetic field was measured with a three component fluxgate sensor (Bartington, *Mag-03* MSES) at floor level. These data were then low-pass filtered (40 Hz low pass filter) and a noise map was constructed (see figure 4.5)

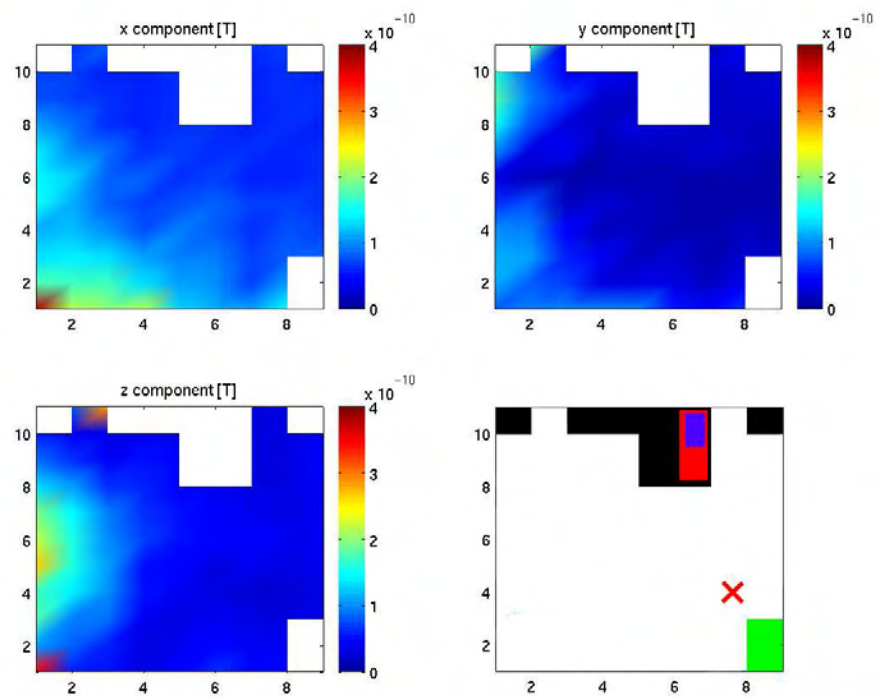


Figure 4.5: Magnetic noise map of the test laboratory, figure a) to c) show the x,y ,and z component of the 0-40 Hz frequency noise. figure d) shows the general layout of the laboratory, the black boxes are wardrobes, the red block is a sink (with the sink itself depicted in blue), and the green block is the plumbing connecting the climate control. The location of the MERIT scanning system is depicted by the red X.

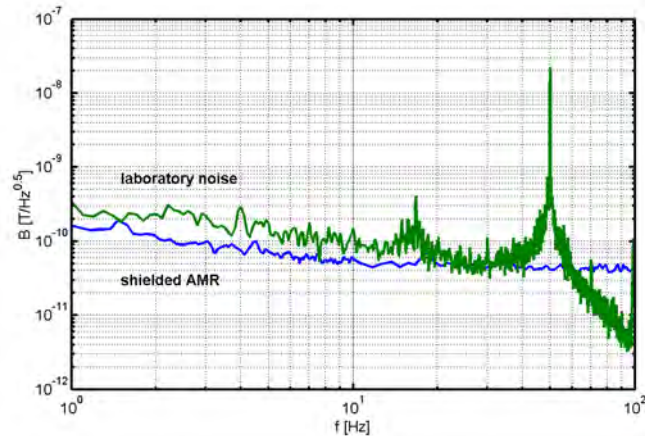


Figure 4.6: Magnetic noise spectrum of the test laboratory, in comparison to the thermal noise spectrum of a shielded AMR sensor.

Clearly the right side of the room can be classified as the quieter side (due to the fact that this was an outer wall no electrical cables were found in this wall). The scanning system was therefore placed in this area, not far from the climate control plumbing. Figure 4.6 shows a complete (total) noise spectrum up to 100 Hz at the approximate location of the scanning system. As a reference the thermal noise spectrum of the used AMR sensor is also shown, which clearly is lower than the ambient noise in that area.

4.3 The Magnetic Field Due to a Reference Coil

The magnetic field due to a coil can easily be calculated when the position of the coil with respect to the positions of the magnetic field sensors is known. Therefore a small coil was used to test the accuracy of the system in terms of difference between a measured data set and a modelled data set. The coil was placed inside the scanning torus of the MERIT setup and a 25 Hz current was applied to the coil. For this test, just as in the case of real measurements, the sensor voltage was measured and modelled. In order to obtain the sensor voltage from the calculated magnetic field equation 4.1 is used. The sensitivities of each sensor are determined in a similar way as described in the previous chapter, which is a sufficiently accurate description for the rather simple magnetic field of a coil. The calculated data was then translated to the local module coordinate system to observe the behaviour of each sensor more accurately. Both measured (U_{mx}, U_{my}, U_{mz}) and calculated (U_{tx}, U_{ty}, U_{tz}) sensor voltages, which are proportional to the measured magnetic field, were subtracted from each other.

The maximal errors relative to the maximal values of all sensor voltages are 0.6%, 0.5%, 1% for the x-, y-, and z-sensor. The RMS errors are 0.20%, 0.18%, 0.53%. Probably the errors are caused by magnetic distortions due to induced eddy currents in metallic objects in the surroundings and not by calibration

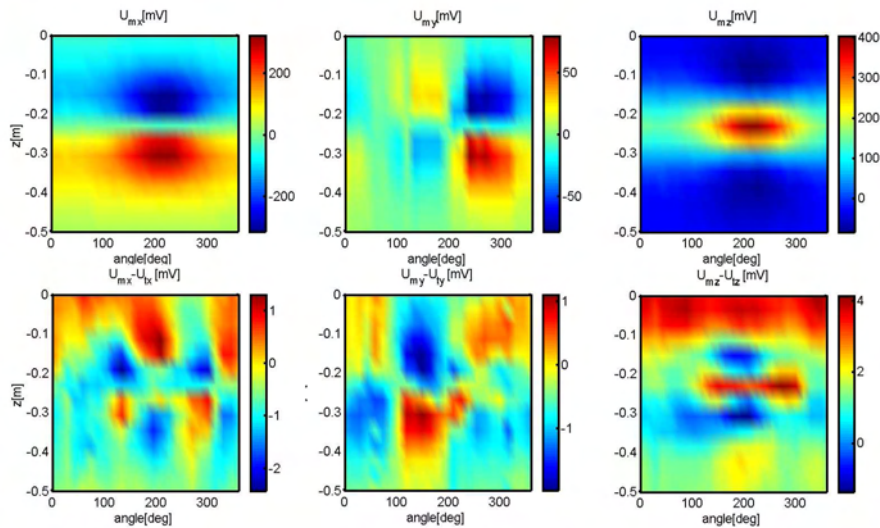


Figure 4.7: Sensor output due to the magnetic field of a coil, a) shows the measured sensor output values (representing the x, y and z components of the magnetic field respectively). Figure b) shows the differences between the measured and calculated magnetic fields (again split up in x, y and z components). All data is presented in the global coordinate system (after Zimmermann et al., 2003).

errors. Comparisons between a traditional three-component fluxgate sensor (a Bartington *Mag-03* MSES) and the designed sensor modules show similar behavior when compared to calculated magnetic field values in a laboratory noise environment.

4.4 Repeatability of a Measured Dataset

The repeatability of a measurement system is also an important factor in obtaining a quantitative measure for the data quality. In order to test the repeatability, the magnetic field due to a coil was measured and the measurement was repeated eight times. With use of the eight datasets the standard deviation of the measurement sets was calculated. In order to obtain the correct dimensions of the error with respect to a measurement the variance is depicted as percentage of the absolute mean value at that location.

In order to characterise the repeatability of the measurements not all measured data was used. Very small sensor outputs were not taken into account, due to the fact that the effect of a disturbance on these very small values is much greater (i.e. the percentile value) than on a measurement with an actual signal (the magnetic field due to the coil instead of noise). A threshold was therefore used to separate the low signal from the large signal subset. In this case 10 % of the mean maximum sensor output value (of the complete dataset of each component) was chosen as threshold between large and small data values. The

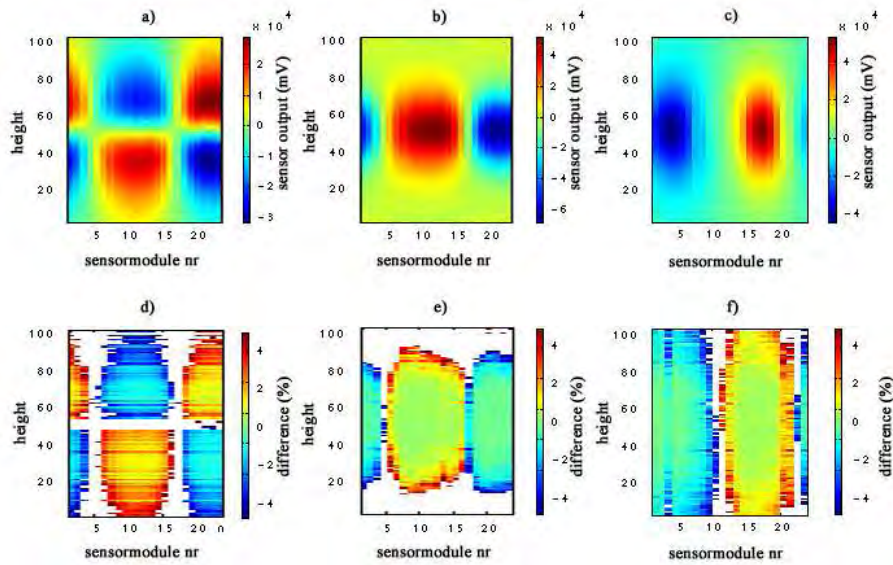


Figure 4.8: Repeatability of the measurements, figures a),b) and c) depict the mean measured magnetic field by the three sensors in mV, figures d),e) and f) the standard deviations as percentages of the mean maximum values after a threshold has been implemented to divide between large and small signals.

white pixels in figure 4.8 denote the left out values. In general the repeatability of the system is better than 1 %, for the x-sensor slightly larger (see figure 4.8).

4.5 The MERIT Measurement Scheme

Several aspects need to be taken into account when an actual measurement is taken, for instance the effect of wires and natural disturbances in the magnetic field. In this section the measurement scheme will be described and possible errors due to measurements will be discussed.

The current wire carries the injection current from power generator to the soil column. Since this current, and its associated magnetic field have the same frequency as the reference signal, it cannot be removed by using the lock-in technique. Therefore a different solution has to be found to negate the effect of the magnetical field due to the wires.

The effect of the current running through the wires in comparison to the current running to the sample can be modelled by application of the law of Biot-Savart (for the wire) and the numerical algorithm presented earlier. The current wire is twisted up to the point where it is connected to the first electrode to reduce the magnetic field due to the current in the wire. From C1 to C2 it is a single wire, in reality the twisting of the wire will give rise to an additional signal, since twisting the two wires will not be as perfect as in the modelled case (and a portion to the magnetic field will not be negated by twisting).

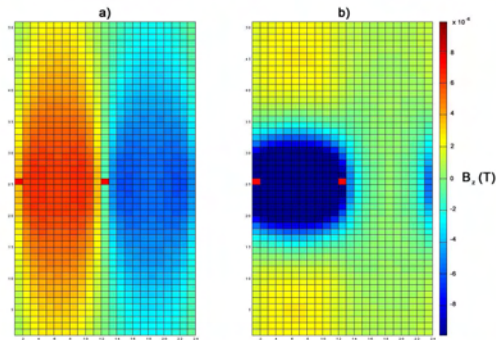


Figure 4.9: Effect of the magnetic field due to the injection current, a) z-component of the magnetic field of a horizontal current injection through a homogeneous column, b) z-component of the magnetic field due to the wires running between C_1 and C_2 (denoted as red pixels).

As can be seen in figure 4.9 the magnetic field due to the wires is almost an order of magnitude larger than the magnetic field due to the currents in the sample (see figure 4.9). This is a major problem in the field of MMR. Firstly it poses a source of errors (measurement of an unwanted field) and secondly, it could cause problems related to the dynamic range of the sensors, which is limited to about 200 nT (see chapter 3).

On the field-scale the solution is to place the wires in a horseshoe design (see figure 2.2), and measure the magnetic field far away from the wires (several 100 m or even km). Application of the law of Biot-Savart to calculate the magnetic field due to the wire, and subtraction of this magnetic field from the measured data set, reduces this error to a minimum. Since the system has a small laboratory scale setup, the physical consequences of this solution cannot be applied due to the dimensions of the room used. The modelling of the wires and subtraction of the wire effect (see Chen et al., 2002) itself also gives rise to problems in this setup. Again the size of the setup is the cause, the modelling the magnetic field due to a current wire requires only the implementation of the law of Biot-Savart. But for the current setup this requires the location of the wire has to be known at (sub-) mm scale which gives rise to practical problems, in mapping the location of the wire with (sub-) mm accuracy.

In the laboratory scale MERIT system a so-called 'difference measurement' scheme therefore is implemented, in which shortly after each other two measurements are conducted with only slight changes in the probe (i.e. water saturation or introduction of a single conductivity anomaly in a homogeneous column). In this way the effect of the wires can be canceled when both data sets are subtracted from each other and only the effect of the changed parameters remain. This can also be applied in the case of the monitoring of flow experiments, in which in two consecutive measurements only slight changes are visible, if the time between both measurements is small enough to negate other

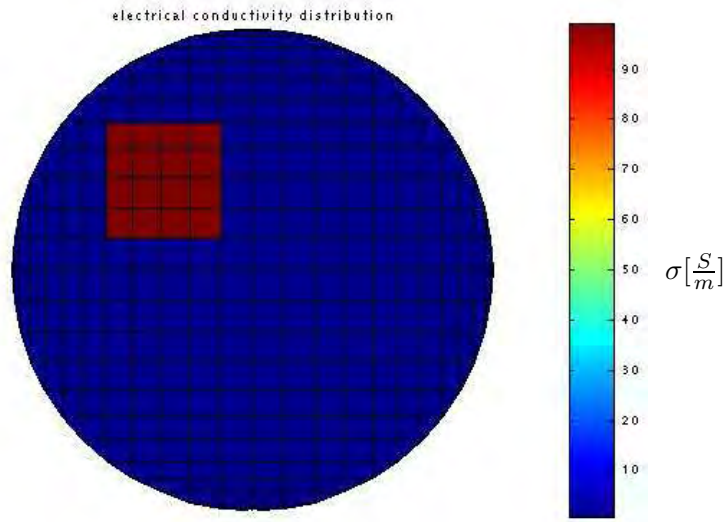


Figure 4.10: Electrical conductivity distribution of the rod model

changes in the system.

4.6 Numerical Magnetic Fields Compared to Real Data

Finally the developed magnetic field forward routine has to be tested against the real data acquired with the MERIT system and vice versa. In this comparison only the MMR component of the MERIT system will be taken into account. The effect of the current wire will be eliminated by the use of so-called difference measurements, which will also be modelled in order to obtain a clear comparison between modelling and measurements.

4.6.1 The Conductive Rod Modelled

To test the measurement signal of a typical 2D structure a rod was modelled with an electrical conductivity of 100 S/m located in a 0.01 S/m column (see figure 4.10). The vertical extensions of the rod are the same as the column itself. The three components of the magnetic field due to a homogeneous column and the model described above were modelled and the difference between both datasets was calculated (see figure 4.11).

As a current injection 100 mA was used in the large vertical dipole configuration (see chapter 5). The clear anomalies present in the difference image show the ability of the MMR data to obtain a response due to the conductive rod.

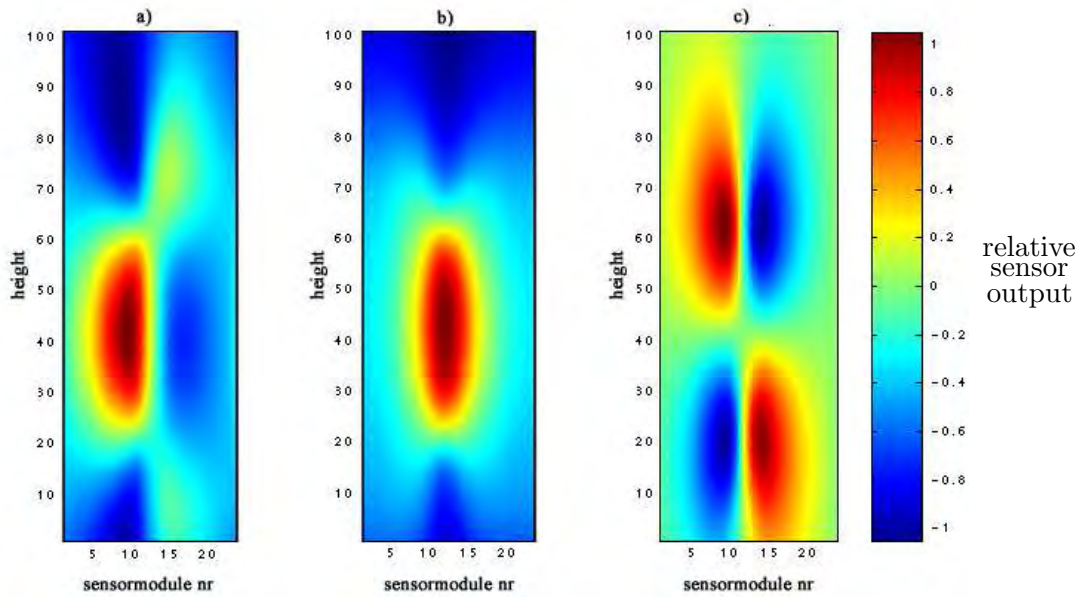


Figure 4.11: The modelled differences in the three components of the magnetic field due to the insertion of the rod (relative values)

4.6.2 The Conductive Rod Measured

A similar configuration was measured, in which an aluminum rod (2.5 cm radius) was placed in a saturated sand column (with an electrical conductivity of $0.013 \frac{S}{m}$). The measurement configuration used here was as similar as possible to the modelled case. In order to compare both results, the measured data was transformed as described in chapter 4. This way both datasets was transformed to the same orthogonal coordinate system as the modelled data.

In general the comparison between the modelled data (see figure 4.11) and measured data (see figure 4.12) fits very well, although the measured magnetic fields are still rather noisy, and show a stripey pattern especially the z component. Still several notes have to be made, first of all, the forward image was calculated without any knowledge on the location of the sensitive magnetic axes. Therefore the sensitive axes were taken as Cartesian coordinates directed along the sensor chips. Secondly the measured data are presented in mV sensor output, implying that the amplitude of both signals cannot be compared, only the shape of the anomalies is of relevance. The data is therefore presented as relative values, each component weighted by the maximum absolute value of each component. The two measured datasets used to build the difference image were weighted with the injected current used at each measurement. This is done to limit the effect of changes in the injection current due to changes in for instance the contact resistance of the electrode between measurements, or temperature effects on the electrical conductivity.

An additional note on the noise present in the measured data has to be made.

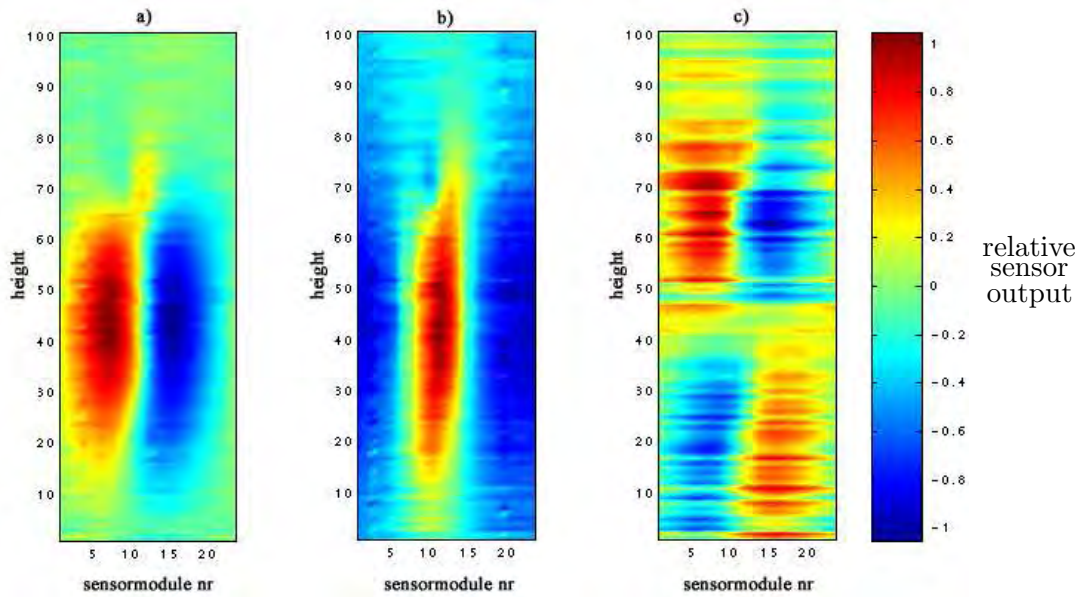


Figure 4.12: The difference measurements for all three magnetic components, due to the introduction of an aluminium rod (relative values)

Decrease of the noise present in measured data can be obtained by increasing the current strength used, in the current set up the maximum current strength lies between 12 and 13 mA, depending on the electrical conductivity of the medium. For normal ERT measurements this value is sufficient if the values for a field scale ERT survey are down-scaled to the column size. MMR measurements on the other hand can still benefit from larger current strengths by increase of the signal to noise ratio in comparison to ERT. The only limiting factor is the magnetic field due to the current in the injection wires, this is obviously limited to the dynamic range of the sensors. In addition more powerful microcontrollers will be able to measure at a higher sampling rate, therefore increase the signal to noise ratio by stacking more responses.

Chapter 5

Optimisation and Resolution of the MERIT System

The optimisation of a system in terms of measurement efficiency and speed is an important aspect of the design of any measurement system. The best choice for sensor location and, in the case of MERIT, current injection electrodes can lead to a better understanding of the studied volume and saves time, effort and money.

A useful tool in understanding the behaviour of a system of linear equations is the study of the so-called Jacobian, or sensitivity matrix of the system, by means of singular value decomposition (see Lanczos, 1961). In this chapter a detailed study of the Jacobian of several MERIT datasets will be shown, leading to conclusions about the most favourable measurement configurations in terms of amount of information contained in the data. Closely related to the determination of the amount of information obtainable in a measurement is the resolution of a dataset. Therefore the difference in resolution of ERT, pure MMR and MERIT datasets will be shown, proving the increase in resolution of a MERIT datasets when compared to either measurement technique as a stand alone.

5.1 Background Mathematics

The following section will deal with the background mathematics used to characterise the importance of different measurement locations. This information will then be used to select the current injection pattern containing the most information. Closely related to the mathematical technique used to distinguish between important and non-important data points is the determination of the resolution of the system.

At first the basics of singular value decomposition (SVD) will be laid down, since SVD is used as basis of both techniques. SVD will be implemented on the so-called Jacobian, or sensitivity matrix, which will lead to the desired characterisation of information and resolution. The second part of this section will

show the application of both techniques on the MERIT system, and conclusion on the (in terms of information density and resolution) most optimum measurement configuration. In addition comments on the inherent non-uniqueness of geophysical inversion and the increase in resolution obtained in MERIT measurements in comparison to ERT or MMR will be made.

5.1.1 Singular Value Decomposition

Solving a set of linear differential equations, will eventually lead to the task of obtaining an inverse of a typical matrix \mathbf{A} (with n rows and m columns). For ill-posed problems (where the rank of the matrix $\mathbf{A} < n$) difficulties occur due to singular behaviour (or behaviour very close to singularity) of the matrix. An important tool to understand this behaviour, for any given square matrix, is to obtain information on its eigenvalues. Unfortunately most matrices are non-square matrices, therefore the matrix has to be decomposed into its singular values, in order to understand its behaviour. Lanczos, 1961 described an effective way to decompose any non-square ($n \times m$) matrix into three different matrices. Two of these matrices are square orthonormal¹ matrices, the third one is a non square diagonal matrix. Starting with the non-square system of equations:

$$\begin{array}{ccc} \mathbf{A} & \vec{x} & = & \vec{y} \\ n \times m & m & & n \\ \text{matrix} & \text{rows} & & \text{rows} \end{array} \quad (5.1)$$

We now can expand the vectors \vec{x} and \vec{y} in a combination of two orthonormal sets of n eigenvectors \vec{v}^n and \vec{u}^n , with a n number of eigenvalues λ_n respectively.

Since \mathbf{A} is not a square matrix, these two sets of eigenvectors are not the eigenvectors of matrix \mathbf{A} . These eigenvectors are related to the matrix \mathbf{A} in the following way:

$$\mathbf{A} \vec{v}^n = \lambda_n \vec{u}^n \quad \text{and} \quad \mathbf{A}^T \vec{u}^n = \lambda_n \vec{v}^n \quad (5.2)$$

It can be easily seen that the vectors \vec{v} are the eigenvectors of the matrix product $\mathbf{A}\mathbf{A}^T$ and \vec{u} the eigenvectors of $\mathbf{A}^T\mathbf{A}$. The square matrices $\mathbf{A}\mathbf{A}^T$ and $\mathbf{A}^T\mathbf{A}$ share the same eigenvalues λ_n^2 . Equation (5.1) can thus be rewritten into:

$$\mathbf{A} \vec{x} = \sum_{n=1}^p \lambda_n \vec{u}^{(n)} (\vec{v}_n \cdot \vec{x}) \quad (5.3)$$

where p depicts the number of non-zero eigenvalues, since zero eigenvalues evidently play no further role in the system of equations. The vectors \vec{v} and \vec{u} can be written as columns of matrices \mathbf{V} and \mathbf{U} respectively. These matrices \mathbf{V} and \mathbf{U} span the basis of the vector space for \vec{x} and \vec{y} (as in equation 5.1) since the eigenvectors are orthonormal. Due to the fact that zero eigenvalues

¹For a typical orthonormal matrix \mathbf{M} the following equations hold: $\mathbf{M}\mathbf{M}^T = \mathbf{M}^T\mathbf{M} = \mathbf{M}\mathbf{M}^{-1} = \mathbf{M}^{-1}\mathbf{M} = \mathbf{I}$, where \mathbf{I} is the identity matrix.

are present, these matrices \mathbf{V} and \mathbf{U} can additionally be split into \mathbf{V}_p , \mathbf{V}_0 and \mathbf{U}_p , \mathbf{U}_0 . Matrix \mathbf{A} can therefore be written as:

$$\mathbf{A} = (\mathbf{U}_p \quad \mathbf{U}_0) \begin{pmatrix} \Sigma_p & 0 \\ 0 & 0 \end{pmatrix} \begin{pmatrix} \mathbf{V}_p^T \\ \mathbf{V}_0^T \end{pmatrix} \quad (5.4)$$

Where \mathbf{U}_p and \mathbf{V}_p corresponds to the nonzero eigenvalues, and \mathbf{U}_0 , \mathbf{V}_0 to the zero eigenvalues. The matrix Σ is a diagonal matrix with the square root of the eigenvalues values of $\mathbf{A}\mathbf{A}^T$.

$$\Sigma_p = \begin{pmatrix} \lambda_1 & 0 & 0 & \dots & 0 \\ 0 & \lambda_2 & & \dots & 0 \\ 0 & 0 & \lambda_3 & \dots & 0 \\ \vdots & \vdots & \vdots & \ddots & \vdots \\ 0 & 0 & 0 & \dots & \lambda_p \end{pmatrix} \quad (5.5)$$

Since the matrices \mathbf{U}_0 and \mathbf{V}_0 correspond to the elements of matrices \mathbf{U} and \mathbf{V} which are multiplied with the zero eigenvalues, no contribution of these elements is present in the system of equations (see Snieder and Trampert, -):

$$\mathbf{U}_0^T \mathbf{A} = 0 \quad \text{and} \quad \mathbf{A} \mathbf{V}_0 = 0 \quad (5.6)$$

The matrix \mathbf{U}_0 therefore is known as the data null-space: any component in the data vector (\vec{y}) contained in the subspace \mathbf{U}_0 cannot be explained by any model. In a similar way the matrix \mathbf{V}_0 is the model null-space, model elements of \vec{x} located in this space cannot be resolved by the set of data. The existence of these null-spaces is the reason for the non-uniqueness in any inversion scheme. Matrices \mathbf{U} and \mathbf{V} therefore contain information on the behaviour of the matrix \mathbf{A} in each different space, and can be used to determine the resolution (model space) and optimal sensor location (data space). A geometrical interpretation of the matrices \mathbf{U} , \mathbf{V} and their relation to matrix \mathbf{A} is given in figure 5.1.

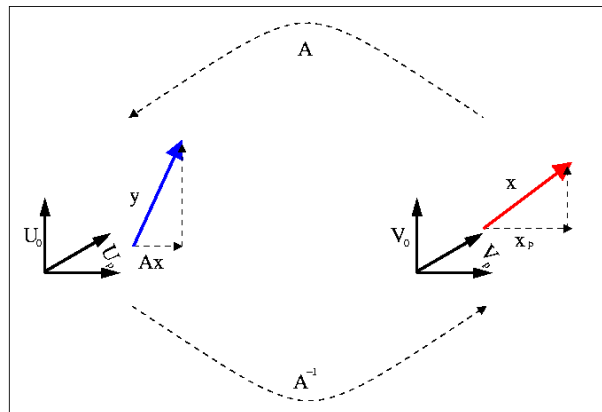


Figure 5.1: Visual interpretation of singular value decomposition, showing the effect of transforming x resp. y from one space to another (after Snieder and Trampert, -).

Starting with a vector \vec{x} on which the linear operator \mathbf{A} acts to transform the model vector \vec{x} to the data vector \vec{y} with the use of equation 5.4. For visualisation purposes we limit ourselves to a three dimensional space, two eigenvectors span the \mathbf{U}_p plane and one eigenvector builds the \mathbf{U}_0 axis. This vector \vec{y} is split therefore into two parts, one lying in the \mathbf{U}_p plane and the other component on the \mathbf{U}_0 axis, perpendicular to the \mathbf{U}_p plane. Returning to the model space, the inverse operator \mathbf{A}^{-1} has to act on the vector \vec{y} and we obtain a vector \vec{x} again, only without the information contained in the blind spots of \mathbf{U}_0 . We therefore only have an estimate of \vec{x} (denoted as \vec{x}_p), generated only by the non-zero eigenvalues, indirectly proving the ground for the non-uniqueness problem of inversion. When the data vector \vec{y} is used as starting point, similar conclusion can be made as in the case of the model vector, components of the data vector that lie on the \mathbf{U}_0 axis cannot be explained by any model.

When only non-zero eigenvalues are in existence in matrix \mathbf{A} (i.e. $\mathbf{U}_0 = \mathbf{V}_0 = \emptyset$), only one unique solution of the inverse calculation is given and the real vectors \vec{x} and \vec{y} can be recovered, depending on starting space, and operation (\mathbf{A} or \mathbf{A}^{-1}).

After expansion of \vec{x} and \vec{y} in the vectors \vec{v} and \vec{u} without the use of the zero valued eigenvalues, the following non-square system of equations can be formulated for the solution of equation 5.3:

$$\vec{x} = \mathbf{V}_p \Sigma_p^{-1} \mathbf{U}_p^T \vec{y} \quad (5.7)$$

where

$$\Sigma_p^{-1} = \begin{pmatrix} \frac{1}{\lambda_1} & 0 & 0 & \dots & 0 \\ 0 & \frac{1}{\lambda_2} & & \dots & 0 \\ 0 & 0 & \frac{1}{\lambda_3} & \dots & 0 \\ \vdots & \vdots & \vdots & \ddots & \vdots \\ 0 & 0 & 0 & \dots & \frac{1}{\lambda_p} \end{pmatrix} \quad (5.8)$$

Note that for small eigenvalues (λ_n) variations in the dataset \vec{y} , due to noise or measurement errors, are exaggerated. This will lead to additional difficulties in solving the system of equations. Therefore only a subset of all available eigenvalues is used, including only eigenvalues larger than a certain threshold value. This step also reduces the CPU time necessary to obtain a solution for the system of equations.

5.1.2 Jacobian Calculation

The Jacobian (\mathbf{J}), or sensitivity matrix, describes the system (denoted by the operator A) in terms of partial derivatives of the measurement datasets to each different model parameter (x_i), where i is the number of model parameters. It therefore can be used to gain insight in the response of the system to changes in the model.

$$\mathbf{J}_{i,j} = \frac{\partial A_j}{\partial x_i} \quad (5.9)$$

In simple cases the Jacobian can be obtained analytically with the use of equation (5.9), but in many cases a numerical scheme must be chosen. In order to numerically evaluate the Jacobian a difference scheme can be used to obtain the partial derivative.

$$\frac{\partial A}{\partial x_i} = \lim_{\Delta x \rightarrow 0} \frac{A(x_i + \Delta x) - A(x_i)}{\Delta x} \quad (5.10)$$

In the case of MERIT the Jacobian describes the magnetic field and electrical potential response due to small changes in the electrical conductivity and can be calculated for several current injection patterns. These Jacobians will later be used to obtain information on the optimum measurement configuration and the resolution of the system.

After obtaining the Jacobian by implementation of equation 5.10 the matrix can than be decomposed in the following way (see 5.4)

$$\mathbf{J} = (\mathbf{U}_p, \mathbf{U}_0) \begin{pmatrix} \Sigma_p & 0 \\ 0 & 0 \end{pmatrix} \begin{pmatrix} \mathbf{V}_p \\ \mathbf{V}_0 \end{pmatrix} \quad (5.11)$$

Following basic matrix algebra, the inverse of \mathbf{J} can now be defined as:

$$\mathbf{J}^{-1} = (\mathbf{V}_p, \mathbf{V}_0) \begin{pmatrix} \Sigma_p^{-1} & 0 \\ 0 & 0 \end{pmatrix} \begin{pmatrix} \mathbf{U}_p \\ \mathbf{U}_0 \end{pmatrix}, \quad (5.12)$$

In the calculations for this chapter the Jacobian is calculated with a Δx of 10 %, further information on the parameterization of the model itself is discussed in Chapter 2).

5.1.3 The Effective Independence Distribution Matrix

The effective independence distribution (Kammer, 1991) is a measure for the behaviour of the system in the model space. The calculation of the effective independence distribution shown here first follows an alternative approach in comparison to Kammer, 1991, and will later be linked to his definitions.

A typical linear system of equations can be written as (compare to 5.1):

$$\vec{y} = \mathbf{A} \vec{x} \quad (5.13)$$

In the case of magnetic and electrical problems however, the system of equations is not linear, therefore a linearized approximation of the problem will be used (see Tillmann et al., 2003) in the following sections. Assuming the inverse of \mathbf{A} exists (i.e. \mathbf{A} square matrix), an estimate of \vec{x} , depicted by \vec{x}_{est} , can be calculated according to:

$$\vec{x}_{est} = \mathbf{A}^{-1} \vec{y} \quad (5.14)$$

If this estimate model vector is inserted into equation 5.13 , an estimate data vector \vec{y}_{est} is calculated, establishing a connection between the forward operator and the data vector.

$$\begin{aligned}\vec{y}_{est} &= \mathbf{A}\vec{x}_{est} \\ &= \mathbf{A}\mathbf{A}^{-1}\vec{y}\end{aligned}\quad (5.15)$$

If instead of any typical forward operator \mathbf{A} , the Jacobian \mathbf{J} is inserted, the influence of the Jacobian on the data vector can be described. This matrix product $\mathbf{J}\mathbf{J}^{-1}$ is known as the effective independence matrix. Unfortunately, the inverse of the Jacobian can often not be calculated since \mathbf{J} is not square. If singular value decomposition is used (by implementing equation 5.7) this problem can be averted (by inserting equation 5.12 for the inverse of \mathbf{J}) and equation 5.15 can be written as:

$$\begin{aligned}\vec{y}_{est} &= \mathbf{J}\mathbf{J}^{-1}\vec{y} \\ &= \mathbf{U}\Sigma\mathbf{V}^T(\mathbf{U}\Sigma\mathbf{V}^T)^{-1}\vec{y}\end{aligned}\quad (5.16)$$

By removal of the null spaces of matrices \mathbf{U} and \mathbf{V} the inverse of \mathbf{J} becomes a square form and the introduction of a singular value threshold eliminates possible singular behaviour due to the determinant of \mathbf{J} .

The effective independence was first introduced by Kammer, 1991 (and later adapted by Poston, 1998), who originally conceived the method for location of on-board monitoring sensors on large space craft. The effective independence distribution matrix (or $\mathbf{E} \equiv \mathbf{J}\mathbf{J}^{-1}$) relates the contribution of each measurement to each different eigenvalue of the dataset.

Kammer, 1991 derived the effective independence distribution matrix in an alternative way, by forming the product $\mathbf{J}^T\mathbf{J}$ and stating that:

$$\mathbf{E} = \mathbf{J}\Psi\lambda^{-1}\Psi^T\mathbf{J}^T \quad (5.17)$$

Where Ψ is a matrix containing all the eigenvectors of $\mathbf{J}^T\mathbf{J}$ and λ the eigenvalues corresponding to these eigenvectors. Since $\mathbf{J}^T\mathbf{J}$ is a square positive definite and symmetric matrix its eigenvalues are real and positive, and its eigenvectors orthonormal, thus:

$$\Psi^T\mathbf{J}^T\mathbf{J}\Psi = \lambda \quad \text{and} \quad \Psi^T\Psi = \mathbf{I}, \quad (5.18)$$

Inserting λ as defined by equation 5.18 in equation 5.17 the independence distribution matrix can be written as:

$$\mathbf{E} = \mathbf{J}(\mathbf{J}^T\mathbf{J})^{-1}\mathbf{J}^T. \quad (5.19)$$

The diagonal of this matrix is known as the effective independence distribution vector (or EID $\equiv \text{diag}(\mathbf{E})$, see Kammer, 1991), and sums the contribution of each measurement location to each eigenvalue of $\mathbf{J}^T\mathbf{J}$. This way a quantitative

image of the importance (in terms of contribution to the eigenvalues of the system of equation) of measurement locations can be obtained. This can be used to first of all determine which measurement locations are redundant, and which are indispensable. In addition this information can be used to compare different measurement strategies in terms of importance. In the case of the MERIT system, one can build a Jacobian for several current injection patterns, and calculate the EID values of all measurement locations for each injection. The current injection with the largest amount of information at a given measurement location can thus be seen as the most preferable current injection.

5.1.4 Adaptations and Assumptions in EID Calculation

Since equation (5.19) is numerically not very stable, and very CPU demanding, several assumptions were made to facilitate the use of large sensitivity matrices in a reasonable amount of time. By application of the orthogonality relations of the SVD matrices one can write:

$$\begin{aligned}
& \text{if: } \mathbf{J} = \mathbf{U}\mathbf{\Sigma}\mathbf{V}^T \\
& \text{then } \mathbf{E} = \mathbf{J} \left[\mathbf{J}^T \mathbf{J} \right]^{-1} \mathbf{J}^T \\
& \quad = (\mathbf{U}\mathbf{\Sigma}\mathbf{V}^T) \left[(\mathbf{U}\mathbf{\Sigma}\mathbf{V}^T)^T \mathbf{U}\mathbf{\Sigma}\mathbf{V}^T \right]^{-1} (\mathbf{U}\mathbf{\Sigma}\mathbf{V}^T)^T \\
& \quad = (\mathbf{U}\mathbf{\Sigma}\mathbf{V}^T) \left[\mathbf{V}\mathbf{\Sigma}\mathbf{U}^T \mathbf{U}\mathbf{\Sigma}\mathbf{V}^T \right]^{-1} (\mathbf{U}\mathbf{\Sigma}\mathbf{V}^T)^T \quad (5.20) \\
& \quad = (\mathbf{U}\mathbf{\Sigma}\mathbf{V}^T) \left[\mathbf{V}\mathbf{\Sigma}\mathbf{\Sigma}\mathbf{V}^T \right]^{-1} (\mathbf{U}\mathbf{\Sigma}\mathbf{V}^T)^T \\
& \quad = \mathbf{U}\mathbf{\Sigma}\mathbf{V}^T \mathbf{V} \left[\mathbf{\Sigma}^2 \right]^{-1} \mathbf{V}^T (\mathbf{U}\mathbf{\Sigma}\mathbf{V}^T)^T \\
& \quad = \mathbf{U}\mathbf{\Sigma} \left[\mathbf{\Sigma}^2 \right]^{-1} \mathbf{\Sigma}\mathbf{U}^T.
\end{aligned}$$

Where $\mathbf{\Sigma}^2$ denotes a diagonal matrix with the square of all elements of $\mathbf{\Sigma}$ on its diagonal. If the problem is well posed, matrix $\mathbf{\Sigma}$ only contains non-zero eigenvalues, in which case the $\mathbf{\Sigma}(\mathbf{\Sigma}^2)^{-1}\mathbf{\Sigma}$ term reduces to the identity matrix \mathbf{I} , and $\mathbf{U}\mathbf{U}^T$ also (due to orthogonality). In other words, each measurement point contributes the same to the eigenvalues and each diagonal element of \mathbf{E} becomes a value of 1. In the case of an ill-posed problem, this is not the case, and both matrices $\mathbf{\Sigma}$ and \mathbf{U} need to be split into subsets, dividing the non-zero eigenvalues from the zero eigenvalues (see equation 5.8). Equation 5.20 can then be expanded by an additional term:

$$\begin{aligned}
\mathbf{E} &= \mathbf{U}\mathbf{\Sigma} \left[\mathbf{\Sigma}^2 \right]^{-1} \mathbf{\Sigma}\mathbf{U}^T \\
&= \begin{pmatrix} \mathbf{U}_p \\ \mathbf{U}_0 \end{pmatrix} \begin{pmatrix} \mathbf{\Sigma}_p & 0 \\ 0 & 0 \end{pmatrix} \begin{bmatrix} \mathbf{\Sigma}_p^2 & 0 \\ 0 & 0 \end{bmatrix}^{-1} \begin{pmatrix} \mathbf{\Sigma}_p & 0 \\ 0 & 0 \end{pmatrix} \begin{pmatrix} \mathbf{U}_p \\ \mathbf{U}_0 \end{pmatrix}^T \quad (5.21) \\
&= \mathbf{U}_p \mathbf{U}_p^T
\end{aligned}$$

Note that expanding matrices \mathbf{U} and $\mathbf{\Sigma}$ at this point (and thus leaving matrix \mathbf{V} in one piece) into the two subsets by taking the non-zero eigenvalues into account does not violate any mathematical rules. The product $\mathbf{V}^T \mathbf{V} = \mathbf{V}_p^T \mathbf{V}_p \equiv \mathbf{I}$ in contrast to the product $\mathbf{U}\mathbf{U}^T \neq \mathbf{U}_p \mathbf{U}_p^T$.

In order to calculate the EID with 4 matrix multiplications and an inverse, only a decomposition in SVD and one matrix multiplication also is sufficient, only the diagonal matrix $\mathbf{\Sigma}$ needs to be inverted, and multiplied with \mathbf{V} and \mathbf{V}^T . This leads to a relative faster and more stable EID routine when \mathbf{J} first is decomposed in its singular values. The EID will give rise to values in the [0,1] domain, depicting unimportant elements of the data vector (i.e. a small or no contribution to the eigenvalues) with 0 and important data points with 1.

The same expression for \mathbf{E} , and thus the EID, can be obtained if equation 5.16 is inserted in equation 5.20, proving the similarities between \mathbf{E} as derived by Kammer and from basic inversion considerations as presented in the first part of the subsection.

5.1.5 Resolution Calculation

The resolution of the system can be calculated in a similar way as the effective information density (see Tillmann et al., 2003), by studying the behaviour of the system in the model space. The model vector (\vec{x}) first is transformed to the data space by an operator \mathbf{A} and subsequently transformed back into model space (by multiplication with the inverse operator \mathbf{A}^{-1}). This way the effect of the loss of resolution due to the model null space can be studied, and only an estimate of the original vector is returned (as depicted in figure 5.1). When singular value decomposition is used to obtain a solution for the inverse problem and the orthogonal behaviour of the matrix \mathbf{U} is used we obtain:

$$\vec{y} = \mathbf{A} \vec{x} \quad (5.22)$$

$$\begin{aligned} \vec{x}_{est} &= \mathbf{A}^{-1} \vec{y} = \mathbf{A}^{-1} \mathbf{A} \vec{x} \\ &= \mathbf{V} \mathbf{\Sigma}^{-1} \mathbf{U}^T \mathbf{U} \mathbf{\Sigma} \mathbf{V}^T \vec{x} \\ &= \mathbf{V} \mathbf{V}^T \vec{x} \end{aligned} \quad (5.23)$$

The estimated model vector (\vec{x}_{est}) can be obtained by multiplication of the real model (\vec{x}) by the matrix product $\mathbf{V} \mathbf{V}^T$. If \mathbf{J} does not exhibit non-unique behaviour, i.e. the matrix $\mathbf{V}_p = \mathbf{V}$, it follows from the orthogonality relations of \mathbf{V} in equation 5.23, that $\mathbf{V} \mathbf{V}^T = \mathbf{I}$, and the rank of $\mathbf{V} \mathbf{V}^T$ is equal to the number unknown model parameters. This means all parameters can be uniquely resolved, exactly what a unique matrix \mathbf{J} describes, the matrix $\mathbf{V} \mathbf{V}^T$ is known as the resolution matrix. The diagonal $\mathbf{V} \mathbf{V}^T$ (known as the resolution vector, or RES) illuminates the model parameters which can be resolved, and hides the ones which are non-solvable by assigning a value between [0 (non-resolvable), 1 (resolvable)] to each model parameter (see also Wiggins, 1972 and Sen and Stoffa, 1995).

Note the similarity between the resolution and the effective independence, both parameters are derived using similar arguments, although in different space (i.e. data and model space).

5.1.6 The Singular Value Threshold

In a typical MERIT dataset, the number of measurements is much larger than the number of model parameters. Unfortunately the non-uniqueness of any magnetic or electrical problem will cause the matrix Σ to have a deficit rank:

$$\Sigma = \begin{bmatrix} \Sigma_p & 0 \\ 0 & 0 \end{bmatrix}. \quad (5.24)$$

This over-determined system of equations will give rise to EID and RES matrices very close to \mathbf{I} . Omitting the zero eigenvalues of the matrix Σ will not affect the matrix \mathbf{V} , since the reduction only affects the rows of Σ . The matrix \mathbf{U} on the other hand is greatly affected, by reduction of the rows of Σ , it will lose the same amount of columns. This will change the EID matrix considerably, and its form will no longer be close to \mathbf{I} . This effect allows the existence of the EID vector in the first place and allows to discern between important and non-important elements of the data vector.

The matrix Σ_p consist of all eigenvalues, even the ones which are very small, these small eigenvalues will give rise to problems in real measurements. The small eigenvalues, will exaggerate effects of noise in the system of equations (as described in section 5.1.1). Introduction of a singular value threshold will limit the exaggeration effects considerable. Therefore the equations used to calculate the EID and RES vectors of the system actually has the form:

$$\begin{aligned} \text{EID} &= \text{diag}(\mathbf{U}\Sigma_t^{-1}\Sigma_t\mathbf{U}^T) \\ \text{RES} &= \text{diag}(\mathbf{V}\Sigma_t^{-1}\Sigma_t\mathbf{V}^T) \end{aligned} \quad (5.25)$$

where t is a chosen threshold value. The fact that the very small singular values are omitted (in the following calculation the cut-off threshold was fixed at $\frac{1}{5000}^{th}$ of the maximum singular value) of course reduces the amount of information available in the data.

In actual measurements this threshold is much to low, it causes errors in the measurement to be blown up to gigantic proportions in comparison to the very small eigenvalues containing the desired information. For numerical modeling, where the only error introduced is the machine (or SVD algorithm) precision this threshold may work, normally a threshold of $\frac{1}{1000}$ or even larger (if the data is very unreliable due to noise effects) is chosen. Figure 5.2 shows a typical eigenvalue spectrum, and the effect of the introduction of a singular value threshold, with a $\frac{1}{1000}$ threshold, more than half of the eigenvalues are omitted, thus diminishing the information contained in the system of equations. For the calculations a threshold of $\frac{1}{5000}$ was therefore used, containing at least half of all eigenvalues available, this effect is of course highly dependable on the structure of the eigenvalue spectrum, and thus of the problem to be solved.

5.2 The Optimal Measurement Configuration

The application of the EID routines (see equation 5.21) leads to an image of the importance of all data points present in the dataset. This information can be

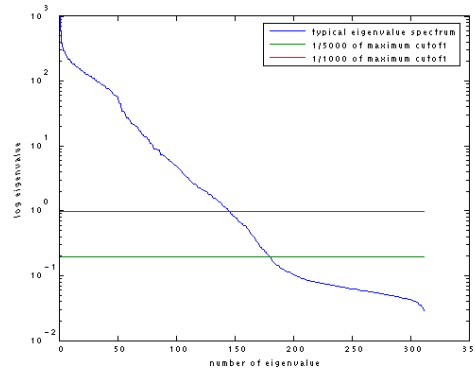


Figure 5.2: A typical Eigenvalue spectrum of a MERIT dataset, and two possible eigenvalue threshold values.

used to discriminate important measurements from unimportant ones, and thus to increase the speed of a measurement by reducing the amount of measurements to the ones which contribute heavily to the eigenvalues of the Jacobian. Alternatively, if the Jacobian consists of several different current injection patterns, the EID can be used to determine which data vector from one current injection contains the most information, and thus which current injection pattern has to be preferred in terms of information content.

The measurement system designed for the MERIT system (see chapter 3) leads to some limitations on the electrode and magnetic field sensor locations. The electrodes used in this system are located on three horizontal planes, each with 5 electrodes evenly spread along the column casing. The magnetic field sensors are located on a vertically moving scanning torus system with 24 modules, evenly spaced along the torus. Each sensor module is located 5 cm from the column casing and measures the three components of the magnetic field. The numerical models used to obtain the optimal measurement configuration will reflect both hardware criteria (see figure 5.3).

The three planes of 5 electrodes lead to 105 possible current injection patterns, and potential difference measurements. Here two subsets will be studied, the horizontal dipole² (containing 10 possible dipoles per plane) and the vertical dipole (with 15 possible dipoles) subsets. No combination of both subsets (i.e. across the column) will be studied.

5.2.1 Horizontal Current Injection Scenarios

The horizontal current injection dipoles are most often used in the study of the electrical properties of core samples. In order to limit the dataset used to calculate the Jacobian and the further EID processing, not the complete finite

²Strictly speaking the current injection dipole is a bipole, the electrode spacing is too coarse for a true dipole. During the rest of this thesis, however, the term dipole will be used in order to emphasize the method MERIT (i.e. the addition of the magnetic field measurements to traditional resistivity measurements) and use normal resistivity survey terminology.

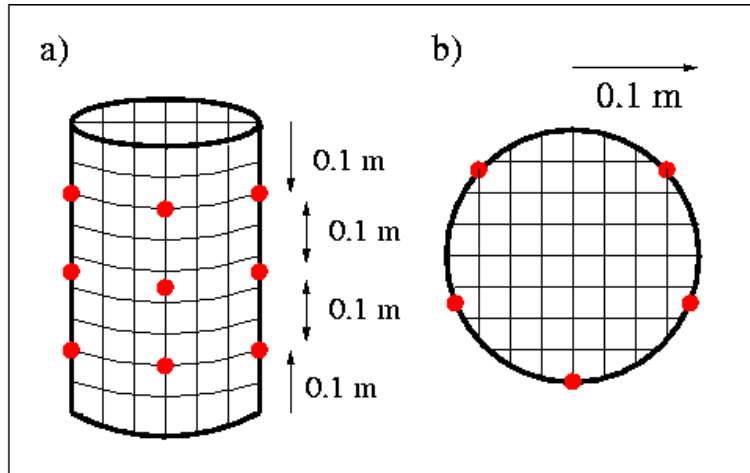


Figure 5.3: Current electrode distribution and numerical model used for resolution calculation, a) side view, b) top view.

element grid was used in the Jacobian calculation. A zone of interest was defined, containing the 7 middle layers of the modelled column, and the Jacobian was only calculated with perturbations of the model in this zone. For all further processing steps the complete column was used, only the Jacobian was limited to the zone of interest. The data itself will consist of 24 measurements of the 3 components of the magnetic field on a single vertical plane (in a circular layout). In addition the electrical potential will be modelled at 48 points along the column, and both measurements will be modelled at 44 vertical planes.

The dimensions of the model used were similar to the actual measurement column (0.1 m radius and 0.4 m height), the magnetic field data were calculated for sensors at a distance of 5 cm from the casing. Since the whole system has a cylindrical layout, dipole lengths in the horizontal plane will be depicted in degrees instead of the usual distance.

Since five electrodes are available per plane no injection dipole straight through the column can be made (i.e. 180 degrees between C_1 and C_2), therefore a dipole length of 144 degrees was used in the first investigations. In this scenario three different dipoles are possible, each at a different injection plane. The data is presented as folded out cylinder mantles, similar to the magnetic fields presented in chapter 4 (see figures 4.11 and 4.12). The ERT data is presented in a similar way as the magnetic field data (i.e. pure electrical potential values at the cylinder mantle), and thus not similar to traditional ERT data, in which only electrical dipoles can be measured.

During the rest of the thesis the data will be presented in this way.

From figure 5.4 one can easily see the huge importance of the ERT³ dataset

³Note that these ERT values are pure electrical potentials and not the electrical potential differences as used in a typical ERT survey

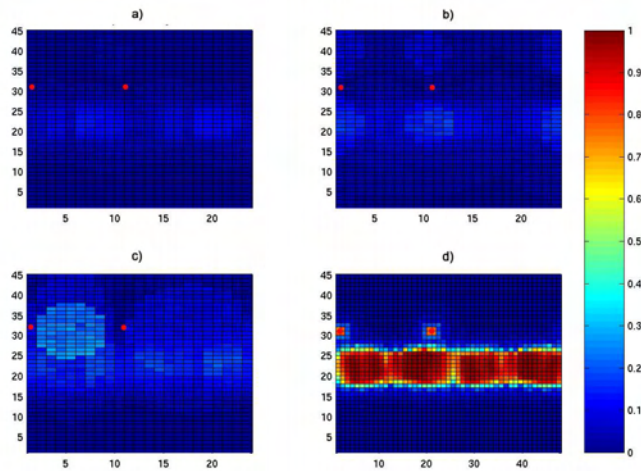


Figure 5.4: EID results, horizontal current injection, figures a),b) and c) denote the EID values for the x,y and z component of the magnetic field, figure d) the EID values for the electrical potential data

when compared to the MMR data, where the ERT data have values close to 1 (i.e. the red colours), the magnetic field data does not have EID values much higher than 0.15 (depicted as bluish pixels). For comparison reason both the ERT dataset and the MMR data set in the Jacobian were weighted with their maximum value, to limit the effect of the huge difference in magnitude of the signal (V in the case of the ERT data versus nT in the MMR data). This difference affects the eigenvalues of the Jacobian of a MERIT dataset, the large values of the electrical part produce larger eigenvalues and thus bias the eigenvalue cutoff (and the EID calculation) to the ERT data. Figure 5.5 shows all EID values at the cylinder mantle are plotted as a curve, the three magnetic field components at first (in blue), the electrical potential data behind (in red). Here the difference in importance is even more clear.

This could lead to the conclusion that ERT data contains practically all information in comparison to MMR data, and the addition of MMR data will only lead to a minimal increase in information. Which is true for this modelled geometry, however, one has to keep in mind that these ERT data are not data which practically can be obtained by traditional ERT techniques. It consists of a data set of electrical potential data which a large sampling density: 48 measurements on a circle with a circumference of only 0.628 m and each 0.01 m a measurement plane along a height of 0.44 m. This way the small cylinder is equipped with 2112 electrodes, a number which is not practically useful. This large number of electrical potential measurements is chosen in order to be able to compare the magnetic field and electrical field data on the level of the magnetic data, i.e. to treat both data types as obtained in a similar fashion. This way both dataset are treated as pure measured values, which is true for the magnetic field, but the electrical potential is only measured as potential

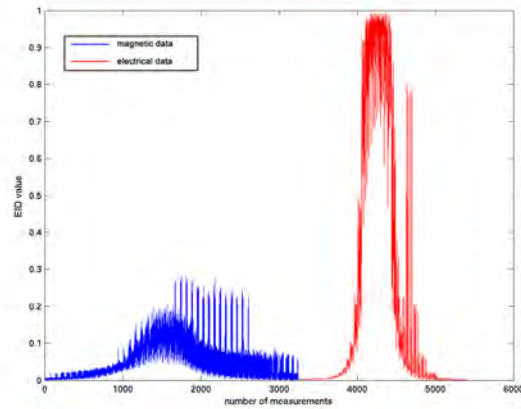


Figure 5.5: EID values for a horizontal current injection, included are data for both electrical potential and magnetic field data.

difference between two electrodes.

In the case of the real column on 13 electrodes are available (15 - 2 for current injection), this will lead to such a small amount of electrical data in comparison to the magnetic dataset that the comparison would be erroneous due to differences in dataset size. Limiting the magnetic field data to the level of the ERT data would have caused problems due to the under-determined nature of such a problem (i.e. number of measurements vs. number of model parameters). Since the main focus of the thesis lies on the magnetic field measurements, the first option was chosen.

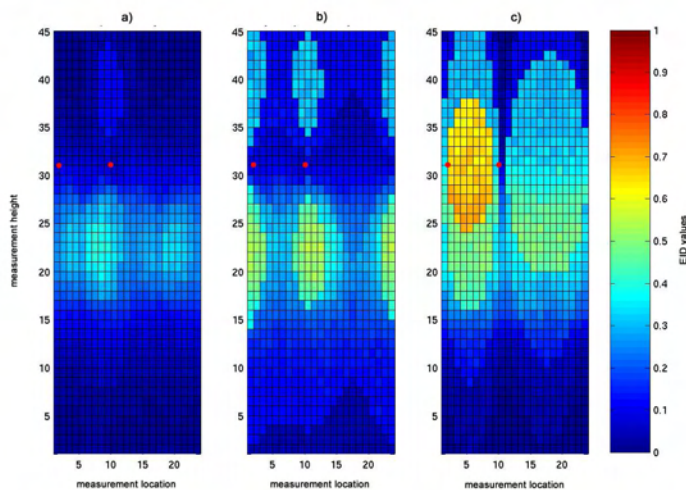


Figure 5.6: EID calculations, top ring horizontal current injection, figures a), b) and c) denote the EID values for the x, y and z component of the magnetic field.

If a closer look of the MMR data is taken (and the EID values are calculated without the addition of the ERT data), figure 5.6 can be obtained. The important data points are biased towards the top of the column, due to the location of the electrodes in the top part. The x component does worst in terms of information, but only slightly worse than the y-component. The z-component data clearly has the largest amount of information about the electric conductivity distribution.

Data points in the lower part of the column do not contribute much since due to the current injection configuration the current will be concentrated in the top part, and so does the magnetic field. When the horizontal injection dipole is lowered to the middle electrode ring, an unwanted effect occurs (see figure 5.7).

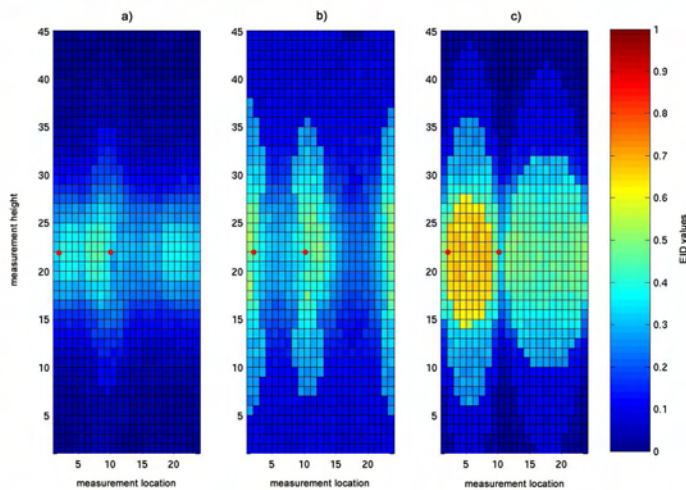


Figure 5.7: EID calculations, middle ring horizontal dipole current injection, figures a),b) and c) denote the EID values for the x,y and z component of the magnetic field.

The area in the close vicinity of the electrodes is deemed important, unfortunately the area around the electrodes is not modelled correctly (see chapter 2). In close vicinity of the electrodes the difference between numerical and analytical solution of the electric potential and magnetic field is largest (about 0.4 %). This causes an additional error in the reconstruction (on top of 'normal' errors like noise). The most important measurement locations are thus modeled less accurate, making this data set unusable in our applications.

Returning to the top electrode ring, the EID values of a smaller dipole (72 degrees dipole length, see figure 5.8). and a larger dipole (216 degrees) were also calculated (see figure 5.9).

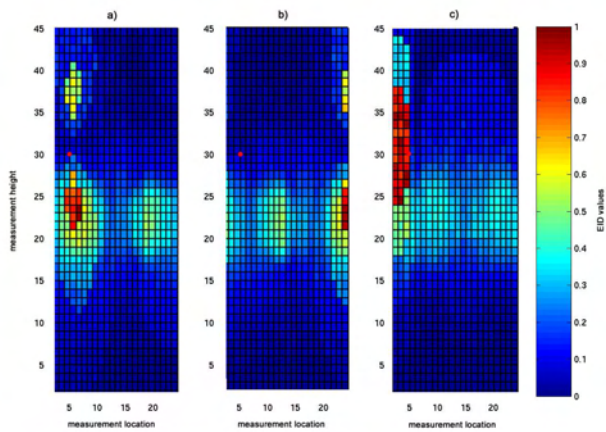


Figure 5.8: EID values for a 72 degrees horizontal dipole current injection, figures a),b) and c) denote the EID values for the x,y and z component of the magnetic field.

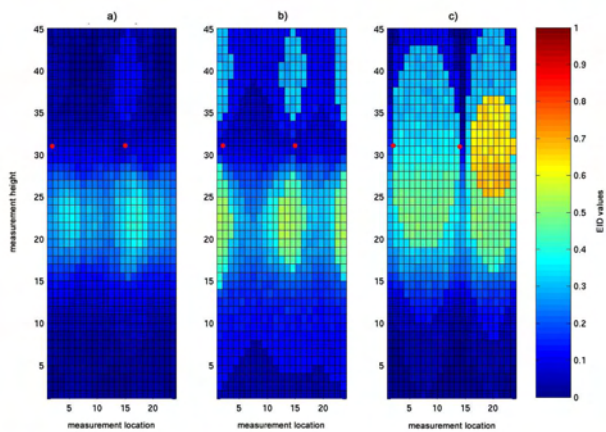


Figure 5.9: EID values for a 216 degrees horizontal dipole current injection, figures a),b) and c) denote the EID values for the x,y and z component of the magnetic field.

The 72 degrees current injection brings similar problems as the middle current injection (see figure 5.7), the most important measurements are located in close proximity to the electrodes, where the numerical modeling has the largest deviation from the analytical solution. The difference between the 216 degrees dipole and the 144 degrees is practically not present, since the minimum distance from electrode to electrode is in both cases 144 degrees (clock wise for the 144 degree dipole, anti-clockwise for the 216 degrees).

5.2.2 Vertical Current Injection Scenarios

The subset vertical dipoles is divided into two parts (see figure 5.3), the so-called large dipoles (with C1 located at the bottom row and C2 at the top) and the small dipoles (C1 at the top, C2 the at middle or C1 at the the middle and C2 at the bottom). At first a typical large dipole scenario will be studied and the comparison between the ERT data and MMR data will be made:

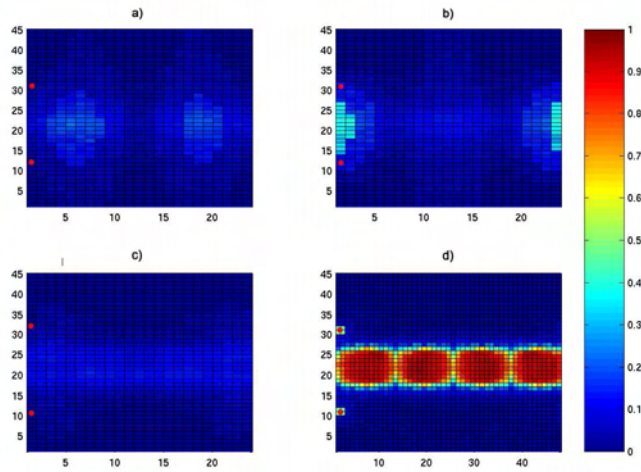


Figure 5.10: EID values for a vertical current injection, located at 0 degrees. figures a),b) and c) denote the EID values for the x,y and z component of the magnetic field, figure d) the EID values for the electrical potential data

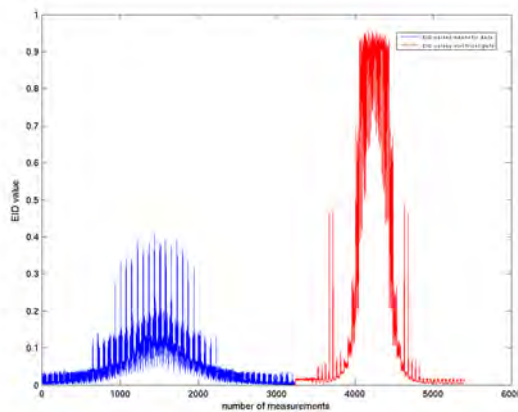


Figure 5.11: EID values vertical current injection, located at 0 degrees. Both electrical potential and magnetic field data are presented.

Similar as in the case of the horizontal dipoles (see 5.4), the ERT data contains the most important measurements (again the ERT data are located in the latter part of the data vector as shown in figure 5.11). But as discussed in the previous

section these results can only be obtained in modelling and not in a practical experiment. When only the magnetic data is used in the EID calculation (see figure 5.12) the decrease in importance of the z-component in ,comparison to the y-component, becomes even more apparent (in comparison to figure 5.6).

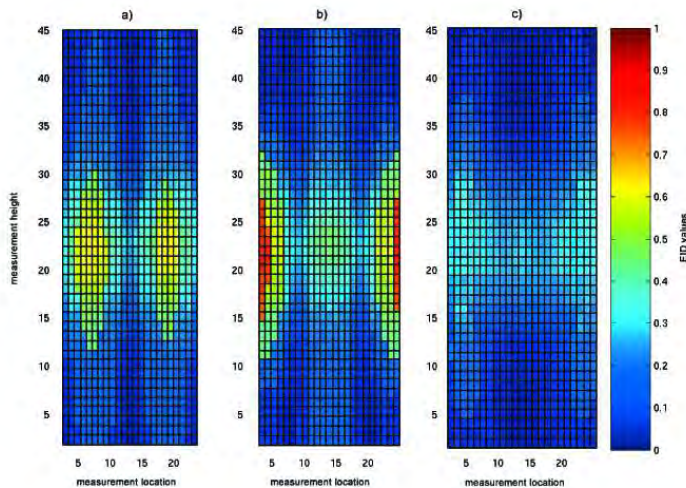


Figure 5.12: EID calculations, single vertical current injection, 0 degrees, figures a),b) and c) denote the EID values for the x,y and z component of the magnetic field.

Due to the different sensitivity behaviour of a large dipole scenario the area around the electrodes is deemed less important than in the horizontal dipole scenarios. Also the shape of important zones the are more biased toward the vertical direction.

Keeping in mind the measurement system layout with a limited number of sensors in the horizontal plane, and a very good positioning accuracy of the vertical moving belt, leads to a preference of the vertical scenarios over horizontal ones.

Small dipole scenarios come in two kinds, a top (top and middle electrodes) and a bottom type (middle and bottom electrodes). Both show (see figures 5.14 and 5.13) the expected bias in importance to the top and bottom part of the measurement locations respectively. But due to the fact that a homogeneous model is used no real difference between both scenarios exists, as was to be expected.

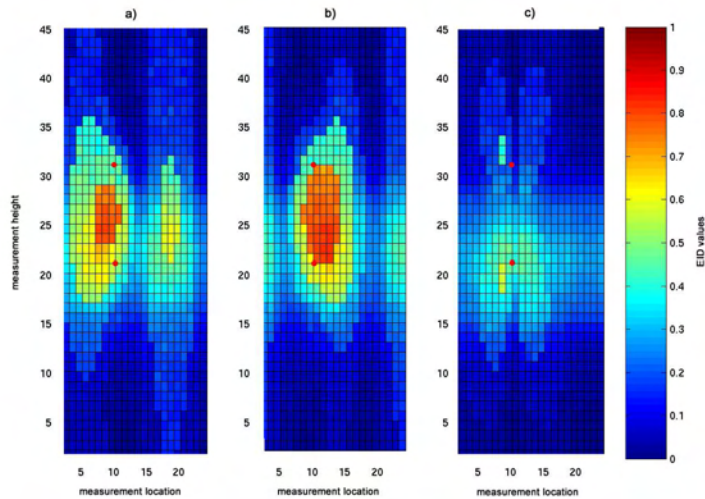


Figure 5.13: EID results vertical current injection, top electrodes, figures a), b) and c) denote the EID values for the x, y and z component of the magnetic field.

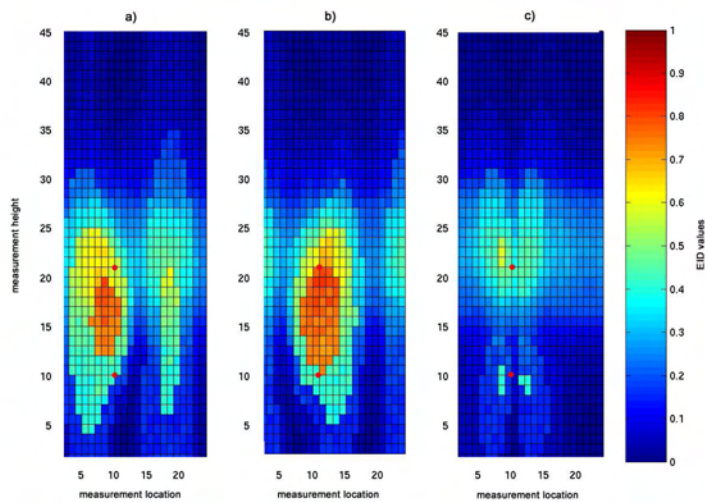


Figure 5.14: EID results vertical current injection, bottom electrodes, figures a), b) and c) denote the EID values for the x, y and z component of the magnetic field.

5.2.3 Concluding Remarks on the Optimum Configuration

Comparison between the two different current injection scenarios can be made by looking at the EID values itself. When both a horizontal dipole scenario and a vertical dipole scenario are used in the EID calculation, a choice can be made on the importance of data obtained in both data sets. Figure 5.15 therefore shows the EID values of 3 datasets, one joint set with both horizontal (middle electrode ring) and large vertical dipole measurements, and the EID values of both data sets calculated separately. Only the magnetic field data is used, and all components of the magnetic field are included.

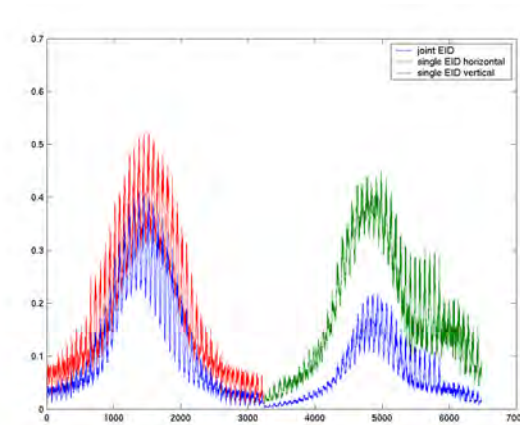


Figure 5.15: EID values for comparison between horizontal and vertical dipole data sets

At first the difference in amplitude of the values between the joint and the single data sets is apparent, this can be explained by the increase in data points, the more data points are available the larger the subset of important data points becomes. This causes the absolute EID value of individual points to decrease, and leads to an apparent decrease. The horizontal data subset of the joint data set shows an increased lowering of the EID values, in comparison with the vertical data subset. This indicates that in a direct comparison the horizontal data subset is less important for reconstruction purposes than the vertical data subset.

A comparison between large and small vertical dipoles leads to an expected conclusion (see figure 5.16). Similar as in a traditional DC resistivity sounding survey, the current density distribution in the small dipole scenario tends to be more concentrated than the large dipole. This concentration of current gives rise to a limited amount of information on the electrical conductivity. The overall information contained in the large dipole is larger than in the small dipole, although the difference is less pronounced as in the comparison between vertical and horizontal dipoles.

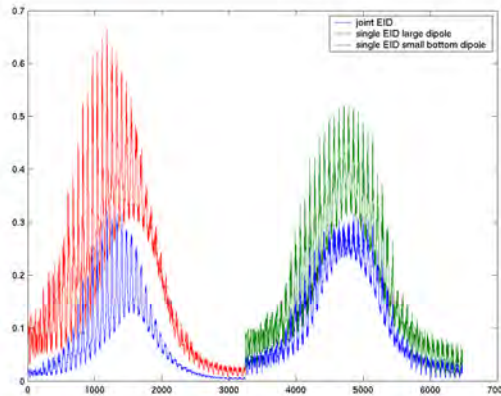


Figure 5.16: EID values for comparison between small and large vertical dipole data sets

The final conclusion on the type of current injection pattern was additionally influenced by the numerical approximations made in the forward algorithms. When the difference between the numerical and analytical solution for a typical, in this case horizontal, current injection is studied (see chapter 2), the relative large error in the vicinity of the electrodes is apparent. Therefore the vertical dipole injections will be preferred above the horizontal injections. In the vertical dataset the areas around both electrodes is deemed non-important, whereas the horizontal datasets depends more heavily on the data in the vicinity of the electrodes. When the numerical solution is less accurate in this area, additional errors will be introduced, which can be avoided by choosing the current injection of more favourable scenarios.

Both arguments combined lead to the conclusion that the MERIT system will mainly use vertical dipole current injections instead of horizontal scenarios. The effect of this conclusion on the resolution of the whole system will be discussed in the following section.

5.3 Resolution of the MERIT System

In this section the resolution of the MERIT system will be discussed (see Tillmann et al., 2003 and Sen and Stoffa, 1995), and compared to those of traditional ERT and MMR datasets. Since the large vertical dipole scenario gives rise to less error and contains more information (as described in the previous section) mainly large vertical current injection patterns will be studied. The horizontal dipole will only be included as reference and only for a homogeneous model. In order to compare both datasets both datasets will consist of data from the same amount of measurement locations (i.e. 24 ERT measurement positions⁴ located at the surface of the column per vertical level, and 24 magnetic field sensor positions located 5 cm away from the column mantle per vertical level). In total the length of the column is divided into 40 height levels. This will not be the case in the actual MERIT measurement setup where only a limited number of electrodes will be used (see chapter 3). As current injection electrodes only the 15 available electrode locations will be used.

Three different models will be used to determine the resolution vector (by calculation of the diagonal of the resolution matrix, see equation 5.23), a homogeneous column and the so-called resistive and conductive shielding model. The Jacobians themselves will consist of only a single plane of perturbed elements in order to leave the CPU time needed for the calculation in acceptable levels.

5.3.1 Resolution of Homogeneous Scenarios

The first model to be studied is a homogeneous column ($\sigma(r) = 0.1 \frac{S}{m}$) as depicted in figure 5.3. As current injection both the horizontal (with a dipole length of 144 degrees) and a large vertical dipole will be modelled. The horizontal current injection is located at the middle of the column height (as is the perturbed plane), the large vertical dipole (between the top and bottom electrode) at 0 degrees. Results of the resolution calculations (depicted as RES values) will be presented as cut-through of the column, showing the resolving capabilities for each model parameter present in the Jacobian.

⁴Again pure electrical potentials will be used in contrast of the electrical potential difference.

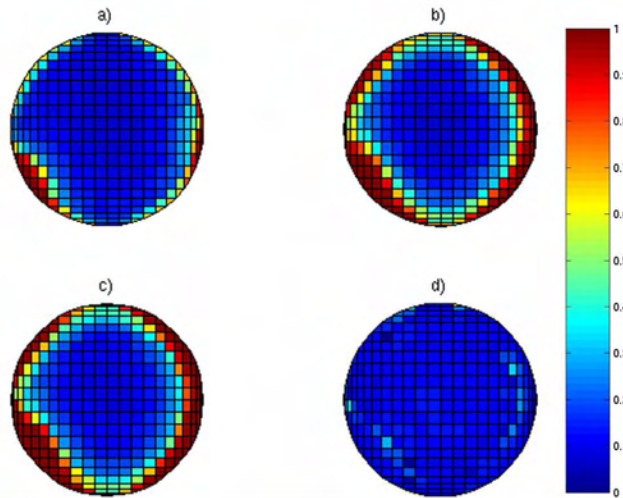


Figure 5.17: Homogeneous column scenario, horizontal current injection, 144 degrees, middle electrode ring, a) resolution of the MMR dataset, b) resolution of the ERT dataset, c) resolution of the MERIT dataset, d) difference in resolution between the MERIT and the ERT dataset

The additional value of the magnetic field in the horizontal dipole dataset (figure 5.17) is not that apparent as in the vertical dipole dataset (figure 5.18, which reinforces the results of the EID calculation). The differences in resolution are more striking in the vertical dipole data (compare the light blue interior grid cells of figure 5.18 c with 5.17 c), although also inherent in the horizontal data. The increased ability of the MMR data set to resolve model parameters in the interior of the column is very striking. The ERT data on the other hand, has a much better (near to perfect) resolution for the outer rim of the column. The MERIT dataset doesn't show the solving capability of the interior as good as a single MMR data set, but incorporates the near perfect resolution of the ERT data. It still has a better resolution than the ERT data for the interior (as visible in the difference between MERIT and ERT). The lack of resolution in the inner part of the column lies in the singular values of the MMR data set, which are rather small in comparison with the ERT data in this case. Due to the singular value decomposition and the implementation of the singular value threshold, most singular values present in the MERIT dataset are contributions of the ERT data, and the MMR data is represented in a lesser degree.

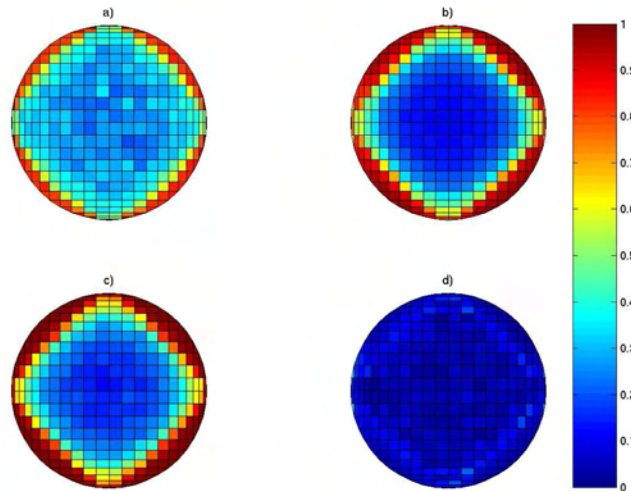


Figure 5.18: Homogeneous column scenario, vertical current injection, a) resolution of the MMR dataset, b) resolution of the ERT dataset, c) resolution of the MERIT dataset, d) resolution difference between the MERIT and the ERT dataset

5.3.2 Resolution of the Resistive Shield Scenario

As mentioned before in the early 1970's symmetry considerations made by Edwards, 1974 and Seigel, 1974 pointed out the increased sensitivity of MMR data to conductive or resistive shielded objects in comparison to traditional resistivity data. In order to prove these statements by resolution calculation two shielding models were constructed, in this section the resistive shielding model will be studied (see also Tillmann et al., 2004 and Verweerd et al., 2004), in the next a conductive shielding model will be presented.

The resistive shielding model consists of a background conductivity of $0.1 \frac{S}{m}$ in which a resistive ($0.001 \frac{S}{m}$) body is located. Inside this body a smaller conductive body is placed with a conductivity of $1 \frac{S}{m}$. A 100 mA current is applied in both a 144 degree horizontal dipole and as a large vertical dipole.

Again similar effects as in the homogeneous model occur when horizontal current injection and vertical current injection are compared, the main focus will therefore lie on the vertical dataset (figure 5.21). The MMR data clearly shows a higher resolution for the conductive layer than the ERT data, where only the outer corners show some resolution. The ERT data on the other hand shows a much better resolution for the outer rim of the column than the MMR data. The MERIT dataset clearly takes the best of both worlds, the good resolution of the outer elements combined with the good resolution of the inner conductive layer. In comparison with figure 5.18 the singular values in this MERIT dataset compromise a larger portion MMR data, hence the greater effect of the MMR data (i.e. better resolution in the interior). The difference between contribu-

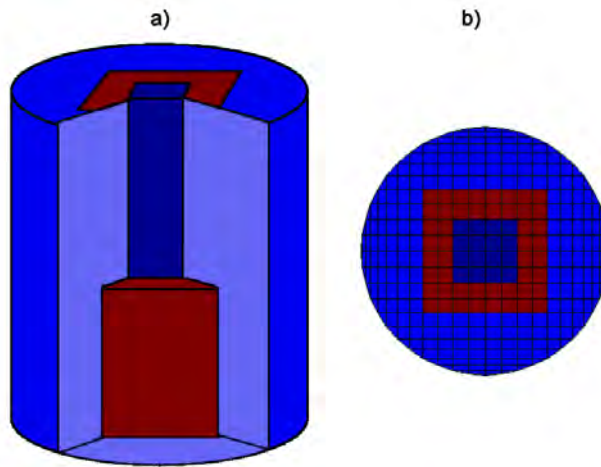


Figure 5.19: Shielded model configuration, a) as side view, b) top view, the different colours denote different electrical conductivities (see text for more details).

tions of the MMR data set in figures 5.18 and 5.21 shows also the importance of the choice of the singular value threshold.

Comparing the results for a horizontal and a vertical current injection dipole, the increase in resolution for the vertical dipole scenario is very great in comparison to the horizontal dipole scenario. Not only does it show more resolution in the outer layer, it even is able to obtain a much better resolution inside the resistive shielding.

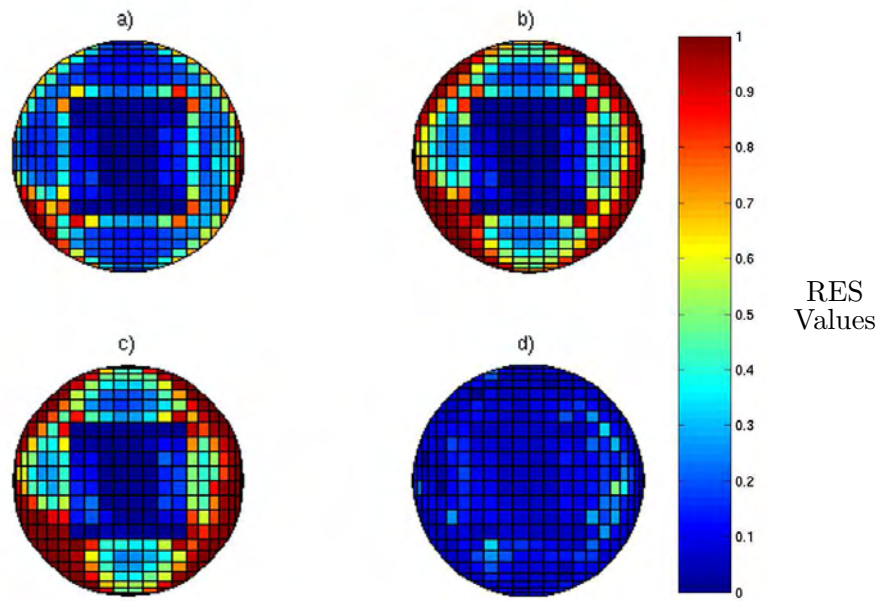


Figure 5.20: Resistive shielding scenario, horizontal dipole, 144 degrees, a) resolution of the MMR dataset, b) resolution of the ERT dataset, c) resolution of the MERIT dataset, d) resolution difference between the MERIT and the ERT dataset

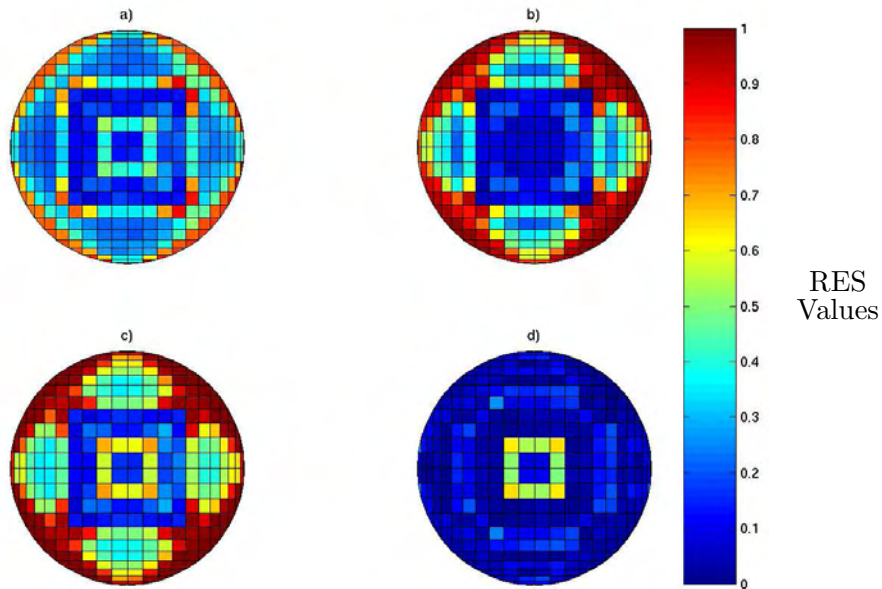


Figure 5.21: Resistive shielding scenario, vertical dipole, a) resolution of the MMR dataset, b) resolution of the ERT dataset, c) resolution of the MERIT dataset, d) resolution difference between the MERIT and the ERT dataset

5.3.3 Resolution of the Conductive Shield Scenario

The conductive shielding scenario is practically the opposite of the conductive shielding, the background conductivity is kept at $0.1 \frac{S}{m}$ but this time the outer layer of the body is conductive ($\sigma = 1 \frac{S}{m}$) and the inner body has the high electrical resistivity of $0.001 \frac{S}{m}$. Only a vertical dipole scenario will be shown, due to the increased resolution differences between the MERIT and ERT datasets in comparison to a horizontal scenario as shown in the conductive shielding scenario (see figure 5.21).

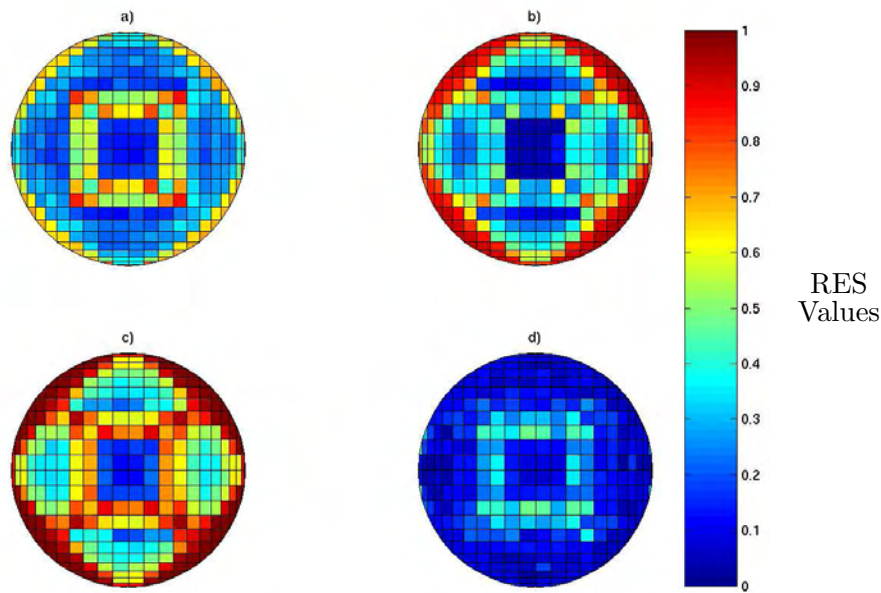


Figure 5.22: Conductive shielding scenario, vertical dipole a) resolution of the MMR dataset, b) resolution of the ERT dataset, conductive scenario. c) resolution of the MERIT dataset, d) resolution difference between the MERIT and the ERT dataset

Again the similar advantages of the MMR dataset in comparison with the ERT dataset are apparent as in the case of the conductive shielding scenario. This time more striking for the conductive shield, the ERT dataset shows the outline of the body, whereas the MMR data allows a near perfect resolution of the conductive shield. Also the inner resistive body is slightly better resolved in the MERIT data than in the ERT data set. Again the near perfect resolution of the ERT data for the outer rim is well retained in the MERIT dataset.

5.4 Under-determined Systems and Resolution Matrix Rank

Not only the spatial distribution of the resolution matrix on the model space gives information on the resolving capabilities of the system. The rank of the resolution matrix depicts the number of resolvable parameters in the system. This information can also be used to study the additional value of a MMR dataset in conjunction with the conclusions made in the previous section. But the problem can also be studied in a more general way: How does the number of observations influence the resolution of the datasets ?

In this section a single large vertical current injection Jacobian (for a homogeneous column) will be used to study the effect of the number of data points on the resolution. Also the singular value threshold will be discussed (as used in equation 5.8), since that is the most important parameter behind the resolution calculations.

5.4.1 MMR Datasets

When the amount of data points is taken into account which are obtained by a three component magnetic field dataset, one can easily be fooled in believing the amount of data points is sufficient for a good resolution. If a model is constructed in which a single plane in a cylindrical body is composed of 312 different grid cells. The magnetic field due to a current injection is then measured along the whole column at 31 different height level and sampled at each level with 24 three component sensors. This leaves a Jacobian matrix with the dimensions of 2232×312 . Since this can be seen as a system of equations with 2232 equations to solve for 312 unknowns, in other words a highly over-determined system.

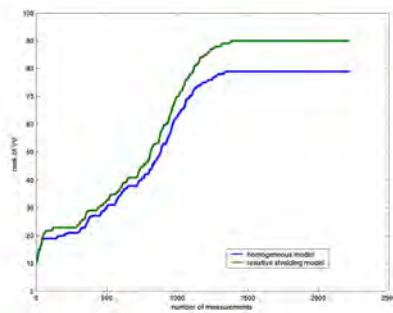


Figure 5.23: Development of the rank of the resolution matrix of the total magnetic field data with increase of data points for a homogeneous and a resistive shielding model

Figure 5.23 shows the development of the rank of the resolution matrix with the increase of data points. As expected the rank of the resolution matrix increases with the number of measurements, but both the homogeneous and the

resistive shielding (see figure 5.17) reach a maximum and stay on that plane. This shows the inability of the data to solve more parameters than a certain level. Other information is needed to achieve a better resolution, again the non-uniqueness of geophysical data inversion plays a large role. Further increase in resolution can only be obtained by introduction of a priori data, other measured parameters or mathematical constrains applied in inversion algorithms (types of inversion schemes or regularisation parameters for instance). In a noise free case (for instance in modelling) the choice of the singular value threshold (as described in equation 5.7) can also lead to increase in resolution, but is limited by the dimensions of the null space (expanding the singular value threshold to the zero valued singular values does not bring additional resolution).

If the effect of the contribution of the three different magnetic field components on the rank of the resolution matrix is studied (see figure 5.24 and table 5.1), one observes the slightly larger rank of the y-component dataset when compared to the x and z components. But the effect is minimal, leading to the conclusion that all magnetic field components practically give the same amount of information on the internal electrical conductivity.

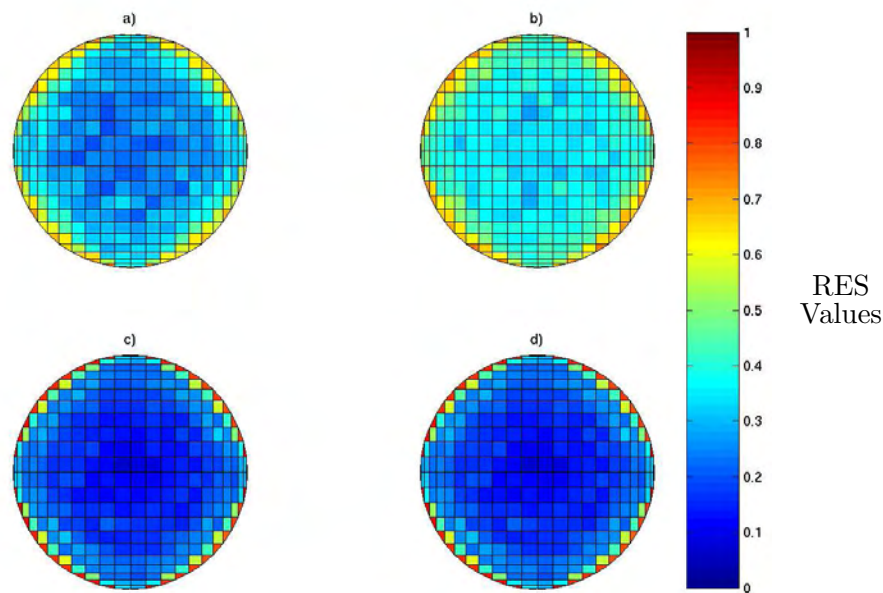


Figure 5.24: Resolution matrices of the three magnetic field components due to a vertical current injection, a) x component, b) y component, c) z component, and d) all three magnetic field components combined.

As was already shown in the resolution calculations, the rank of the resolution matrix is highly dependable on the current injection pattern (see table 5.1). If a horizontal current injection is used in stead of a vertical, the behaviour of the system will be completely different. Also the internal conductivity distribution has a huge impact on the resolving capabilities (see figure 5.23).

	rank B(x)	rank B(y)	rank B(z)
horizontal	76	74	73
vertical	111	112	103

Table 5.1: Rank of the resolution matrices for the three components of the magnetic field with two different current injection patterns

5.4.2 ERT Datasets

Similar conclusions can be drawn from an ERT data set concerning the resolving capabilities (see figure 5.25). Although the overall number measurement points in the Jacobian is less (the Jacobian consists of 1488×312 elements), the actual number of resolvable parameters is higher than in the case of a pure MMR dataset. The behaviour of the rank shows similar features as the previous figures (see figure 5.23), after a certain number of measurements a plateau is reached.

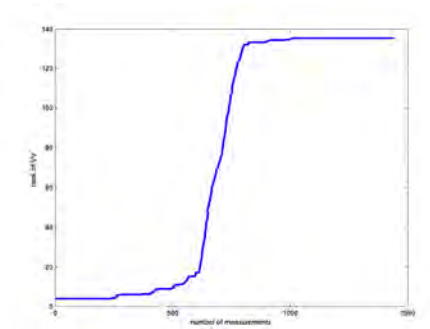


Figure 5.25: Dependency of the resolution matrix rank of a homogeneous column on the number of data points for an ERT dataset

5.4.3 MERIT Datasets

Comparing both the MMR and the ERT data resolution increases with the number of measurements to a MERIT dataset the increase in resolution becomes apparent. From the example models showed in the previous section (the homogeneous column and the shielding scenario) the maximum rank of the resolution matrix was compared (see table 5.4.3). Each model scenario shows the improved resolution of the MERIT dataset very clearly, similar to the spatial distribution of the resolution (figures 5.18, 5.21 and 5.22). These results also provide proof of the considerations made by Edwards and Seigel. In the case of a conductive shielding layer, ERT data quickly loses its resolution, whereas MMR data will provide a relative good resolution.

	RES rank ERT	RES rank MMR	RES rank MERIT
homogeneous column	153	166	192
resistive shielding	181	140	202
conductive shielding	138	181	211

Table 5.2: The rank of the resolution matrix of pure ERT, pure MMR and a MERIT data set for several conductivity scenarios. As current injection a large vertical dipole is used. The total number of model parameters used to calculate RES is 312.

5.4.4 The singular value threshold revisited

In studying the results of the resolution calculation the effect of the singular value threshold becomes apparent. The difference in contribution of the MMR data to the MERIT data in figures 5.18 and 5.21, proved this very clearly. When the resolution is calculated of a Jacobian consisting of two (or more) different data sets, one should pay careful attention to the behaviour of the singular values of each part of the Jacobian.

In order to obtain a justified resolution, the singular values should be in the same dimension range, and even then differences in the rate of decline can cause a difference in the contribution of singular values between the different measurement types. If the singular values of the pure ERT and MMR data sets are plotted together (see 5.4.4), this difference become clear:

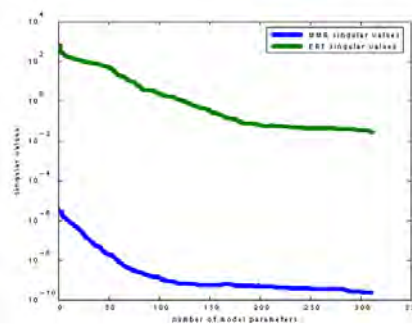


Figure 5.26: Singular value spectra of the Jacobian of an ERT and a MMR data set, calculated for the same model, homogeneous column, $\sigma = 0.1 \frac{S}{m}$.

Clearly in this case, weighting of the data does bring both curves at the same level, but the difference in shape will add a larger contribution of ERT to the MERIT data set than MMR data. A perfect solution for all cases can not be found, since the dimension and shape of the singular values is depends on the

model and the type of measurement. In this thesis both datasets were weighted, such that the maximum eigenvalues were in the same order of magnitude. This can be seen as a minimum invasion in the Jacobian, in order to be able to treat both datasets at the same level of importance. An over-weighting of the MMR data set, will push behaviour of the system of equations in the direction of MMR data, as will an over-weighting of ERT data in the direction of pure ERT.

5.4.5 Concluding Remarks on the Resolution

The implementation of a MMR dataset to an ERT dataset increase the resolving capability greatly. In case of a shielding conductive or resistive layer the effect is so large that features which are not resolved by ERT alone can be resolved by a MERIT dataset. This supports the analytical work done by Edwards, 1974 and Seigel, 1974 and gives the basic justification for the application of MERIT in mapping an electrical conductivity distribution.

The resolution matrix can also be used to determine the maximum of resolvable parameters, and how many elements of the model space cannot be resolved due to the fact that the compromise a highly dependent system of equation instead of an independent one. It can be shown that addition of a MMR data set to an ERT dataset limits the model space with several dimensions (the increase in resolution matrix rank), and therefore reduces the non-uniqueness of the system. This effect is increased if a vertical dipole dataset is used in comparison to a horizontal dipole data set.

Most important aspect however is the wise choice of the singular value threshold. This choice will at first affect how much information is taken into account in calculation of the resolution, on the second hand it will influence the contribution of the MMR data to the MERIT data set. This effect occurs due to the difference in singular values of both data sets, after singular value decomposition and implementation of the threshold only the larger singular values are taken into account, without any prejudice for the source of the values; ERT or MMR.

Chapter 6

Synthetic Data Inversion

This chapter will address the combined inversion of both electrical potential and magnetic field data, in order to obtain an image of the electrical conductivity distribution of the column. The rudimentary inversion scheme described in this chapter is included as a proof of the concept for the MERIT system, and clearly needs further development. Since the forward operator is non-linear and shows singular behaviour, direct inversion of the data is not possible, an iterative inversion scheme needs to be implemented. Statistical inversion algorithms (for instance Simulated Annealing or Monte Carlo schemes) are very CPU-time demanding. Instead a Quasi-Newton algorithm is chosen in which a Broyden Jacobian update is used. The algorithm is tested by implementation of simple synthetic model data.

6.1 The Quasi-Newton Inversion Algorithm

In the inversion of 2D-resistivity surveys the use of a Gauss-Newton or Quasi-Newton (or a combination of both) is widely spread (see e.g. Loke and Barker, 1994, Loke and Dahlin, 1996, and Chambers et al., 2004). In this study the inversion will be limited to the case of 2D electrical conductivity distributions due to the large computing time associated with real 3D Jacobians for a high resolution finite element grid. The 3D forward algorithm developed for MERIT (see Tillmann et al., 2003) will be implemented in the inversion routine. Therefore an in z-direction constant electrical conductivity distribution is assumed in a column with 48 grid cells in both x and y direction (leaving due to the cylindrical shape of the column 312 grid cells with unknown electrical conductivities, all other grid cell represent free space, and have a known electrical conductivity of 0).

Inversion schemes are used to determine a model vector \vec{x} which explains the data vector \vec{y} sufficiently (see equation 5.1), without the need to calculate the inverse of the forward modelling operator \mathbf{A} directly:

$$\vec{x} = \mathbf{A}^{-1}\vec{y} \tag{6.1}$$

In most cases the inverse of matrix \mathbf{A} can not be determined due to the fact that matrix \mathbf{A} is not square, and in the case of real data, also contaminated

with noise. In addition to this comes the non-linear dependency of the modelvector on the datavector in electromagnetic problems. To solve the system of equations, the problem has to be linearized, and a new system of equations has to be constructed, which allows solving an approximation of the real problem.

$$\vec{d} = \mathbf{F}\vec{m} \quad (6.2)$$

where \vec{d} is the linear approximated datavector \vec{y} , \mathbf{F} , the linear forward operator (equivalent to \mathbf{A}) and \vec{m} the linear approximation of the modelvector \vec{x} . The solution of this system of equation will be approximated by a least squares cost functional ($\chi(m)$),

which minimum corresponds to the best model that fits the data vector, while subject to certain constraints:

$$\chi(m) = \chi_d(m) + \lambda\chi_c(m) \quad (6.3)$$

functional χ_d corresponds to the misfit between the calculated data vector and the actual data vector ($\chi_d = \Sigma(\vec{d}_{data} - \vec{d}_{model})^2$ where \vec{d}_{model} is the forward calculated model data) and χ_c an a priori determined constraint function, which is weighted by a regularization parameter λ . Minimization of the cost function can follow several different iterative schemes, each with its own advantages and disadvantages.

In this thesis a Quasi-Newton scheme is chosen to minimize the cost function, in which a smoothness constraint function, the so-called roughness matrix is implemented. The Quasi-Newton method basically is a Gauss-Newton least-squares method without the need to calculate the Jacobian of every new model. The solution of the inverse problem is therefore given by (see e.g. Loke and Dahlin, 1996):

$$\left(\mathbf{J}_i^T \mathbf{J}_i + \lambda_i \mathbf{C}^T \mathbf{C} \right) \overrightarrow{\Delta m}_i = \mathbf{J}_i^T \vec{g}_i \quad (6.4)$$

where \mathbf{J}_i is the Jacobian of the current model, \mathbf{C} the roughness matrix (containing spatial derivatives with respect to both x- and y- direction ($\nabla_{1,2}$ resp.): $\mathbf{C} = \nabla_1 + \nabla_2$) $\overrightarrow{\Delta m}_i$ is the current perturbation vector (the update of the model), λ_i the current Lagrange multiplier or damping factor, \vec{g}_i the data misfit vector (the difference between measured data (\vec{d}_{data}) and current model ($\mathbf{F}(\vec{m}_i)$)). The Lagrange multiplier depends on the maxima of the Jacobian and roughness matrices ($\lambda_i = \frac{\max \mathbf{J}}{\max \mathbf{C}} * f_i$) and is first kept constant, later reduced stepwise during the inversion process by the function $f_i = (1, 1, 0.5, 0.1, 0.001)$.

With the use of the perturbation vector $\overrightarrow{\Delta m}$ an updated model is constructed according to:

$$\vec{m}_{i+1} = \vec{m}_i + \alpha \overrightarrow{\Delta m}_i \quad (6.5)$$

Where α is determined by a line search algorithm in order to find the optimum step size for the perturbation vector $\overrightarrow{\Delta m}_i$. For the step size a third order

polynomial function was fitted to the RMS misfit function of four step sizes ($\mathbf{A}(\overline{m}_i(\alpha(j))) - \overline{d}_{data}$) and the minimum value of the polynomial was obtained.

The Jacobian matrix for the starting model is calculated by application of a difference scheme to the forward routine (see also chapter 5). Subsequent Jacobian matrices are estimated (depicted by \mathbf{J}_i^\dagger) by means of a Broyden scheme (see Broyden, 1965).

$$\begin{aligned} \mathbf{J}_{i+1}^\dagger &= \mathbf{J}_i^\dagger + \overline{u}_i \overline{\Delta x}_i^T \\ \text{where } \overline{u}_i &= \frac{(\overline{\Delta y}_i - \mathbf{J}_i^\dagger \overline{\Delta x}_i)}{\overline{\Delta x}_i^T \overline{\Delta x}_i}, \\ \text{and } \overline{\Delta y}_i &= \overline{y}_{i+1} - \overline{y}_i \end{aligned} \quad (6.6)$$

here \overline{y}_i depicts the response of the i^{th} model and $\overline{\Delta d}_i$ the change in model response between the $(i+1)^{th}$ and i^{th} model (i.e. $\mathbf{F}(\overline{m}_{i+1})$ and $\mathbf{F}(\overline{m}_i)$).

As stopping criterium for the inversion iteration, the difference between two successive model vectors was chosen. If the two successive models did returned similar values and the decrease in RMS misfit was negligible (i.e. $\leq 0.1\%$), the scheme was terminated. The RMS value of the misfit was calculated according to:

$$\text{RMS} = \sqrt{\frac{\sum_{j=1}^k \left(\frac{\overline{d}_{data} - \overline{d}_{model}}{\overline{d}_{data}} \right)^2}{k}} \quad (6.7)$$

6.2 Weighting Electric and Magnetic Data

A major point in the inversion routine is the weighting of the electrical potential and the magnetic field data. The obvious difference in dimensions (potential data in several V and the magnetic field data in nT) already implies the necessity of a weighting factor.

In this scheme a rather simple weighting factor is used, the electrical potential data is normalized by the ratio of the largest value in the magnetic and the maximum of the electrical dataset in order to obtain similar dimensions as the magnetic data. The datavector can therefore be written as:

$$\overline{d} = \left[\begin{array}{c} \overline{d}_B \\ \frac{\max(d_B)}{\max(d_P)} \overline{d}_P \end{array} \right] \quad (6.8)$$

Where \overline{d}_B describes the magnetic dataset, and \overline{d}_P the electrical dataset.

6.3 Synthetic Data Inversion Test Scenarios

In order to test the developed inversion routine two different scenarios were selected, a vertical anomaly and a shielded anomaly. Each synthetic 2D model contains 312 model parameters, constructed in a similar way as presented in chapter 2 . A single vertical current injection was used with an amplitude of 100 mA located at 0 degrees, and with a dipole length of 36.6 cm (equivalent to the large vertical dipole scenario). The dimensions of the modelled column are similar to the soil column used in the experimental setup. At a distance of 5 cm from the column the magnetic field was calculated at 24 different positions (all located in a circle). The electrical potential differences were measured at the 13 available electrodes which are not used for current injection. The electrical potential at the location of the electrodes was interpolated if the location did not coincide with a grid point. All vertical and horizontal dipoles possible in this electrode orientation have been used in the model, leading to 40 possible electrical potential differences. The magnetic field is measured at 44 height levels and includes 3168 data points. To limit the time needed to calculate a single iterative step, only one current injection is used to obtain an image of the conductivity distribution.

6.3.1 Inversion Scenarios

Since the MMR data can only determine conductivity contrasts (see Chapter 1) no homogeneous model will be used to test the inversion algorithm, instead two off axis anomalies will be used in this study to determine the capabilities of the inversion scheme.

An square brick, with an electrical conductivity of 10 S/m, (see figure 6.1) is introduced to an 0.1 S/m homogeneous column , and located off the central axis of the column. The anomaly extends over the complete length of the column, the imaging plane is located in the middle of the column, between both current injection electrodes. After three iterations no decrease in the RMS misfit is obtained, and the final inverse model is returned with and RMS error of 1.9 (see figure 6.2).

Although a complete MERIT data set (ERT and MMR data) is used, the data is unable to obtain the real electrical conductivity values , the ratio between background and model on the other hand is well resolved. The cause of this inability to map the real electrical conductivity values can be found in the difference between the MMR data and the ERT data used in the inversion, the much larger amount of MMR data could force the inversion to get stuck in the local 'MMR minimum', which allows all absolute conductivity values as long as the ratio is correct. Thus the real global minimum with both correct conductivities and ratio is not reached. This behaviour become more clear if both input and modelled dataset are studied (see figure 6.3), the magnetic field data is fitted quite nicely, contrary to the potential field data. Also the huge difference in dimensions between magnetic data and electrical potential becomes clear.

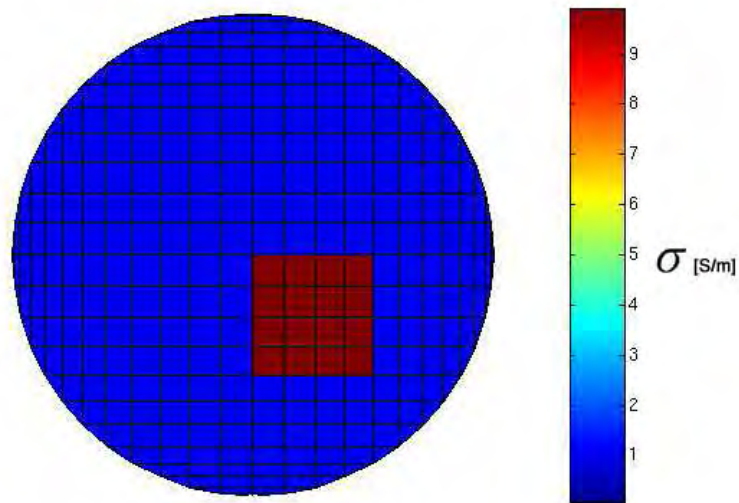


Figure 6.1: Numerical model used in the synthetic inversion

Alternatively a brick-like structure is modelled (see figure 6.4), the electrical conductivities were taken similar to the previous model (0.1 S/m column and 10 S/m anomaly). Inverting this model proved to be a little more difficult (see figure 6.5), hence a slightly larger RMS error of 2.0 % even after more iterations (five iterations were necessary to reach no significant additional decrease in RMS error). The returned model is also not as nicely placed as the column example, and the 'banana-shape' of the anomaly is more pronounced as in the column case, an effect that is caused by the roughness matrix and amplified by the elongated shape of the brick anomaly. Also the fact that only a single current injection is used can give rise to a distorted anomaly.

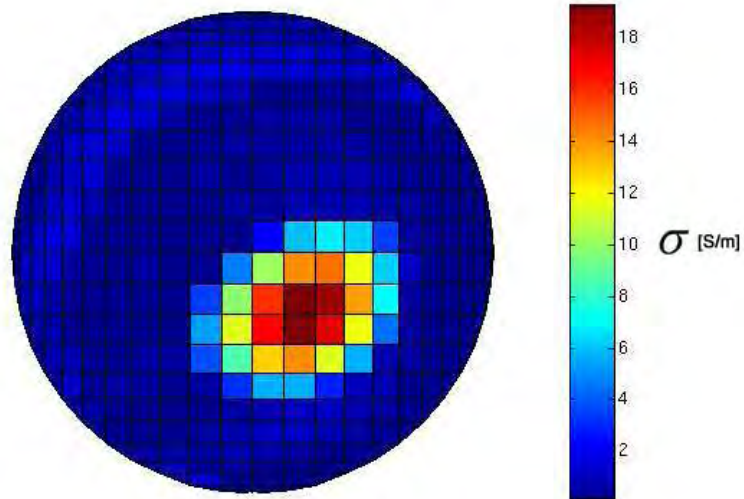


Figure 6.2: Returned model after 3 inversion iterations, RMS error between input data and final data: 1.9%

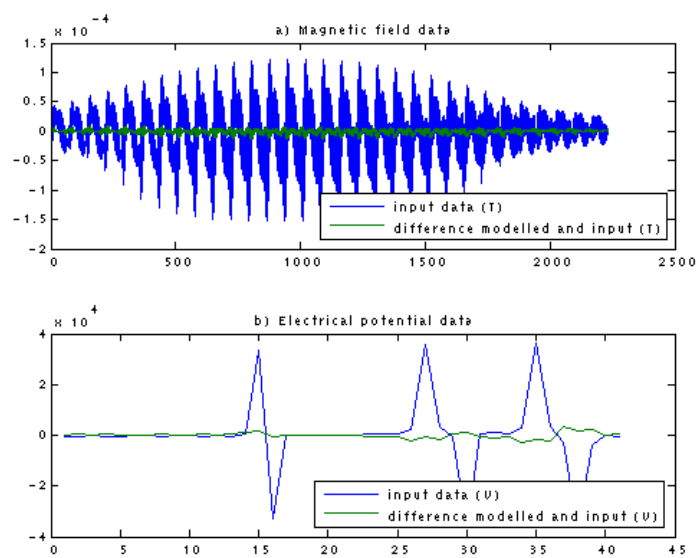


Figure 6.3: Original data compared with the forward calculated data of the returned model of figure 6.2, a) depicts the input magnetic field data and the difference between input and modelled data, b) the potential field data and the difference between input and modelled data.

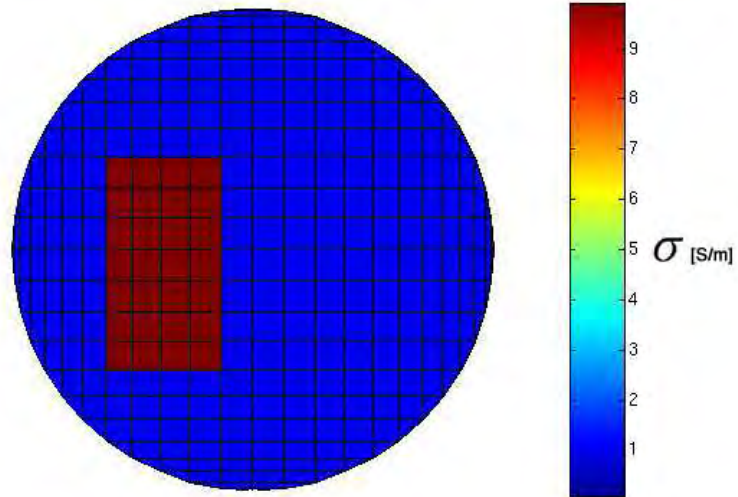


Figure 6.4: Start model for inversion for the brick scenario

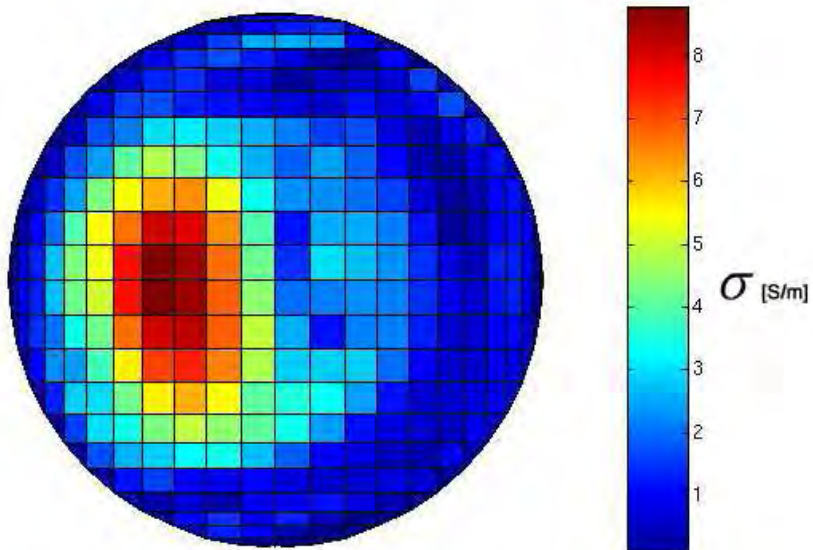


Figure 6.5: Returned model after 5 inversion iterations, RMS error between input and output data 2.0%

Both examples show the relative accurate imaging of the object, both in anomaly shape as in its electrical conductivity contrast. The exact conductivities could not be found possibly due to the large difference in sizes of the MMR and ERT data, which build these MERIT datasets.

6.3.2 Shielded Body Scenario

In order to test the enhanced ability of the MMR data to image shielded bodies also a shielded body scenario was modeled (see figure 6.6). The model consists of 3 different zones, an outer zone with an electrical conductivity of 0.1 S/m, an resistive shell of 0.01 S/m and an inner zone with an electrical conductivity of 10 S/m. In order to be able to present a good distinction between the three electrical conductivity zones, the electrical conductivity is presented as its logarithmic value.

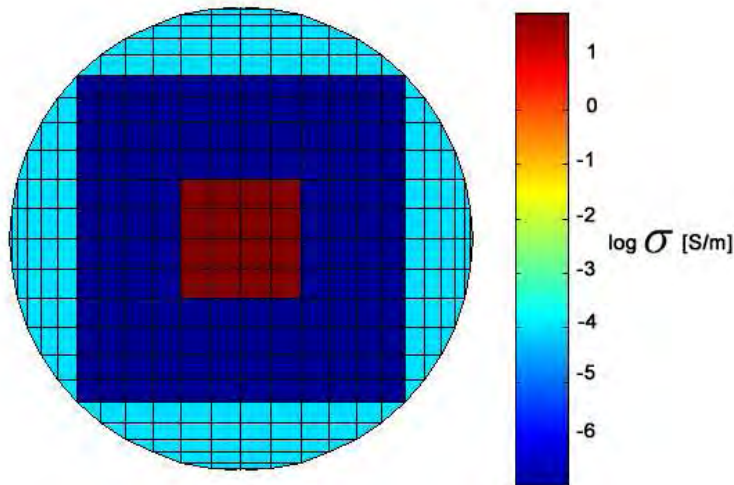


Figure 6.6: Start model for inversion of the shielded model scenario (logarithmic values)

Returning the shielded body anomaly proves to be rather complicated for the inversion routine, there is a some contrast visible between the middle and outer body, but the inner body is imaged rather well. The absolute values are not correct, similar as in the case of the column model (see figure 6.2), but the contrasts are resolved rather well. In comparison to the input model the contrast of core:middle body:outer body is $1:\frac{1}{100}:\frac{1}{10}$, the inversion results shows a contrast of about $1:\frac{1}{1000}:\frac{1}{10}$. Both anomalies appear to be pushed to the right part of the column, the overall size of the inner bodies is still relative good, as is the electrical conductivity contrast. Clearly the single current injection does not contain enough information for a correct reconstruction of the input model.

Therefore the same model was also inverted with two vertical current injections,

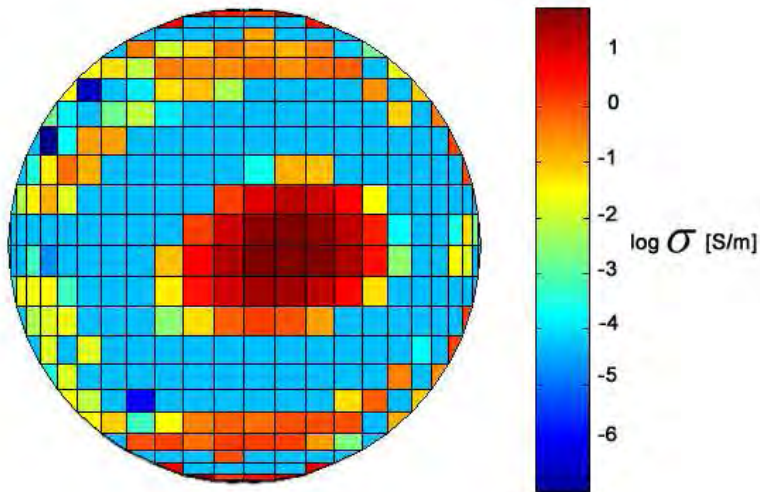


Figure 6.7: Returned model after 5 inversion iterations, RMS error between input and output data 3.8% (logarithmic values)

the first located at the same position as depicted in figure 6.6, the other at the opposite side of the column. The dipole length of both injections was taken constant. The image obtained after 5 iterations 6.8 shows a better result than figure 6.7, with a clearer difference in electrical conductivity contrast between the middle and outer layer. Also the whole anomaly does not experiences the shift to the right.

Although the result shows some improvement in comparison with the single current injection, the reconstruction is still not satisfying. Figure 6.8 points out the limits of this simple inversion scheme, and makes the development of a more sophisticated scheme points out the limits of this simple inversion scheme, and makes the development of a more sophisticated scheme

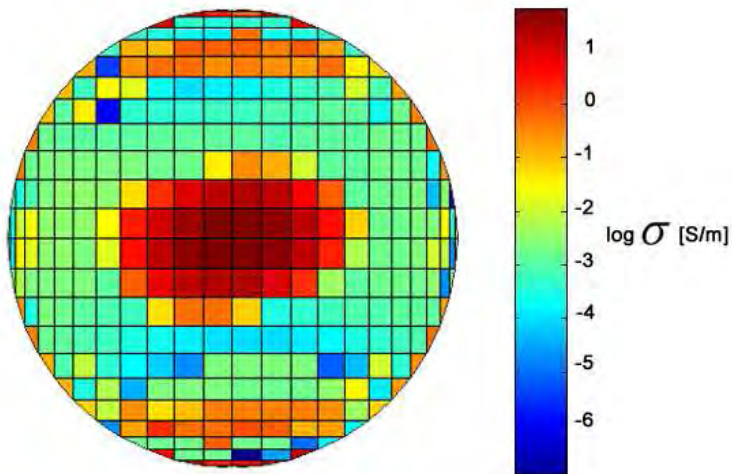


Figure 6.8: Returned model after 5 inversion iterations with 2 opposite vertical current injections, RMS error between input and output data 3.0% (logarithmic values)

6.4 Inversion of Noisy Data

Since a real life dataset always is contaminated by noise, the effect of noise on the reconstruction also is modelled. For this the vertical column dataset is taken (see figure 6.1) and to the forward calculated data 3% of random noise is added. This dataset is then inverted along the same scheme as the original noise free dataset.

The resulting electrical conductivity distribution (see figure 6.9) shows a very similar image as the noise free case (figure 6.2). The anomaly is a little more smooth and the absolute values are more off, although the contrast still is rather good.

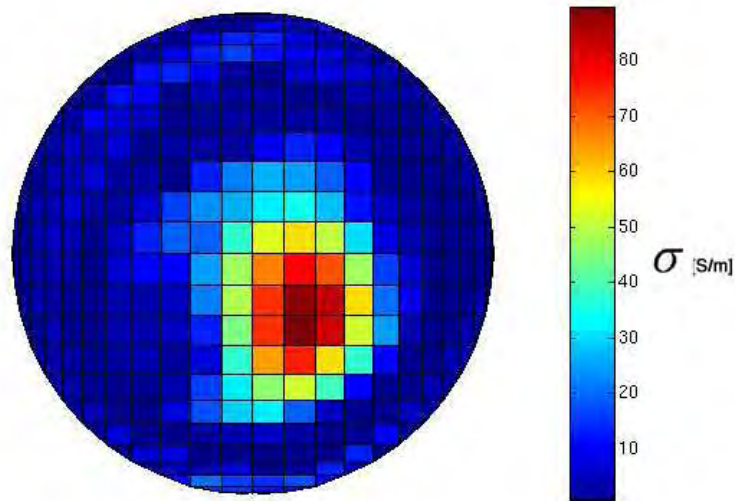


Figure 6.9: Returned model after 3 inversion iterations, with 3% noise added

6.5 Horizontal and Vertical Current Injections Revisited

Finally the conclusions drawn in Chapter 5 were tested on an inversion experiment. Two MERIT datasets of the same conductivity model were calculated (see also Verweerd et al., 2005, one with a horizontal and one with a vertical current injection. Both data sets were treated in the following inversion similar (3 iteration steps, same grid and same lagrange multiplier). A horizontal cut through the column was taken a height in the middle between the height of the horizontal and the lower vertical injection electrodes. This was done in order to prevent a bias of the inversion to the horizontal electrode case. If the plane of inversion is taken at the same height level as the two horizontal, the current distribution pattern can cause a relative high sensitivity in that level, a clear benefit for the horizontal current injection.

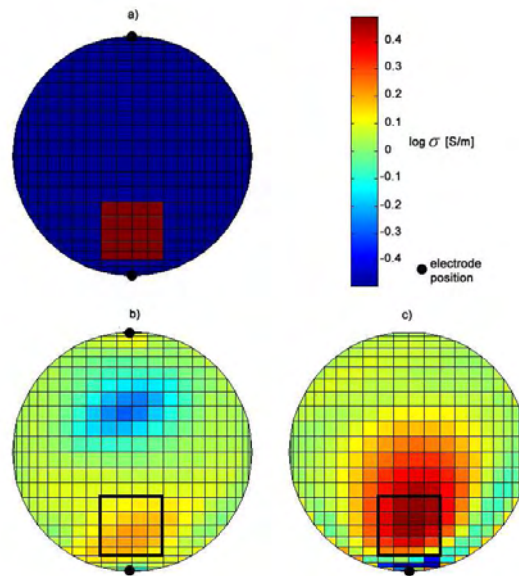


Figure 6.10: Comparison of Horizontal and Vertical current injection on the imaging capabilities. Figure a) depicts the input model, b) a horizontal current injection, c) a vertical current injection pattern.

Both datasets (see figure 6.10) are not able to image the conductivity distribution correctly, although the ratio again is in quite good agreement with the input model. Clearly the vertical current injection provides an image much closer to the original model. Thus giving another indication of the superior information content of a vertical current injection above a horizontal one.

6.6 Concluding Remarks on Inversion

With the development of the 2D quasi-Newton inversion scheme a proof of concept is given for the imaging of the MERIT system. The ability to locate anomalous object is shown clearly, although some models tend to put more emphasis on the MMR part of the system than on the ERT part (in imaging the correct ratio of electrical conductivity between anomaly and column instead of the correct values). The cause could be found in the larger amount of MMR data in respect to the ERT data (in which only 3 rings of 15 electrodes were used (-2 electrodes for current injection)).

Due to the cylindrical nature of the column different sizes in grid cells are necessary to build the finite element grid. These different size in both x and y length in grid sizes give rise to a so-called 'banana-effect' in the returned models, caused by the calculated roughness matrix. The size of the anomaly affects this 'banana-effect' by accentuation of the banana shape for elongated (either in x or y direction) anomalies.

More complicated anomalies (the shielded anomaly for instance) can only partially be reconstructed by the inversion routine when only a single injection current is used. Clearly the need of a more sophisticated inversion scheme, especially tuned to the problems of joining two datasets with a large difference in magnitude is apparent.

In addition the results from Chapter 5, in which a vertical current injection was proven to contain more information than a horizontal one could be supported by a synthetic model. The horizontal injection dataset did provide a far worse image in comparison to the vertical injection dataset of the original conductivity distribution.

Main conclusion is that despite the use of only one current injection a good reconstruction could be obtained by the introduction of the magnetic field data. Proving the value of the addition of MMR data to traditional ERT. Even the introduction of the in geophysics typical 3% noise does not introduce such errors that a relative correct reconstruction is impossible. More complicated models need the addition of more current injections in order to obtain an acceptable result.

Chapter 7

Discussion and Recommendations

In this chapter a discussion around several recommendations will be given, leading to a possible outline for future research on the MERIT system. Also several acquisition targets and other areas of science will be introduced in which MERIT can lead to an increase in information.

With the construction of the scanning torus measurement system a working prototype of the MERIT system is completed. The technique itself is also well developed with the addition of the forward routines. Technical problems remain present, for instance the changes in the amplitude of the injected current due to for instance corrosion effects at the electrodes will decrease the accuracy of the difference measurements. Also the relative high contact resistance due to the small size of the electrodes could give rise to problems in high resistive media, increasing the electrode size will diminish the non-invasive character of the method, especially on the soil column scale.

Also the measurement of magnetic fields is not trivial, sensors will always have the difficulty of measuring a signal in an environment which is highly 'polluted' by other magnetic fields (Earth's magnetic field for instance, which is approximately an order of 5×10^5 larger as the signal due to the injected current). Advances in processing power of the micro controllers used in the sensor modules, for instance can increase the measurement quality and speed considerable. The external field (of natural and anthropogenic origin) also has an effect on the magnetic sensor sensitivity, since the direction of the sensitive axis depends on the external magnetic field. A pre-measurement calibration scheme including a small coil can be used to determine the direction of the sensitive axis by fitting the measured values to the known (calculated) magnetic field of the coil.

Further optimization of the system (for instance in terms of speed) can lead to dynamic imaging of flow and transport processes in soil columns. Numerical experiments showed the ability of MERIT to map the changes in electrical conductivity in these type of experiments (see Tillmann et al., 2004). The flow and transport experiments can be also optimized to incorporate electrical conductivity contrasts due to application of a salt tracer.

One can also introduce the 'sister' technique of MMR: The Magnetic Induced Polarization (see Seigel, 1974), and possibly increase the resolution of standard spectral induced polarization (SIP) in a similar way as MMR supports ERT. The MERIT system prototype can also be used as a basis to develop such a measurement system. Especially when micro-controllers with a higher performance are used which allows the processing of both signal amplitudes and phases. High performance micro controllers can also be used to measure at different lock-in frequencies, thus obtaining even more information.

Up scaling of the MERIT system to so-called lysimeter scale (large soil monoliths) will increase the capability to characterise soil properties in a non-invasive way and can lead to improvements due to the larger volume of investigation in comparison with traditional sensor type used in lysimeter studies (time domain reflectometry, suction cups, tensiometers etc.). Up scaling onto the field scale is also an important aspect (and already proven for mining application by Cattach et al, 1993). A roving magnetometer system used in conjunction with a standard ERT survey could also increase the imaging capability of ERT surveys. The availability of boreholes for current injection will even enlarge the complimentary effect of MMR on ERT.

Combined with the up scaling of the MERIT system, the system could also be implemented in other branches of science. In the field of medicine (see Levy et al., 2002), non-destructive testing (see Nazarov et al, 2004) or industrial tomography (see Kemna et al., 2003 and Zimmermann et al., 2003) the non-invasive aspect of the system is of great importance. With the additional measurement of the magnetic an increase in resolution similar to the increase described in this thesis can be expected. Although one has to keep in mind that the measurement of magnetic fields is limited in application with metallic objects (metal pipes or vessels for instance). These (ferro-)metallic objects interfere in two ways: first due to the presence of eddy currents in the objects which distorts the magnetic field lines. Secondly the magnetic properties (magnetic permeability) will cause magnetic signals on the same scale as signals due to the current injection. Since these effects can not be separated, no clear imaging of the electrical conductivity is possible.

Finally, the inversion routine used is a relative simple scheme, and might not be applicable for monitoring of dynamical processes. More sophisticated techniques, especially tuned to the characteristic problems of magnetic and electrical signals in inversion routines (signal amplitude for instance), can lead to better images. Secondly the quasi-Newton inversion scheme described here is a 2D inversion scheme, and therefore only applicable in a very limited amount of scenarios. A 3D algorithm is therefore highly recommended and currently under development (see Tillmann et al., 2005). Alternative inversion schemes are beginning to emerge for the joint inversion of MMR and ERT data, for instance Gauss-Newton based schemes by Labreque et al., 2003 or Chen et al., 2002.

Chapter 8

Summary and Conclusions

With the development of the MERIT system a new tool to map electrical resistivity distribution is created. The current MERIT system accommodates the measurement of the electrical potential and magnetic field due to a 25 Hz current injection in cylindrical samples. The three components of the magnetic field are measured with AMR sensors and is capable to operate without the use of extensive magnetic shielding in a typical laboratory environment.

The addition of the information on the electrical conductivity contained in the magnetic field leads to an increase in the resolving capability when compared to tradition ERT data. By applying singular value decomposition to the Jacobian of a MERIT dataset the effects of the introduction of the magnetic data could be observed in both data and model space. In data space the contribution of each measurement point to the eigenvalues of the system of equations can be quantified leading to conclusions on the optimum measurement configuration and current injection patterns. It could be proven that vertical current injection dipoles provide superior information in comparison to horizontal dipoles. The increase in resolution can be made visible when the model space is studied. The magnetic data is only sensitive to electrical conductivity contrasts which lead to clear increases in resolution in model scenarios where a shielding layer hides an anomalous object. Less pronounced is the resolution increase due to the addition of MMR data to ERT in homogeneous scenarios. Also the superior resolution of vertical current injections in comparison to horizontal ones could be proven.

A fundamental inversion routine, and thus the final step towards completion of the technique, was presented by the development of a 2D quasi-Newton inversion routine in order to image the electrical conductivity distribution. Which performance is satisfactory for simple models even with a single current injection, but becomes increasingly problematic for more complicated models.

Chapter 9

Acknowledgements

In this section I would like to thank everybody who helped me during my stay in Germany for nearly 3.5 years, both on scientific and personal level. Several people I would like to mention in person since their help was indispensable:

First of all I would like to thank Axel Tillmann and Egon Zimmermann, who both contributed a great deal to my work, and without whom this thesis will not be the same. I really enjoyed working with you the past years, and will miss the cooperation very dearly. You were the proverbial giants, on who's shoulders I could stand.

Secondly I have to thank my parents, Fred and Joke Verweerd, and my sister Japke Verweerd, for helping me where they could and just for being there.

Thirdly I would like to thank my colleagues at the Forschungszentrum Jülich, who putting up with a coffee guzzling, t-shirt and headphones wearing Dutch Geophysicist, I'd like to thank you all for your kindness and great working environment. Special thanks goes out to: Andreas Englert, Walter Glaas, Karsten Gössling, Michael Herbst, John Köstel, Kerstin Müller, Martin Münch and Lutz Weihermüller.

I also would like to thank my friends back 'home', who kept me up to date of everything that happened in Holland, we have wasted a lot of bandwidth with emails: Mark van Doorn, Lisette Beekman, Jacco Kuipers, Frédérique Siegenbeek van Heukelom, Wout Snel, Tamar van Voornveld and Michiel van Zeeland. A very special thanks goes out to Willem Knoops and Yvonne Zwiers who also contributed to my thesis by proofreading.

Finally I have to thank my supervisors, Andreas Kemna, my official Forschungszentrum supervisor, Andreas Hördt, my Doktorvater at the university of Bonn, and Harry Vereecken, my second examiner and director of the Agrosphere Institute. I thank you for all the support, for leaving me enough room to breathe and to find out things my way. In addition I would like to thank Harry Vereecken and Horst Halling, former director of the Zentral Institut für Elektrotechnik, for the opportunity to travel around the world and visit a large amount of conferences and workshops to present my work, you both know I really enjoyed it.

References

1. J. E. Acosta and M. H. Worthington, 1983. A Borehole Magnetometric Resistivity Experiment. *Geophysical Prospecting*, vol. 31, EAGE, Houten, pp. 800-809.
2. G.E. Archie, 1942. The Electrical Resistivity Log as an Aid in Determining Some Reservoir Characteristics. *Transaction of the American Institute of Mining, Metallurgical and Petroleum Engineers*, vol. 146, AIME, Littleton, pp. 54-62.
3. R. Barr, D. Llanwyn Jones and C. J. Rodger, 2000. ELF and VLF Radio Waves. *Journal of Atmospheric and Solar-Terrestrial Terrestrial Physics*, vol. 62, Elsevier Science, Amsterdam, pp.1689-1718..
4. R. Barret, M. Berry, T. F. Chan, J. Demmel, J. Donato, J. Dongarra, V. Eijkhout, R. Pozo, C. Romine and H. van der Vorst, 1994. Templates for the Solution of Linear Systems: Building Blocks for Iterative Methods. *SIAM, Philadelphia*.
5. L. R. Bentley and M.Gharibi, 2004. Two- and Three-dimensional Electrical Resistivity Imaging at a Heterogeneous Remediation Site. *Geophysics*, vol. 69, SEG, Tulsa,, pp. 674-680.
6. S. Berthold, L. R. Bentley and M, Hayashi, 2004. Integrated hydrogeological and geophysical study of depression focused groundwater recharge in the Canadian prairies. *Water Resources Research*, vol.40, AGU, W06505.
7. D. Boggs, 1999. The Theory and Application of Sub-Audio Magnetic Data Acquisition and Numerical Modelling. Phd. Thesis, University of New England, Department for Geology and Geophysics, Armidale.
8. R. Boll and K. J. Overschott (vol. ed.), 1989. Sensors: Magnetic Sensors. *VCH Verlagsgesellschaft, Weinheim*.
9. C.G. Broyden, 1965. A class of methods for solving nonlinear simultaneous equations. *Mathematics of Computation*, vol.19, AMS, Providence, pp.577-593.
10. M. K. Cattach, S. J. Lee, J. M. Stanley and G. W. Boyd, 1993. Sub-Audio Magnetics (SAM) - A High Resolution Technique for Simultaneous Mapping Electrical and Magnetic Properties. *Exploration Geophysics*, vol. 24, ASEG, Perth, pp.387-400.
11. M. K. Cattach, 1996. SUB-AUDIO MAGNETICS (SAM), A High Resolution Technique for Simultaneously Mapping Electrical and Magnetic Properties of the Earth. Phd. Thesis, University of New England, Department for Geology and Geophysics, Armidale.

12. J. E. Chambers, M. H. Loke, R. D. Ogilviy and P. I. Meldrum, 2004. Noninvasive monitoring of DNAPL migration through a saturated porous medium using electrical impedance tomography. *Journal of Contaminant Hydrology*, vol. 68, Elsevier Science, Amsterdam, pp.1-22.
13. J. F. Claerbout, 1976. Fundamentals of Geophysical data processing. *McGraw-Hill, New York*.
14. W. Daily, A. Ramirez, D. Labreque and J. Nitao, 1992. Electrical Resistivity Tomography of Vadose Water Movement. *Water Resources Research*, vol. 28, AGU, Washington DC., pp. 1429-1442.
15. W. Daily and E. Owen, 1991. Cross-borehole Resistivity Tomography. *Geophysics*, vol. 56, SEG, Tulsa, pp.1228-1235.
16. W. Daily, A. Ramirez, and A. Binley, 2004. Remote Monitoring of Leaks in Storage Tanks Using Electrical Resistance Tomography: Application at the Hanford Site. *Journal of Environmental and Engineering Geophysics*, vol. 9, EEGS, pp. 11-24.
17. K. A. Dines and R. J. Lytle, 1979. Computerized Geophysical Tomography. *Proceedings of the IEEE* , vol. 67, IEEE, Los Alamos, pp. 1065-1073.
18. J. Chen, E. Haber, and D. W. Oldenburg, 2002. Three-dimensional Numerical Modelling and Inversion of Magnetometric Resistivity Data. *Geophysical Journal International*, vol. 149, Blackwell Publishing, Oxford, pp.679-697.
19. J. Chen, D. W. Oldenburg, and E. Haber, 2004. Reciprocity in Electromagnetics: Application to Marine Magnetometric Resistivity. *Physics of the Earth and Planetary Interiors*, , submitted, Elsevier Science, Amsterdam.
20. A. Dey and H. F. Morrison, 1979. Resistivity Modeling for Arbitrarily Shaped Three-Dimensional Structures. *Geophysics*, vol. 44, SEG, Tulsa, pp. 753-780 .
21. R. N. Edwards, 1974. The Magnetometric Resistivity Method and its Application to the Mapping of a Fault. *Canadian Journal of Earth Sciences*, vol. 11, NRC Research Press, Ottawa, pp. 1136-1156.
22. R. N. Edwards and E. C. Howel, 1976. Field Test of the Magnetometric Resistivity (MMR) method. *Geophysics*, vol, 41, SEG, Tulsa, pp. 1170-1183.
23. R. N. Edwards, H. Lee, and M. N. Nabighian, 1978. On the Theory of Magnetometric Resistivity (MMR) Methods. *Geophysics*, vol. 43, SEG, Tulsa, pp. 1176-1203.
24. R. N. Edwards, D. C. Nobes, and E. Gómez-Teriño, 1984. Off-shore Electrical Exploration of Sedimentary Basins: The Effects of Anisotropy in Horizontally Isotropic, Layered Media. *Geophysics*, vol. 49, SEG, Tulsa, pp. 566-576.

25. R. N. Edwards, L. K. Law, P. A. Wolfgram, D. C. Nobes, M. N. Bone, D. F. Triggs and J. M. DeLaurier, 1985. First Results of the MOSES Experiment: Sea Sediment Conductivity and Thickness Determination, Bute Inlet, British Columbia, by Magnetometric Off-shore Electrical Sounding. *Geophysics*, vol. 50, SEG, Tulsa, pp. 153-161.
26. J. A. Elders and M. W. Asten, 2004. A Comparison of Receiver Technologies in Borehole MMR and EM Surveys. *Geophysical Prospecting*, vol. 52, EAGE, Houten, pp. 85-96.
27. M. Fathianpour, 1997. Analytical and Numerical Modelling of Total Field Magnetometric Resistivity (TFMMR) Data . Phd. Thesis, Flinders University of South Australia, School of Earth Sciences, Faculty of Science and Engineering, Adelaide.
28. J. B. Fink, E. O. McAlister, B. K. Sternberg and W. G. Wieduwilt (vol. ed.), 1990. Investigations in Geophysics no. 4: Induced Polarization, Application and Case Histories. *SEG, Tulsa*.
29. A. Furman, T. P. A. Ferré, and A. W. Warrick, 2004. Optimization of ERT Surveys for Monitoring Transient Hydrological Events Using Perturbation Sensitivity and Genetic Algorithms. *Vadose Zone Journal*, vol. 4, SSSA, pp. 1230-1239.
30. G. Golub and C. F. van Loan, 1989. Matrix Computations, 2nd Edition. *John Hopkins University Press, Baltimore*.
31. E. Gómez-Trevino and R. N. Edwards, 1979. Magnetometric Resistivity (MMR) Anomalies of Two Dimensional Structures. *Geophysics*, vol. 44, SEG, Tulsa, pp. 947-958.
32. D. J. Griffiths, 1989. Introduction to Electromagnetics, 2nd edition. *Prentice-Hall inc., New Jersey*.
33. A. A. Inayat-Hussain, 1989. Magnetic Field of Direct Currents in Horizontal Stratified Conductors. *Journal of Applied Physics, AIOp*, vol. 65, pp. 3731-3732.
34. J. J. Jakosky, 1933. Method and Apparatus for Determining Underground Structure. *U.S. Patent no. 1906271*.
35. D. Jarman, -. A Brief Introduction to Sigma Delta conversion, Application Notes AN9504. *Milpitas, Ca.*, Available: http://www.intersil.com/support/parametric_data.asp?x=AppNote.
36. J. Jin, 1993. The Finite Element Method in Electromagnetics. *John Wiley Sons inc., New York*.
37. D. Kammer, 1991. Sensor Placement for On-Orbit Modal Identification and Correlation of Large Space Structures. *AIAA Journal of Guidance, Control and Dynamics*, vol 14(2), AIAA, Reston, pp. 251-259.

38. A. Kemna, J. Vanderborght, B. Kulesa, and H. Vereecken, 2002. Imaging and Characterisation of Subsurface Solute Transport Using Electrical Resistivity Tomography (ERT) and Equivalent Transport Models. *Journal of Hydrology*, vol. 267, Elsevier Science, Amsterdam, pp. 125-146.
39. A. Kemna, A. Tillmann, A. Verweerd, E. Zimmermann, and H. Vereecken, 2003. MERIT - A New Magneto-Electrical Resistivity Imaging Technique: 1) Modeling and Tomographic Reconstruction. *Proceedings of the 3rd World Congress on Industrial Process Tomography, Banff*.
40. B. Kulesa, U. Jaekel, A. Kemna, and H. Vereecken, 2002. Magnetometric Resistivity (MMR) Imaging of Subsurface Solute Flow: Inversion Framework and Laboratory Tests. *Journal of Environmental and Engineering Geophysics*, vol. 7, EEGS, Denver, pp. 111-118.
41. D. Labreque, R. Sharpe, D. Casale, G. L. Heath, and J. M. Svoboda, 2003. Combined Electrical and Magnetic Resistivity Tomography: Synthetic Model Study and Inverse Modeling. *Journal of Environmental and Engineering Geophysics*, vol. 8, EEGS, Denver, pp.251-262.
42. D. Labreque, D. Casale, G. L. Heath and J. M. Svoboda, 2002. Combined Electrical and Magnetic Resistivity Tomography: Theory and Inverse Modeling. *Proceedings of the SAGEEP, Las Vegas*, EEGS.
43. C. Lanczos, 1961. Linear Differential Operators. *Von Nostrand, London*.
44. S. Levy, D. Adam, and Y. Bresler, 2002. Electromagnetic Impedance Tomography (EMIT): a New Method for Impedance Imaging. *IEEE Transactions of Medical Imaging*, vol. 21, IEEE, Los Alamos, pp.676-687.
45. S. Liu and T-C. J. Yeh, 2004. An Integrative Approach for Monitoring Water Movement in the Vadose Zone. *Vadose Zone Journal*, vol. 3, SSSA, Madison, pp. 681-692.
46. M. H. Loke and R. D. Barker, 1994. Rapid Least-Squares Inversion of Apparent Resistivity Pseudosections by a Quasi-Newton Method. *Geophysical Prospecting*, vol. 44, EAGE, Houten, pp. 131-152.
47. M. H. Loke and T. Dahlin, 1996. A Comparison of the Gauss-Newton and Quasi-Newton Methods in Resistivity Imaging Inversion. *Journal of Applied Geophysics*, vol. 49, Elsevier Science, Amsterdam, pp. 149-162.
48. R. J. Lytle, A. G. Duba, and J. L. Willows, 1979. Alternative Methods for Determining the Electrical Conductivity of Core Samples. *Review of Scientific Instrumentation*, vol. 50, AIP, Argonne, pp. 611-615.

-
49. J. C. Macnae, Y. Lamontagne, and G. F. West , 1984. Noise Processing Techniques for Time-Domain EM Systems. *Geophysics*, vol. 49, SEG, Tulsa, pp. 934-948.
 50. J. Malmivuo and R. Plonsey, 1995. Bioelectromagnetism. *Oxford University Press, Oxford*.
 51. H. Militzer and F. Weber (vol. ed.), 1985. Angewandte Geophysik Band 2: Geoelektrik-Geothermik-Radiometrie-Aerogeophysik. *Springer Verlag, Wien*.
 52. H.-M. Münch, A. Kemna, K. Titov, E. Zimmermann, and H. Vereecken, 2005. Dependence of the Spectral Induced Polarization Response of Sands on Salinity, Grain Size and Saturation.. *Geophysical Research Abstracts*, 2nd General Assembly of the EGU, Wien, EGU, Lindau..
 53. R. Müller, 1990. Rauschen. *Springer Verlag, Berlin*.
 54. M. N. Nabighian (vol. ed.), 1991. Investigations in Geophysics no. 3: Electromagnetic Methods in Applied Geophysics vol. 1, Theory. *SEG, Tulsa*.
 55. M. N. Nabighian (vol. ed.), 1991. Investigations in Geophysics no. 3: Electromagnetic Methods in Applied Geophysics vol. 2, Application, part A and B. *SEG, Tulsa*.
 56. A. V. Nazarov, F. C. S. da Silva, and D. P. Pappas, 2004. Arrays of magnetoresistive sensors for nondestructive testing. *Journal of Vacuum Science and Technology* , vol. 22, AIP, pp. 1375-1378.
 57. B. Pant and M. Caruso, -. Magnetic Sensors Cross-Axis effect, Application Notes AN-2. *Honeywell, Morristown*, Available:<http://www.ssec.honeywell.com/magnetic/datasheets.html>.
 58. J. L. Poston, 1998. A Parallel Algorithm for Subset Selection. *Journal of Statistical Computation and Simulation*, vol. 60, GSCS, Blacksburg, pp. 1-17.
 59. J. M. Reynolds, 1997. An Introduction to Applied and Environmental Geophysics. *J. Wiley & Sons, New York*.
 60. P. Ripka (vol. ed.), 2001. Magnetic Sensors and Magnetometers. *Artech House, Boston*.
 61. H. O. Seigel, 1974. The Magnetometric Induced Polarization Method. *Geophysics*, vol. 30, SEG, Tulsa, pp. 321-339.
 62. M. K. Sen and P. L. Stoffa, 1995. Global Optimization Methods in Geophysical Inversion. *Elsevier Science, Amsterdam*.
 63. R. Snieder and J. Trampert, -. Inverse Problems in Geophysics. *Samizdat Press*, Available: <http://samizdat.mines.edu/>.

-
64. E. C. Stoner and E. P. Wohlfahrt, 1991. A Mechanism of Magnetic Hysteresis in Heterogeneous Alloys (reprint from 1947). *IEEE Transaction of Magnetism*, vol. 27, IEEE, Los Alamos, pp. 3475-3518.
 65. J. M. Svoboda, B. Canan, J. L. Morrison, G. L. Heath, and D. Labrecque, 2002. Advanced Technology for Mapping Subsurface Water Conductivity. *Proceedings of SAGEEP 2002, Las Vegas*, EEGS.
 66. W. M. Telfors, L. P. Geldart, and R. E. Sheriff, 1990. Applied Geophysics, 2nd edition. *Cambridge University Press, Cambridge*.
 67. W. Thomson, 1857. On the Electro-Dynamic Qualities of Metals-Effect of Magnetization on the Electrical Conductivity of Nickel and Iron. *Proceedings of the Royal Society, London*, vol. A8.
 68. A. Tillmann, A. Verweerd, A. Kemna, E. Zimmermann, and H. Vereecken, 2003. Non-invasive 3D Conductivity Measurements with MERIT. *Proceedings of the SAGEEP, San Antonio*, EEGS.
 69. A. Tillmann, R. Kasteel, A. Verweerd, E. Zimmermann, A. Kemna, and H. Vereecken, 2004. Non-invasive 3D Conductivity Measurements During Flow Experiments in Columns with MERIT. *Proceedings of the SAGEEP, Colorado Springs*, EEGS.
 70. A. Tillmann, R. Kasteel, A. Verweerd, E. Zimmermann, A. Kemna, and H. Vereecken, 2004. Flow Experiment Monitoring with Non-invasive 3D Conductivity Measurements. *Geophysical Research Abstracts*, 1st General Assembly EGU, Nice, EGU.
 71. A. Tillmann, R. Kasteel, A. Verweerd, E. Zimmermann, A. Kemna, and H. Vereecken, 2004. MERIT: Eine nichtinvasive Methode zur Beobachtung von Fließ- und Transportprozessen in Bodenproben. *Proceedings of the 64th General Assembly of the DGG, Berlin*, DGG.
 72. A. Tillmann, R. Kasteel, A. Verweerd, E. Zimmermann, A. Kemna, and H. Vereecken, 2004. Non-invasive 3D Conductivity Measurements During Flow Experiments in Columns with MERIT. *Proceedings of the Eurosoil, Freiburg*.
 73. A. Tillmann, A. Verweerd, E. Zimmermann, W. Glaas, A. Kemna, and H. Vereecken, 2005. Non-invasive monitoring of flow and transport processes with MERIT. *Geophysical Research Abstracts*, 2nd General Assembly of the EGU, Vienna, EGU, Lindau.
 74. S. Tumanski, 2001. Thin Film Magnetoresistive Sensors. *IoP Publishing, Bristol*.
 75. H. Vereecken, S. Hubbard, A. Binley, and T. Ferré, 2004. Hydrogeophysics: An Introduction from the Guest Editors. *Vadoze Zone Journal*, vol.3, SSSA, pp. 1060-1062.

-
76. H. Vereecken, A. Kemna, A. Tillmann, H. Vanderborght, and A. Verweerd, 2004. Hydrogeophysical Characterization of Subsurface Solute Transport at the Krauthausen Test Site: Experiments and Numerical Modeling. *Proceedings of the International COST 629 Workshop, Rome*, .
 77. A. Verweerd, E. Zimmermann, A. Tillmann, A. Kemna, and H. Vereecken, 2003. MERIT- Mapping Electrical Conductivity Distributions on a Lab Scale. *Proceedings of the Interurban Workshop on Water and Organic Matter in Soils, Berlin*.
 78. A. Verweerd, A. Tillmann, E. Zimmermann, A. Kemna, and H. Vereecken, 2004. MERIT: Sensor Module Design and Data Acquisition. *Proceedings of the 64th General Assembly of the DGG, Berlin, DGG*.
 79. A. Verweerd, E. Zimmermann, A. Tillmann, A. Kemna, and H. Vereecken, 2004. A New Scanning System for Resistivity Imaging of Porous Media. *Geophysical Research Abstracts*, 1st General Assembly of the EGU, Nice, EGU, Lindau.
 80. A. Verweerd, E. Zimmermann, A. Tillmann, A. Kemna, and H. Vereecken, 2004. Development of a New Magneto-Electrical Resistivity Imaging System. *Proceedings of the 66th EAGE Conference and Exhibiton, Paris*, EAGE, Houten.
 81. A. Verweerd, A. Tillmann, E. Zimmermann, A. Kemna, and H. Vereecken, 2004. Magneto-Electric Mapping of 3D Electrical Conductivity Distributions: System Design and Resolution Analysis. *Proceedings of the 10th European Meeting of the EEGS, Utrecht*, EAGE, Houten.
 82. A. Verweerd, A. Tillmann, E. Zimmermann, A. Kemna, and H. Vereecken, 2005. Optimum current injection pattern for a new magneto-electrical measurement system . *blabla*, submitted.
 83. P. Weidelt and A. Weller, 1997. Computation of Geoelectrical Configuration Factors for Cylindrical Core Samples. *Scientific Drilling*, vol. 6, Springer, Berlin, pp. 27-34.
 84. R. A. Wiggins, 1972. The General Linear Inverse Problem: Implication of Surface Waves and Free Oscillations for Earth Structure. *Reviews of Geophysics and Space Physics*, vol. 10, AGU, Washington, pp. 251-285.
 85. Y. Rubin and S. Hubbard (vol. ed.), 2005. Water Science and Technology Library, vol. 50: Hydrogeophysics. *Springer, Berlin*.
 86. E. Zimmermann, A. Verweerd, W. Glaas, A. Tillmann, and A. Kemna, 2003. MERIT - A New Magneto-Electrical Resistivity Imaging Technique: 2) Magnetic Sensors and Instrumentation. *Proceedings of the 3rd World Congress on Industrial Process Tomography, Banff*.

87. E. Zimmermann, A. Verweerd, W. Glaas, A. Tillmann, and A. Kemna, 2005. A new AMR sensor based magneto-electrical resistivity imaging system. *IEEE Sensors*, vol.5, IEEE, Los Alamos, pp.232-241.
88. E. Zimmermann, G. Brandenburg, W. Glaas and A. Kemna, 2001. Untersuchung hochempfindlicher magnetoresistiver Sensoren für geophysikalische Anwendungen. *Internal Report (KFA-ZEL-IB-500101)*, Forschungszentrum Jülich GmbH.

personal information

name: Arre Job Verweerd

date of birth: 16.06.1976

place of birth: Lekkerkerk, the Netherlands

education

- 2002-2006: Doktorarbeit at the Rheinischen Friedrich-Wilhelms-Universität in Bonn, Germany Department of Geodynamics and Geophysics.
- 2001 Doctoraal degree in Geophysics, Utrecht Univeristy Utrecht, the Netherlands, department of Applied Geophysics.
- 1996 Propedeuse degree in Geophysics, Utrecht Univeristy, Utrecht, the Netherlands, department of Applied Geophysics.
- 1995-2001 Student Geophysics, Utrecht Univeristy, Utrecht, the Netherlands, department of Applied Geophysics.
- 1995 VWO examn at the Christelijk Lyceum in Alphen aan den Rijn, the Netherlands (mathematics, physics, chemistry, biology, geography, Dutch, English).
- 1993-1995 VWO student at the Christelijk Lyceum in Alphen aan den Rijn, the Netherlands.
- 1993 HAVO examn at the Christelijk Lyceum in Alphen aan den Rijn, the Netherlands (mathematics, physics, chemistry, biology, Dutch, English).
- 1989-1993 HAVO student at the Christelijk Lyceum in Alphen aan den Rijn, the Netherlands.

Di manakah engkau, ketika Aku melerakkan dasar bumi?

Ceritakanlah, kalau engkau mempunyai pengertian!

Siapakah yang telah menetapkan ukurannya?

Bukankah engkau mengetahuinya?

- Atau siapakah yang telah merentangkan tali pengukur padanya?

Atas apakah seni-sendinya dilantak, dan siapakah yang memasang batu
penjurunya?

Ayup 38: 4-6